

Numerical analysis of bubble interactions in sonochemistry

Author: Dániel Nagy

Supervisor:

Dr. Ferenc Hegedűs (BME–HDS)

Péter Kalmár (HDS–BME)

October 30, 2023

Scientific Student Conference at BME



M Ű E G Y E T E M 1 7 8 2



Hidrodinamikai
Rendszerek
Tanszék



Új Nemzeti
Kiválóság Program

Contents

1	Introduction	6
1.1	Sonochemical reactors	6
1.2	Modeling of single-bubbles	7
1.3	Multi-bubble systems	9
1.4	ALPACA compressible multiphase flow solver	10
1.5	Goal	12
2	Validation	13
2.1	Spherical validation	13
2.1.1	Simulation setup	13
2.1.2	Quantifying the non-sphericity	15
2.1.3	Results	17
2.2	Non-spherical Validation	21
2.3	Cross validation with ROM	21
2.3.1	Initial shape in ALPACA	21
2.3.2	Simulation settings	22
2.3.3	Results	22
3	Multi-bubble systems	27
3.1	Setup	27
3.2	Convergence	29
3.3	Effect of distance	33
3.4	Interaction phenomena	37
3.4.1	Coalescence in the expansion phase	37
3.4.2	Non-spherical expansion	37
3.4.3	Symmetric jets	38
3.4.4	Delayed jets	39
3.4.5	Halting jets	40
3.4.6	Effects through the pressure field	41
3.4.7	Pressure wave emission	42
3.5	Influence of parameters	43
3.6	Adding more bubbles	46
4	Conclusion	48
4.1	Validation	48
4.2	Reduced Order Model (ROM)	48
4.3	Multi-bubble systems	49
4.4	Improvement points	50
5	Appendix	54
5.1	Legendre polynomials and surface modes	54
5.2	Derivation of standing and traveling waves	55
5.3	Simulation settings	57

Absztrakt

A szonokémia lényege kémiai folyamatok hatékonyságának a növelése ultrahangos besugárral. Egy buborék az ultrahangos besugárzás hatására oszcillálni kezd, azaz periodikusan kitágul és összeomlik. Bizonyos paraméterek mellett az összeomlás olyan nagy lehet, hogy a buborék átmérője és ezáltal a térfogata lényegesen lecsökken, így a buborékban lévő gáz nyomása és hőmérséklete jelentősen megnő. Ez az akusztikus kavitáció, amely kémiai folyamatokat indíthat be a buborékban. A szonokémiában a buborékok sugara néhány mikrométer és a besugárzás frekvenciája az ultrahang tartományba esik ($>20\text{kHz}$). Egyetlen gömb alakú buborék viselkedése leírható a Keller-Miksis egyenlettel és ez alapján az optimális paraméterek megtalálhatók a lehető legnagyobb kompresszió és határfok eléréséhez. Azonban egy szonokémia reaktorban több millió buborék is lehet, és a buborék-buborék illetve a buborék-akusztikus térinterakciók jelentősen csökkenthetik a kompresszió határfokát.

Egy szonokémia reaktorban számos különféle buborék-buborék interakció előfordulhat. A legegyszerűbb eset az összeolvadás és szétesés. Két egymáshoz közel elhelyezkedő buborék a kitágulás során összeolvadhat, illetve egy buborék széteshet több darabra egy összeomlás során. Előfordulhatnak komplexebb jelenségek, például egy tengelyszimmetrikus buborékösszeomlás során a buborékba a tengely mentén folyadéksugár áramolhat ami a buborékot szétszakítja, ez a folyadéksugár képes környező buborékokat is befolyásolni, például azok is széteshetnek. A buborék hatással lehet az akusztikus térre a buborékösszeomlás és szétesés során, amikor az nagy amplitúdójú nyomáshullámot bocsát ki, illetve a buborékok az akusztikus hullámot kitakarják és csillapítják.

A buborék és akusztikus tér interakciók szimulálása komplex feladat, hiszen ehhez egyrészt szükséges egy kétfázisú szimuláció a fázishatár pontos leírásával, ráadásul a fázishatár időben gyorsan változhat. Másrészt az akusztikus teret is szimulálni kell, amely a folyadék összenyomható modellezését igényli. Harmadrészt a használt ultrahang hullámhossza (néhány milliméter) és a buborék mérete (néhány mikrométer) között jelentős méretbeli különbség van, így az akusztikus tér és a buborékok együttes szimulációja nagyon nagy méretbeli különbséget igényel a numerikus hálóban. A dolgozatban a már korábban többször használt ALPACA szoftver kerül alkalmazásra. Az ALPACA képes többfázisú, összenyomható áramlások numerikus szimulációjára, így lehetséges mind a buborékok szimulációja, és az akusztikus tér figyelembe vétele is. Az ALPACA korszerű multiresolution algoritmust használ, amely a megfelelő paraméterek mellett képes a hálót automatikusan beállítani úgy, hogy a buborék határfelülete akár 1000-szer kisebb cellákkal kerüljön felbontásra, mint a tartomány buboréktól távolabbi részei.

A dolgozatban bemutatásra kerül az ALPACA megoldó és annak validálása szonokémiai szimulációk szempontjából releváns paramétertartományban. Ezután két buborékot tartalmazó tengelyszimmetrikus szimulációk beállításának a bemutatása következik és a különböző buborék interakciók is bemutatásra kerülnek. A cél a buborékok közti távolság hatásának a vizsgálatát a dinamikára.

Abstract

Sonochemistry is a field that aims to enhance the efficiency of chemical processes through the use of ultrasonic irradiation. When a bubble is exposed to ultrasonic waves in a liquid, it undergoes oscillations, periodically expanding and collapsing. Under specific conditions, these collapses can become substantial, resulting in a significant reduction in the bubble's diameter and, consequently, an increase in the pressure and temperature of the gas within the bubble. This phenomenon is known as acoustic cavitation, and it can trigger chemical reactions within the bubble. In sonochemistry applications, the bubbles typically have a radius of a few micrometers, and the irradiation frequency falls within the ultrasonic range (>20 kHz). The behavior of a single spherical bubble can be mathematically described by the Keller-Miksis equation. Using this equation, one can determine the optimal parameters to achieve the highest compression and efficiency. However, it's important to note that sonochemical reactors may contain millions of bubbles, and interactions between these bubbles or between the bubbles and the acoustic field can lead to a significant reduction in compression efficiency.

In a sonochemical reactor, various bubble-bubble interactions can occur. The simplest cases involve merging and breaking up. When two bubbles are in close proximity, they may coalesce during their expansion phases. Alternatively, a single bubble may break up into multiple smaller bubbles during a collapse. More complex phenomena can also be observed. For instance, during an axisymmetric bubble collapse, a jet of liquid may penetrate the bubble along its axis, causing it to break apart. This process can also influence nearby bubbles, potentially causing them to break up as well. Furthermore, bubbles can influence the acoustic field during both their collapse and break-up phases. They may emit high-amplitude pressure waves or dampen the acoustic wave in the surrounding environment.

The simulation of bubble-acoustic field interactions is a complex task, since it requires a two-phase simulation with an accurate description of the phase boundary, and the phase boundary can change rapidly over time. Additionally, simulating the acoustic field requires a compressible fluid model. Complicating matters, there's a significant size difference between the ultrasound wavelength used (a few millimeters) and the bubble size (a few micrometers). Consequently, simulating the acoustic field and the bubbles together necessitates a considerable disparity in the cell size of the numerical mesh. In this paper, the ALPACA software is applied, which has been previously employed for similar cases. ALPACA is capable of numerically simulating multiphase compressible flows, allowing us to simulate both bubbles and the acoustic field. An advanced multiresolution algorithm in ALPACA automatically adjusts the mesh, ensuring that the bubble boundary is resolved with cells up to 1000 times smaller than those used in regions farther from the bubble.

This paper introduces the ALPACA solver and its validation within a parameter range relevant to sonochemical simulations. The subsequent section outlines the configuration of axisymmetric simulations involving two bubbles and discusses various bubble interactions. The primary objective is to explore the impact of the distance between bubbles on their dynamics.

Notations

Notations used in the paper

Notation	Explanation
a_0	cell size on l_0 level
a_{\min}	minimum cell size
\hat{a}_{avg}	non-sphericity based on square sum of modes
\hat{a}_{dev}	non-sphericity based on deviation from a sphere
\hat{a}_{max}	non-sphericity based on max. mode amplitude
c	speed of sound
c_V	specific heat capacity
d	distance between bubble interfaces
e	internal energy
f	acoustic frequency
l_m	m th level of the multiresolution mesh
m_b	mass of the bubble
\hat{m}_b	dimensionless mass of the bubble
p	pressure
p_0	ambient pressure
p_A	pressure amplitude
p_b	average pressure in the bubble
p_∞	background pressure (Stiffened Gas EoS)
t	time
x	radial coordinate (axissymmetric model)
y	axial coordinate (axissymmetric model)
y_0	center of bubble
u	velocity in x -dimension
v	velocity in y -dimension
D	distance between bubble centers
D^*	dimensionless bubble distance
D_{cell}	number of cells along the bubble diameter
R	bubble radius (also equivalent radius)
\tilde{R}	equivalent bubble radius
R_0	initial bubble radius (also equilibrium radius)
R_E	equilibrium bubble radius
R_{spec}	specific gas constant
T	temperature
T_b	average temperature of the bubble
V_b	volume of the bubble
γ	ratio of specific heats
γ	parameter of the Stiffened Gas EoS
λ	wavelength
ϕ	<i>level-set</i> function
ρ	density
ρ_b	average density of the bubble

1 Introduction

Sonochemistry studies the effects of ultrasound waves on chemical reactions and processes. Its significance lies in its potential industrial applications, which encompass the synthesis of molecules, ultrasonic cleaning, and improved mixing due to irradiation. It holds promise in various fields of engineering and science. In chemical engineering, it offers an environmentally friendly approach to molecule production. Green chemistry, with its focus on reducing the emission and use of hazardous materials in processes, has gained increasing importance [1]. Sonochemistry can streamline highly complex, multistep chemical reactions, often requiring fewer steps and enhancing efficiency [2, 3]. It also finds niche applications, such as the controlled production of nanoparticles [4, 5]. In the food and pharmaceutical industries, sonochemistry proves valuable for surface cleaning without the need for hazardous chemicals [6]. Furthermore, ultrasound can be employed for water treatment [7].

The physical foundation of this method is a specific form of cavitation known as acoustic cavitation. Due to the high-pressure amplitudes of the sound field, which can reach hundreds of kilopascals, micrometer-sized bubbles form in the liquid. These bubbles experience rapid expansion when the pressure in the surrounding liquid is low and contraction when the pressure is high [8]. These expansion-contraction cycles occur quickly due to the ultrasonic frequency of irradiation, typically exceeding 20 kHz. If the pressure amplitude is sufficiently high, the contraction phase can be exceptionally intense in a short period, resulting in pressures inside the bubble reaching several megapascals, and temperatures soaring to thousands of Kelvins. This phenomenon is referred to as acoustic cavitation. Unlike most engineering applications, in sonochemistry, cavitation is a deliberate and essential phenomenon. Bubbles and cavitation serve as the fundamental elements of every sonochemical application, creating the extreme conditions under which chemical reactions can take place. For instance in ultrasonic cleaning, the collapse of bubbles near a surface generates high-velocity jets that can kill bacteria or remove contaminants from surfaces.

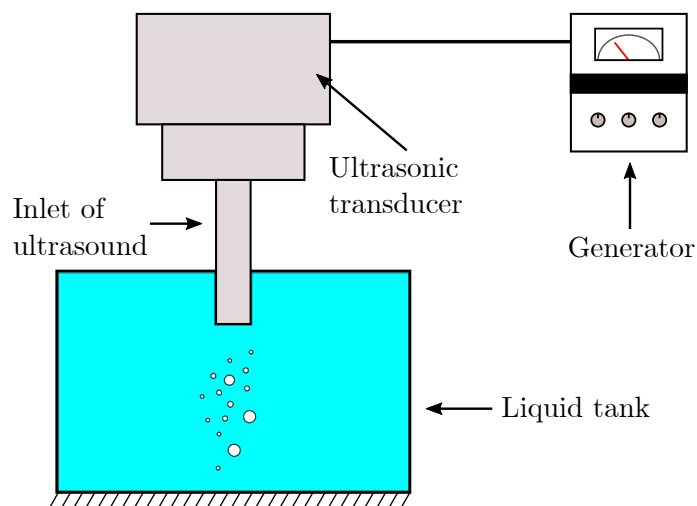


Figure 1.1: Parts of a sonochemical reactor

1.1 Sonochemical reactors

Sonochemical reactors are relatively straightforward to construct. They typically involve the insertion of an ultrasonic transducer into a liquid tank, as illustrated in Figure 1.1. This transducer is connected to an electrical function generator. Typically, a sinusoidal excitation is used

with a specified frequency f and amplitude p_A , which can be adjusted on the generator. These are the most crucial control parameters because they are the easiest to modify. In Figure 1.1, the ultrasound source is located to the north, and the sound wave propagates towards the south wall, where it is reflected. The combination of the wave traveling south and the reflected wave traveling north can create a standing wave if the distance between the wall and the inlet (l) corresponds to a multiple of half the wavelength (λ), which is expressed as

$$l = n \cdot \frac{\lambda}{2}, \text{ where } n \in \mathbb{N}^+. \quad (1.1)$$

Depending on the application, a multi-frequency excitation can be applied, which may help enhance cavitation [9]. The type of liquid is application-dependent, furthermore particles or gases are usually also dissolved in the liquid. Water can be used to create hydrogen or ammonium; however, the production of carbon nanotubes requires chlorobenzene with ZnCl_2 particles [10].

Microbubbles are typically generated when the high-pressure ultrasound is activated, leading to the coalescence of pre-existing nanobubbles, which are bubbles with a sub-micrometer radius. In some instances, gas is introduced directly into the liquid tank to create new bubble nuclei and accelerate the bubble formation process. Large bubbles can readily fragment into numerous smaller ones, constituting another significant means of bubble generation. These methods commonly yield a cloud of bubbles containing hundreds of thousands or even millions of individual bubbles. Alternatively, bubbles can be generated one at a time using short laser pulses. In this scenario, a substantial amount of energy is deposited in the liquid, causing localized evaporation [11]. This technique is often employed in experimental setups to investigate the behavior of individual bubbles because it allows for the nearly precise replication of the same bubble multiple times.

The ultimate objective is to establish a modeling framework capable of simulating an entire sonochemical reactor, thereby enabling the determination of the chemical output based on the input parameters, which can be then used for parameter optimization. This comprehensive simulation necessitates the modeling of various components, including the bubbles, the acoustic field and the chemical reactions. Furthermore, as a reactor can house millions of bubbles, interactions between these bubbles and their impact on acoustic damping become significant. These interactions and acoustic damping have the potential to diminish the reactor's efficiency. Consequently, for a precise reactor simulation, it is important to account for these effects.

1.2 Modeling of single-bubbles

Modeling single bubbles in an acoustic field is relatively straightforward when assuming a spherical shape. The Gilmore equation provides a suitable framework by considering the compressibility of the liquid, surface tension, and the primary effects of viscosity. However, it operates under the assumption of a small density variation in the liquid [12]. In sonochemistry, the Keller-Miksis equation is the widely used model. This equation incorporates the effects of surface tension, full viscosity, and acoustic radiation [13]. The Keller-Miksis equation is a second-order differential equation for the bubble radius R , which is expressed as:

$$\left(1 - \frac{\dot{R}}{c}\right) R\ddot{R} + \left(1 - \frac{\dot{R}}{3c}\right) \frac{3}{2}\dot{R}^2 = \left(1 + \frac{\dot{R}}{c} + \frac{R}{c} \frac{d}{dt}\right) \frac{(p - p_\infty(t))}{\rho}, \quad (1.2)$$

where c is the sound speed in the liquid, p is the far-field pressure and ρ is the density of the liquid. The acoustic excitation is included through the p_∞ pressure term, in a sinusoidal standing wave

$$p_\infty = p_A \sin(\omega t), \text{ where } \omega = 2\pi f. \quad (1.3)$$

In the event of a substantial bubble collapse initiating from a large bubble, the spherical shape is no longer maintained as the surface tension force is not strong enough to keep the bubble spherical. The modeling of non-spherical bubbles is a more complex task, although several simplifications can be made. When a bubble experiences excitation along a single axis, the resulting shape oscillation is axisymmetric. This axisymmetric bubble surface at a specific time t can be described using polar coordinates r and θ [14], as illustrated in Figure 1.2d. As long as the bubble shape is axisymmetric the bubble surface S is assumed in a general Fourier-series form as [15],

$$S(r, \theta, t) = r - R(t) - \sum_{n=1}^{\infty} a_n(t) P_n(\cos(\theta)) = 0, \quad (1.4)$$

where a_n is the n th mode amplitude, P_n is the n th Legendre polynomial, and $P_n(\cos(\theta))$ functions are the orthogonal basis of the general Fourier series. The first few mode shapes are illustrated in Figure 1.2, the 0th mode corresponds to the radial dynamics $R(t)$, the 1st mode is the translational motion of the bubble and higher modes describe the deviation from the spherical shape.

The Keller-Miksis equation can be expanded to incorporate the oscillations of these axisymmetric surface modes, enabling the description of non-spherical bubble oscillations. However, this approach assumes small surface oscillations, typically requiring the amplitudes of the modes to be significantly less than the bubble radius, i.e., $a_n \ll R$. This approach is commonly referred to as the Reduced Order Model (ROM), which consists of a set of coupled differential equations governing the bubble radius R and the surface modes a_i . The ROM is grounded in perturbation theory and assumes potential, inviscid, and incompressible flows. For this application additional terms are incorporated, to allow the description of weakly-viscous and weakly-compressible cases [16].

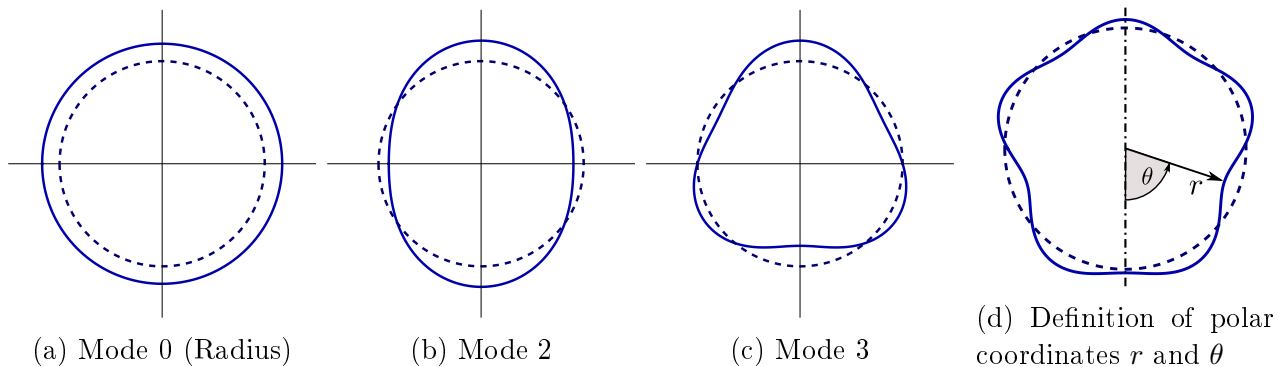


Figure 1.2: Illustration of the first few axisymmetric modes (with y -axis of symmetry) and the description of a perturbed bubble surface using polar coordinates r and θ .

When the amplitude of surface oscillations becomes substantial, the reduced-order model is no longer suitable. Large surface oscillations can potentially lead to bubble breakup, and such scenarios can only be effectively examined through measurements or multiphase hydrodynamic simulations. Multiphase hydrodynamic simulations of microbubbles can be performed using computational tools such as OpenFOAM [17, 18], ALPACA [19], and self-developed research software [20]. In numerical simulations, the bubble interface can be represented using the Volume of Fluid (VoF) technique. In VoF, a transport equation is formulated to determine the volumetric fraction of a particular phase within a cell. A volume fraction of zero indicates the absence of that phase in the cell, while a volume fraction of one means the exclusive presence

of the phase. Level-set methods are another approach that provides a sharp representation of the interface [21]. A level-set function is used, where cells with negative level-set values belong to the first phase, while those with positive level-set values belong to the second phase. It's worth noting that level-set methods are known to exhibit mass loss in cases of significantly deformed interfaces [22]. Similar to VoF, a transport equation is employed to track the interface's evolution. Direct measurements of non-spherical bubbles and the determination of their surfaces are possible, but they require advanced optical systems and high-speed cameras [23, 24]. These experimental setups can also serve as valuable validation cases for computational fluid dynamics (CFD) simulations.

1.3 Multi-bubble systems

As previously mentioned, sonochemical reactors contain millions of bubbles. These bubbles can break up during collapse if the surface oscillations become too large. In such cases, several new bubbles are created. Additionally, bubble jets can cut through a bubble, although a jet itself does not create new bubbles; it may impact neighboring ones. A jet can occur when a large pressure gradient exists between two sides of a bubble. This large pressure difference results in a highly non-spherical collapse of the bubble, leading to the formation of a high-velocity liquid jet through the bubble. The processes of jetting and breakup typically occur during the collapse. Conversely, during the expansion phase, nearby bubbles may coalesce, resulting in the creation of a new bubble formed by the combination of two existing bubbles [25].

Even when bubbles are positioned farther apart and do not coalesce during the expansion phase, they still influence each other through various mechanisms. Firstly, cavitating bubbles generate high-amplitude shockwaves in the surrounding liquid. These shockwaves then propagate and impact other nearby bubbles, with the shockwave amplitude decaying with distance. Therefore, bubbles in proximity are most significantly affected by these shockwaves. Secondly, the presence of multiple bubbles in the liquid can lead to distortions in the acoustic field. Since each bubble may experience a different pressure change, the acoustic field is not uniform when multiple bubbles are involved. Thirdly, bubbles in the system dissipate the energy of the acoustic waves, which can have an impact on neighboring bubbles and the overall system. It's important to note that these effects between bubbles, while distinct, are interconnected. For example, one cause of energy dissipation is the emission of shockwaves by the bubbles, highlighting the complex interaction of factors in a multi-bubble system.

The majority of the aforementioned bubble interactions have unfavorable implications. From a chemical perspective, the primary objective is to achieve the highest possible compression of a bubble. However, processes such as bubble breakup or the formation of a jet can significantly hinder the compression. In these cases, a substantial portion of the energy is diverted towards the generation of a high-velocity liquid jet instead of producing the desired high pressures and temperatures within the bubble. The emission of high-amplitude shockwaves by a collapsing bubble is another disruptive factor, as these shockwaves can impact neighboring bubbles, potentially destabilizing their otherwise spherical surfaces. This destabilization can lead to bubble breakup or jet formation during subsequent collapse events. The distortion of the acoustic field around the bubble is also problematic, as it reduces the pressure amplitude and results in a smaller collapse. Additionally, distorted acoustic fields may give rise to significant pressure gradients, increasing the likelihood of bubble jet formation during collapse.

Multi-bubble systems can be simulated using the Keller-Miksis equation with the inclusion of a coupling term that takes into account the compressibility of the liquid and radiation coupling [26]. However, this method assumes spherical bubbles, and the coupling is treated as

instantaneous, neglecting the delay caused by the speed of sound. The investigation of multi-bubble systems using this approach is effective primarily when there is significant distance between the bubbles. In cases where the bubbles are closely positioned, the spherical shape is lost during collapse due to flattening [27]. Nonetheless, this approach still yields valuable insights. For instance, there are scenarios where the bubbles positively influence each other, allowing for higher compression ratios [28].

1.4 ALPACA compressible multiphase flow solver

The requirements for a hydrodynamic simulation of excited microbubbles are numerous:

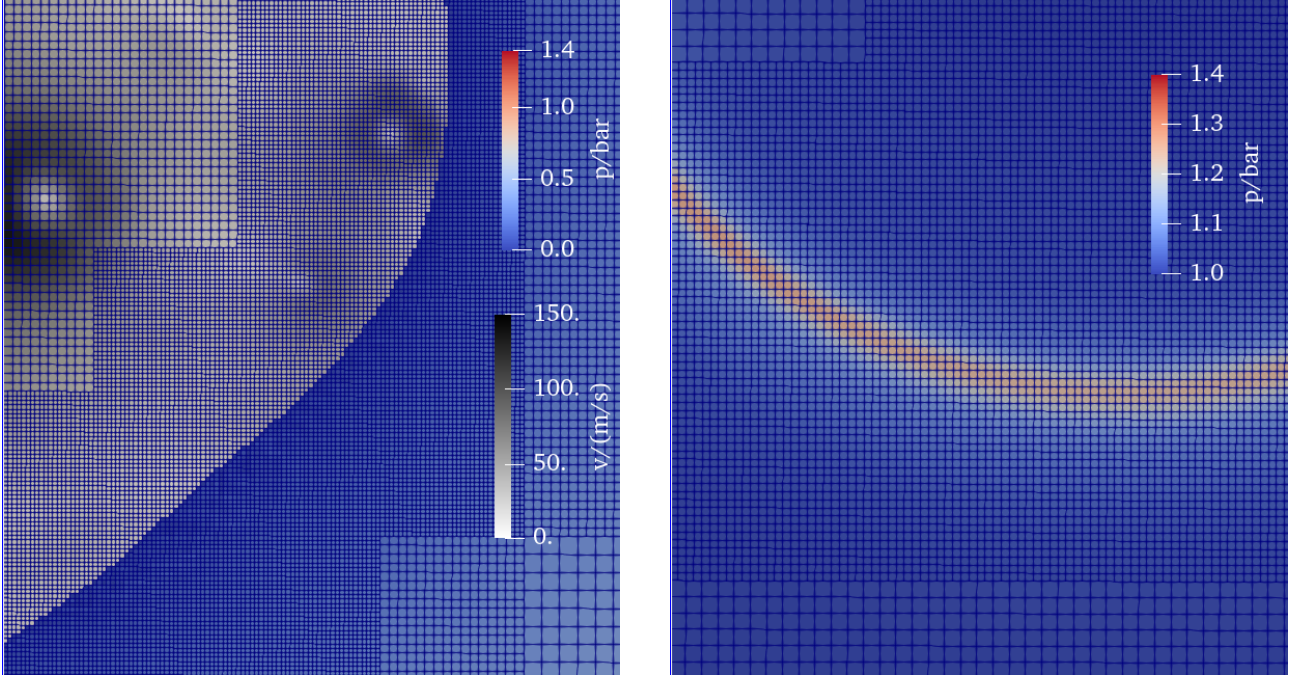
1. **Multiphase simulation:** It is necessary to perform a multiphase simulation that describes the interface and calculates surface tension.
2. **Compressible formulation:** A compressible formulation must be used, as the simulation needs to account for acoustic waves and collapsing bubbles.
3. **Handling of negative pressures:** High-pressure amplitudes can create negative pressures in the liquid, if the pressure amplitude p_A exceeds the ambient pressure p_0 . The presence of negative pressure in the liquid can pose challenges for certain methods of interface handling. For instance, the Volume of Fluid (VoF) method is known to encounter issues when negative pressure values coexist with large pressure gradients [17].
4. **Mass conservation:** It is essential to ensure the conservation of mass for the bubbles. As mentioned earlier, the level-set method is known to dissipate mass through the interface.
5. **Shockwave capture:** Cavitating bubbles can produce shockwaves, and accurately capturing these shockwaves is crucial for investigating their effects on the surroundings. This requires the use of numerical schemes with low artificial dissipation, such as high-order Weighted Essentially Non-Oscillatory (WENO) methods [29].
6. **Dealing with scale differences:** Large differences in scale must be addressed. The size of the computational domain should be at least one wavelength to simulate a standing wave. For a typical case, this means that the domain size, denoted as l , should be as follows,

$$l = \lambda = \frac{c}{f} = \frac{1500 \text{ m/s}}{100 \text{ kHz}} = 15 \text{ mm}.$$

The bubble sizes relevant to sonochemistry are typically below 50 μm , resulting in nearly three orders of magnitude difference between the domain size and the bubble size. This substantial scale difference necessitates specific numerical meshes.

In addition to the six criteria mentioned above, achieving a sufficient spatial resolution of the bubble is important. For collapsing bubbles, high temporal resolution is also required. Meeting these requirements, the ALPACA solver stands out as a good choice. It was purposefully developed for studying compressible and multiphase phenomena [30]. ALPACA allows for the application of high-order, non-dissipative numerical schemes to accurately capture shockwaves [21]. ALPACA's meshing process is relatively straightforward, employing a multiresolution algorithm that automatically refines the mesh as needed. In this algorithm, the maximum number of refinements, denoted as l_{max} , can be set. Based on this value and the domain size, the minimum cell size can be determined. Another crucial parameter is the tolerance of refinement, denoted as ε . Higher ε values result in the refinement of only the most important details with

the largest changes, which, in most cases, includes the bubble interface. Figure 1.3a displays the mesh on the interface of a collapsed bubble, illustrating the highest resolution at the interface, with cell size increasing farther away from it. By decreasing the ε value, other details, such as shockwave fronts, can also be refined. Figure 1.3b demonstrates the higher resolution at a wavefront.



(a) Mesh near a bubble interface

(b) Higher resolution at a shockwave front

Figure 1.3: Examples of multiresolution meshes in ALPACA bubble simulations using tolerance $\varepsilon = 0.01$. The coloring is based on the pressure in the liquid and on the velocity magnitude in the gas phase according to the colorbar.

In ALPACA the interface between phases is tracked by a sharp level-set method. The level-set method was mentioned previously in Section 1.2. The following transport equation is solved to track the interface,

$$\frac{\partial \phi(x, y, z)}{\partial t} + \mathbf{u}_\phi \cdot \nabla \phi(x, y, z) = 0, \quad (1.5)$$

where $\phi(x, y, z)$ is the level-set function. The level-set function gives the signed non-dimensional distance from the interface. The interface is given by

$$\phi(x, y, z) = 0, \quad (1.6)$$

and a value of $|\phi| = 1$ means that the point is one cell size away from the interface. Positive signs in ALPACA are assigned to the first phase, while negative signs represent the second phase. To preserve the non-dimensional distance property of the level-set, ALPACA employs level-set reinitialization in every time step. Additionally, a cutoff is applied in cells that are located farther away from the interface, limiting the absolute value of $|\phi|$ and preventing far-field fluctuations of the level-set. One notable drawback of ALPACA is the issue of mass loss at the interface, primarily due to the discretization errors in the level-set reinitialization [31]. As a countermeasure, it is essential to track the mass of the bubble in simulations to avoid excessive dissipation that could lead to non-physical outcomes.

The ALPACA simulations produce `xdmf` output files in HDF5 format, which can be imported into CFD post-processing softwares like Paraview. Given the large number of simulations, post-processing is fully automated for efficiency and reproducibility, utilizing Paraview’s Python extension. A post-processing script was developed by myself, which calculates various quantities, including equivalent radius, average bubble pressure, bubble mass. The initial script was detailed in my 2021 TDK work [32]. Subsequently, it has been updated to incorporate surface modes, and the script has been extended to handle multi-bubble simulations. While the Paraview GUI is still used for generating contour plots of scalar and vector fields, the scripting automation greatly enhances the efficiency of the process.

1.5 Goal

In this study, the ALPACA compressible multiphase flow solver is employed for conducting multi-bubble simulations. The study focuses on the validation of bubble simulations in ALPACA, as well as the setup for simulating multiple bubbles in an axisymmetric scenario. The primary objectives of this work can be summarized as follows:

1. Demonstrating that ALPACA can effectively simulate both spherical and non-spherical bubbles across a wide range of parameters relevant to sonochemistry. It’s worth noting that while some of this work was covered in last year’s TDK, several new results are introduced.
2. The Keller-Miksis equation can describe the radius–time curves of non-spherical bubbles, as long as the distortion is not too large. An additional goal is to determine a quantitative threshold for the equation’s applicability, based on the extent of non-sphericity.
3. After the numerical setup is thoroughly validated a multi-bubble simulation is created. The objective is to identify a distance limit beyond which bubbles have little influence on each other. In Section 1.3 several bubble interactions have been described, in theory their effect reduces with distance. Finding an exact limit is important from the practical point of view, as it enables the calculation of the maximum number of bubbles that can be accommodated within a given volume. This, in turn, allows us to estimate the reactor’s chemical output.
4. Different bubble interactions are explained based on the simulation results. The primary focus is on describing their effects on bubble dynamics, with the focus placed on the maximum compression, as this factor is closely related to the chemical yield.

2 Validation

The validation of ALPACA was the subject of the previous year's TDK, it included a detailed convergence study of the simulations for several parameter combinations [32]. Altogether 27 parameter combinations were tested and compared to measurements and other models. This section gives a short summary about previous work and highlights new findings not yet included in the previous papers.

2.1 Spherical validation

2.1.1 Simulation setup

An axisymmetric setup was used in the bubble simulations, as shown in Figure 2.1a. The x - and y -axes correspond to the radial and axial directions, respectively. The domain size is $b \times l$, where $l = n \cdot \lambda$ and $n \in \mathbb{N}^+$. The bubble was placed in the middle of the domain with its center at $y_0 = l/2$. The level-set can be initialized as

$$\phi(x, y) = -R_0 + \sqrt{x^2 + (y - y_0)^2}, \quad (2.1)$$

where R_0 is the initial bubble radius. The boundary conditions are illustrated in Figure 2.1a. A wall is present on the south and north sides, causing waves to be reflected. On the east side, a zero-gradient boundary condition is applied, while the west side serves as the axis of symmetry. The standing wave is generated through the initial conditions. The derivation of the velocity and density of a standing wave can be found in the Appendix at Section 5.2. The initial conditions in the liquid phase come from setting $t = 0$, in Equation (5.29)-(5.31),

$$p_l(x, y) = p_0, \quad (2.2)$$

$$u_l(x, y) = 0, \quad (2.3)$$

$$v_l(x, y) = -\frac{p_A}{c\rho_0} \sin(ky) \quad \text{and} \quad (2.4)$$

$$\rho_l(x, y) = \rho_0, \quad (2.5)$$

where p_l is the pressure, u_l is the x -directional velocity, v_l is the y -directional velocity, ρ_l is the density in the liquid phase and $k = 2\pi/\lambda$. The initial conditions in the bubble correspond to the equilibrium condition, that is

$$p_b(x, y) = p_0 + \frac{2\sigma}{R_0}, \quad (2.6)$$

where p_b is the bubble pressure, σ is the surface tension and R_0 corresponds to the equilibrium radius R_E . The initial velocities are zero and the density is set according to the ideal gas Equation of State (EoS),

$$u_b(x, y) = 0, \quad (2.7)$$

$$v_b(x, y) = 0 \quad \text{and} \quad (2.8)$$

$$\rho_b(x, y) = \frac{p_b(x, y)}{(\gamma_b - 1)c_V T_b}, \quad (2.9)$$

where u_b is the x -directional velocity, v_b is the y -directional velocity and ρ_b is the density in the gas phase (i.e. bubble). In both phases the stiffened gas EoS is used [33],

$$p = (\gamma - 1)\rho e - p_\infty, \quad (2.10)$$

where e is the internal energy and γ , p_∞ are the parameters. In the gas phase $p_{\infty,g} = 0$, thus the stiffened gas EoS results in the ideal gas law and $\gamma_g = 1.4$ is the ratio of specific heats. The speed of sound can be calculated from the parameters as,

$$c = \sqrt{\gamma_l \frac{p_{\infty,l} + p_0}{\rho_0}}. \quad (2.11)$$

For the spherical validation $\gamma_l = 4.4$ and $p_{\infty,l} = 6 \cdot 10^8$ Pa are adopted from the literature [34], which corresponds to $c = 1624.8$ m/s. The simulation settings are summarized in the Appendix in Table 5.1 under column #1.

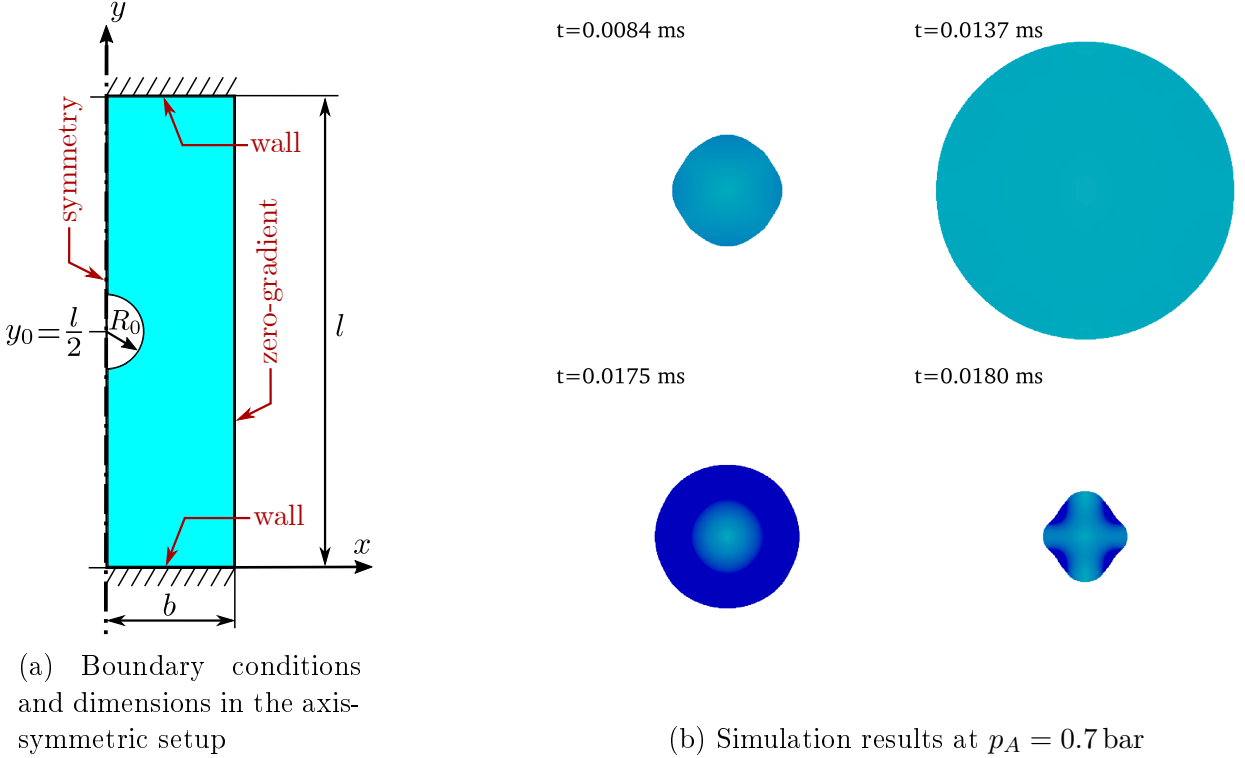


Figure 2.1: Spherical validation (*left*) setup (*right*) a simulation result

As we know already ALPACA can be used for spherical bubble simulations if the following conditions are met [35, 32]:

- The bubble resolution is large enough. Based on prior experiences, it has been established that the error and mass dissipation at the bubble interface are proportional to the cell size at the surface of the bubble. To attain the minimum cell size at the bubble interface, the multiresolution meshing parameters in the simulations must be configured accordingly. In the case of ALPACA, the interface can be meshed with the smallest cells if a low tolerance is set; in practice, $\varepsilon < 0.1$ achieves the desired mesh. The bubble resolution can be quantified as

$$D_{\text{cell}} = \frac{2R_0}{a_{\text{min}}}, \quad (2.12)$$

where R_0 is the bubble radius and a_{min} is the minimum cell size. Equation (2.12) expresses the number of cells along the bubble diameter, assuming the smallest resolution is used uniformly across the entire bubble. It is important to note that although resolution jumps might occur within the bubble, what matters most is the number of cells along

the circumference, which is always approximately πD_{cell} . For optimal results in modeling spherical dynamics, it is recommended to use $D_{\text{cell}} \geq 100$. Additionally, it's worth noting that mass loss is proportional to (D_{cell}^{-2}) , which means that doubling the resolution results in only one-fourth of the mass being dissipated on average.

- The simulation domain must be large enough. Previous research, as documented in my work [36], has indicated that in smaller domains, the standing wave can experience damping, particularly at high frequencies. In practice, it is advisable to set the width and length of the simulation domain to be at least equal to one wavelength to avoid this damping effect.

Based on the previous points, the bubble resolution was set to $D_{\text{cell}} = 218$ and the domain size was $3\lambda \times 3\lambda$ throughout the spherical validation.

2.1.2 Quantifying the non-sphericity

In my earlier research, the determination of a bubble's deviation from a perfect spherical shape was primarily reliant on visual assessment. Nevertheless, more precise and objective methods can be created for this purpose. The methods to quantify the *non-sphericity* of bubbles are all based on the surface modes a_i (see the first few modes in Figure 1.2). The overarching concept is to compute a single metric from these surface modes, allowing for the quantification of sphericity. This sphericity can be quantified using a variety of techniques.

1. Based on individual surface modes. The criterion for determining when a bubble can no longer be considered spherical is based on the condition that if any dimensionless surface mode amplitude surpasses a specified threshold M , the spherical shape is considered lost at a time $t = t^*$. Mathematically, this condition is expressed as,

$$\hat{a}_{\text{max}}(t^*) = \max_i \left(\frac{a_i(t^*)}{R(t^*)} \right) \geq M, \quad (2.13)$$

where a_i/R is the dimensionless mode amplitude. This method is straightforward, but it has a limitation. The drawback is that while it checks whether any individual mode exceeds the threshold M , it may not account for situations where several modes are close to M but none of them surpass it. As a result, a bubble can still be classified as spherical, even if it exhibits noticeable non-spherical characteristics. For example, as depicted in the two bubble shapes on the right side of Figure 2.2, both have $\hat{a}_{\text{max}} = 0.5$, but they display distinct visual differences, with one appearing almost broken up despite having the same \hat{a}_{max} .

2. Based on the sum of the surface modes squared. In this case, all surface modes are taken into consideration. The spherical shape is considered to be lost at time $t = t^*$ if

$$\hat{a}_{\text{avg}}(t^*) = \sqrt{\sum_{i=2}^N \left(\frac{a_i(t^*)}{R(t^*)} \right)^2} \geq M. \quad (2.14)$$

This method correctly assigns a significantly larger value to the bubble shape in the right of Figure 2.2.

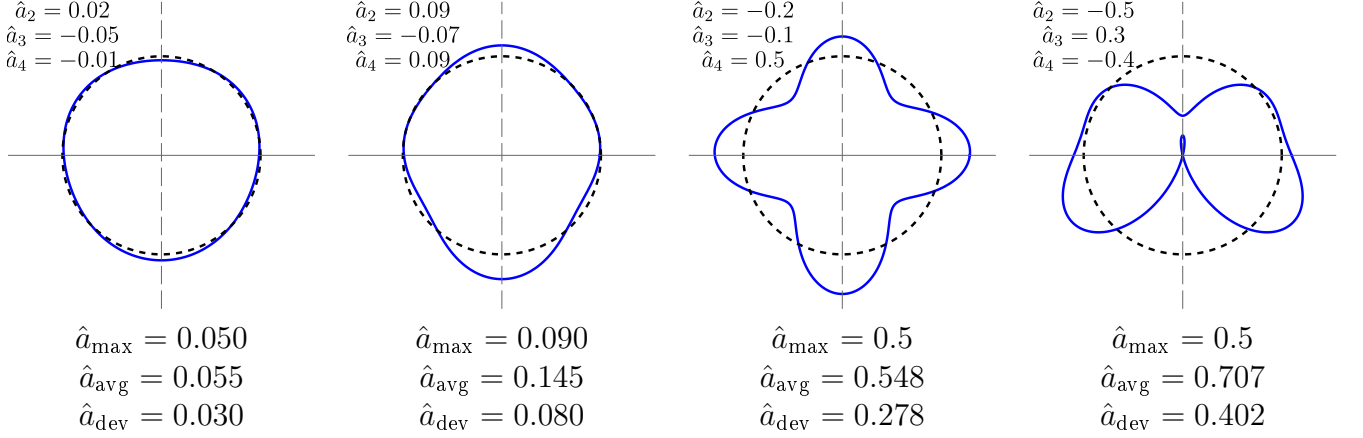


Figure 2.2: Different surface deformations and corresponding non-sphericity measures

3. Based on the deviation from the spherical shape. The bubble's surface can be described as $r(t, \theta)$ (see. Equation (1.4)) and the deviation from the perfect spherical shape can be represented as $R - r(t, \theta)$. Its square can be integrated in dimensionless form as

$$\hat{a}_{\text{dev}}^2(t) = \int_0^\pi \left(1 - \frac{r(t, \theta)}{R(t)}\right)^2 \sin(\theta) d\theta, \quad (2.15)$$

where $\sin(\theta)$ is employed as a weighting factor. This choice means that near the axis ($\theta \approx 0$ and $\theta \approx \pi$) the weight is relatively small, while it approaches 1 near the largest extent ($\theta = \pi/2$). The definition of θ was previously illustrated in Figure 1.2d. Interestingly, \hat{a}_{dev} can also be derived from the mode amplitudes

$$\hat{a}_{\text{dev}}^2(t) = \sum_{n=2}^{\infty} \left(\frac{2}{2n+1} \hat{a}_n^2(t) \right), \quad (2.16)$$

since the Legendre polynomials form an orthogonal basis and the a_i mode amplitudes can be regarded as coefficients of a generalized Fourier series. This also means that a generalized form of Parseval's identity can be applied. The derivation of this formula, along with a comprehensive explanation, is provided in Section 5.1 within the Appendix. In that case the spherical shape is lost at $t = t^*$ if

$$\hat{a}_{\text{dev}}(t^*) = \sqrt{\sum_{n=2}^{\infty} \frac{2\hat{a}_n^2(t^*)}{2n+1}} \geq M. \quad (2.17)$$

This approach also assumes that higher modes have progressively diminishing effects, which is visually evident in Figure 2.3. As the mode number increases, the area between the bubble's surface (continuous curve) and the ideal spherical shape (dashed line) becomes smaller. Therefore, it is apparent that a pure mode 4, for instance, causes less deviation from the spherical shape compared to a pure mode 2 with the same amplitude.

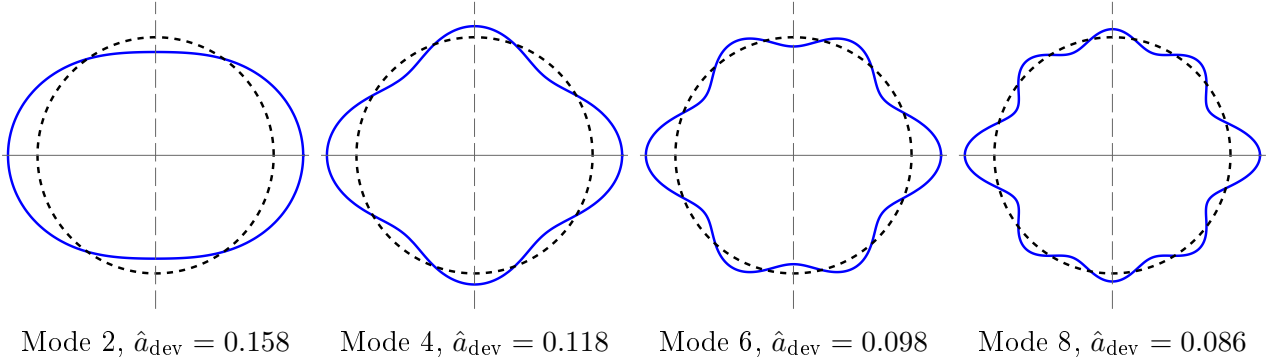


Figure 2.3: Pure bubble modes with $\hat{a}_i = 0.25$, $i = 2, 4, 6, 8$

Non-sphericity leads to a deviation from the Keller-Miksis equation, as this equation assumes perfectly spherical bubbles. The relative error in this context can be defined as,

$$E(t) = \frac{|\tilde{R}(t) - R_{KM}(t)|}{R_{KM}(t)}, \quad (2.18)$$

where $\tilde{R}(t)$ is the equivalent radius in the ALPACA simulation and $R_{KM}(t)$ is the radius predicted by the Keller-Miksis equation. The equivalent bubble radius is calculated from the bubble volume V_b as

$$\tilde{R}(t) = \sqrt[3]{\frac{3V_b}{4\pi}}. \quad (2.19)$$

With a clear definition for the error, all the necessary elements are in place to conduct simulations and determine the limit of non-sphericity within which the Keller-Miksis equation remains useful. To summarize, there are three methods to quantify non-sphericity, and examples of all three can be observed in Figure 2.2, \hat{a}_{avg} is based on the square sum of the modes and \hat{a}_{dev} is based on the integral of the weighted deviation from the spherical shape. The quantity \hat{a}_{max} is not used in the future as it cannot assess the non-sphericity properly.

Table 2.1: Time instances of reaching 10% error ($t_{10\%}^*$) and bubble split (t_{split}) and the mass lost at $t_{10\%}$

p_A/bar	0.1	0.2	0.4	0.7	1.0	1.5
$t_{10\%}^*/\text{ms}$	–	–	0.0364	0.0273	0.0185	0.0202
t_{split}/ms	–	–	0.0523	0.0285	0.0285	0.0273
$\hat{m}_l(t_{10\%})$	0.61%	1.30%	1.26%	0.36%	0.50%	0.39%

2.1.3 Results

For the spherical validation, multiple cases were examined with different frequencies and pressure amplitudes. In the discussion that follows, we focus on a specific case where $f = 120$ kHz and the pressure amplitude varies as $p_A = 0.1 \text{ bar} \dots 1.5 \text{ bar}$. In Figure 2.1b snapshots of the bubble can be seen, showing its expansion and subsequent collapse. Figure 2.4 displays the six simulations conducted at $f = 120$ kHz with varying pressure amplitudes. The dashed black line in the figures represents the solution of the Keller-Miksis equation. Notably, for low pressure amplitudes ($p_A \leq 0.4 \text{ bar}$) there is a remarkable agreement between the simulations and the Keller-Miksis equation. However, for higher pressure amplitudes, the simulation results start

to deviate. This deviation occurs because the bubbles are no longer perfectly spherical, as evidenced in Figure 2.1b at $t = 0.018$ ms, while the Keller-Miksis equation assumes a spherical bubble.

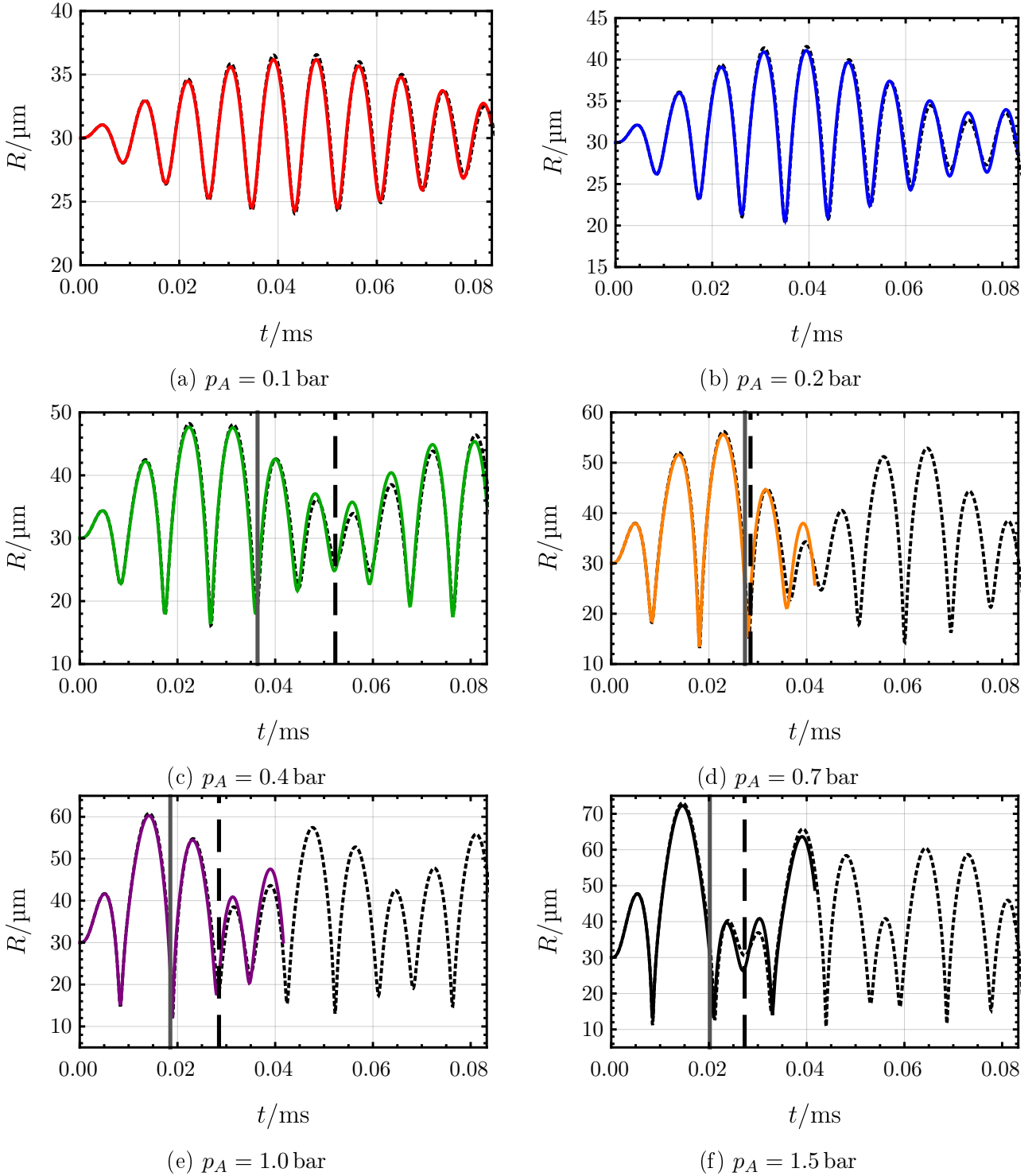


Figure 2.4: Spherical validation results at $f = 120$ kHz. Dashed black line depicts Keller-Miksis, vertical gray lines depict the 10% error threshold (t_{10}), vertical dashed black lines show the breakup of the bubbles (t_{split}).

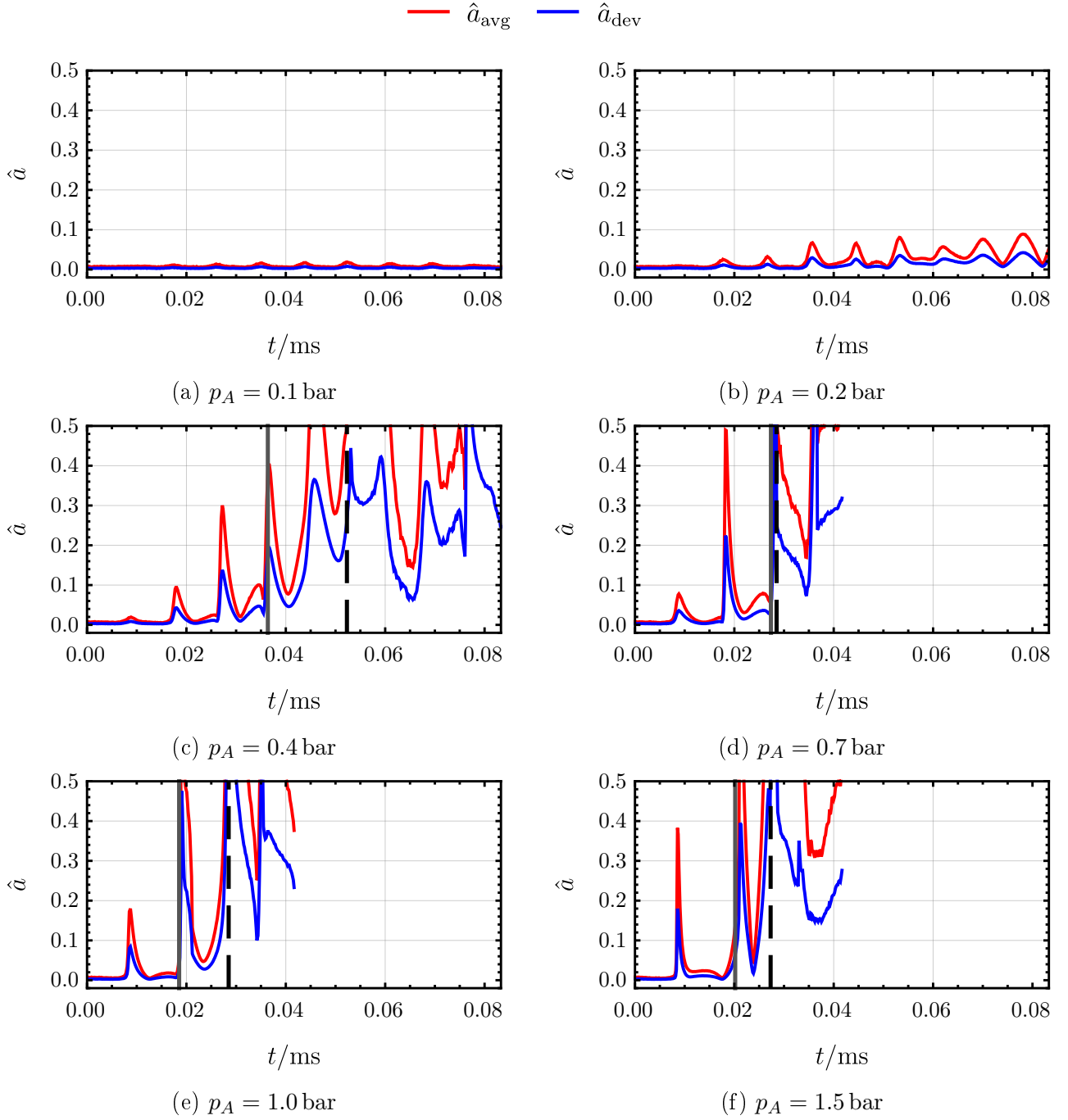


Figure 2.5: Non-sphericity throughout the simulations based on both definitions (\hat{a}_{avg} and \hat{a}_{dev}), the vertical gray and black lines show the 10% error and the split up times.

In the simulations the relative error E reaches 10% at the vertical gray lines in Figure 2.4, these specific time instances are called $t_{10\%}$. Higher pressure amplitudes cause the bubble to break up into pieces after a few cycles, the time of split-up is shown in Figure 2.4 with dashed black lines, and these time instances are denoted as t_{split} . Following the break-up the bubble pieces still periodically expand and collapse, they can even coalesce again into a larger bubble. When several small bubbles are present the total volume of all bubbles is used to calculate a single equivalent bubble radius. The mentioned time instances, the average error until $t_{10\%}$ and the mass loss until $t_{10\%}$ is summarized in Table 2.1. The mass lost \hat{m}_l is defined as

$$\hat{m}_l(t) = 1 - \frac{m(t)}{m_0}, \quad (2.20)$$

where m_0 is the starting mass and $m(t)$ is the mass at time t . The mass loss is less than 1.3% in each case as evidenced from the table.

The non-sphericity throughout the six simulations is depicted in Figure 2.5. In this figure, the red and blue lines represent the definitions of non-sphericity using \hat{a}_{avg} and \hat{a}_{dev} . It is evident that for higher pressure amplitudes ($p_A \geq 0.4$ bar) the spherical shape is lost during bubble collapses ($t \approx 0.01$ ms, $t \approx 0.02$ ms ...). During these instances, significant spikes in the non-sphericity can be observed according to both measures. However, if the spikes in \hat{a} are not excessively large, the deviation from the Keller-Miksis equation remains small. For instance, consider the third bubble collapse at $p_A = 0.4$ bar around $t \approx 0.028$ ms. This event results in a spike of $\hat{a}_{\text{avg}} = 0.29$ and $\hat{a}_{\text{dev}} = 0.14$; however, this spike does not cause the error to increase significantly, and in the 4th cycle there is still good agreement between the Keller-Miksis equation and the ALPACA simulation.

Based on the observations from Figure 2.5 it can be concluded that if the spikes in \hat{a} during a bubble collapse remain below the threshold

$$\hat{a}_{\text{avg}} < 0.2 \quad \text{and} \quad \hat{a}_{\text{dev}} < 0.1, \quad (2.21)$$

then the subsequent expansion-collapse cycle can be accurately described by the Keller-Miksis equation, which is a conservative estimate. In many cases even larger spikes in non-sphericity are possible without exceeding a 10% error in the bubble radius. This implies that the Keller-Miksis equation can effectively approximate the radial dynamics of an acoustically excited bubble, even when the bubble is not perfectly spherical. This is because minor, stable surface oscillations do not induce a significant change in the radial dynamics.

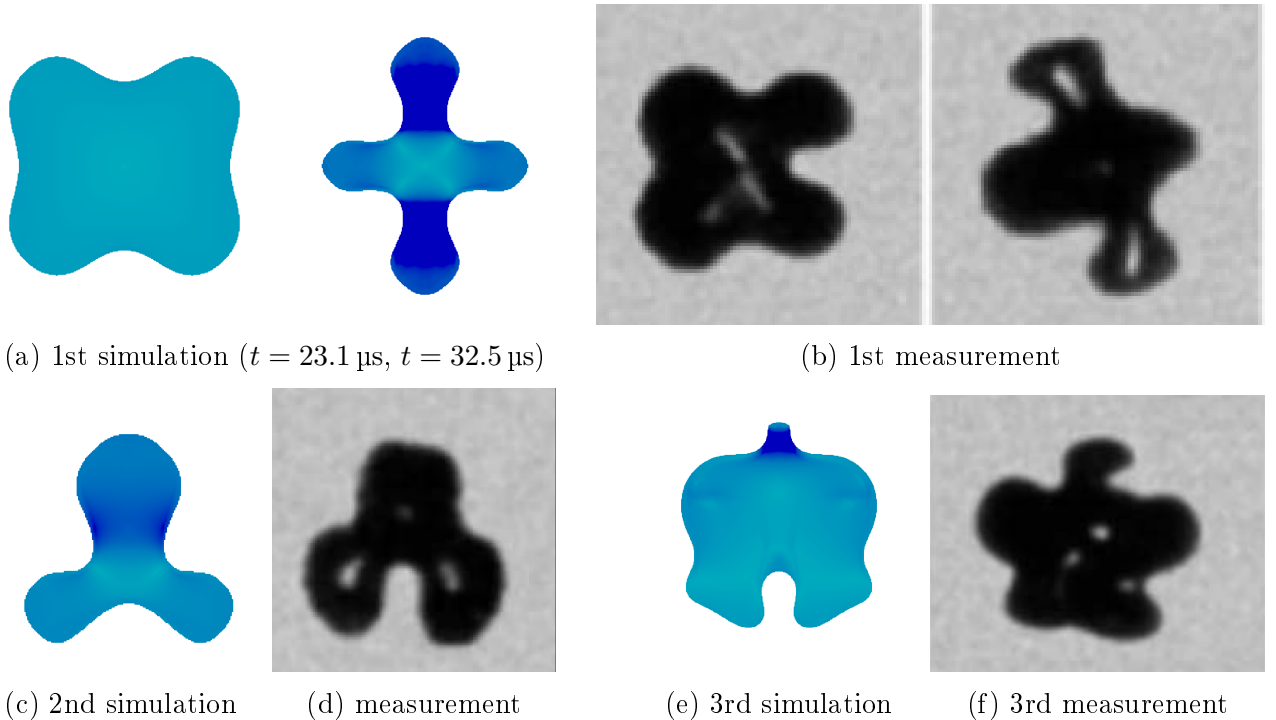


Figure 2.6: Modes forming in the ALPACA simulation and the measurement of Verluis. The simulation results are colored based on the velocity magnitude, the pictures are taken by high-speed cameras in the measurement.

2.2 Non-spherical Validation

The validation of ALPACA for non-spherical bubble oscillations was previously discussed in a TDK study, and it demonstrated good agreement between measurements and simulations in terms of the bubble shape. Additionally, the dominant surface mode could be reliably determined [32]. Figure 2.6 provides a comparison between ALPACA simulations and measurements by Verluis [37]. Each measurement and simulation used the same parameters, except for the bubble radius. In the first case, with $R_0 = 36 \mu\text{m}$, a 4th surface mode oscillation was observed in both the measurement and simulation. Similarly, a good agreement can be found for the 3rd mode oscillation in the second simulation ($R_0 = 30 \mu\text{m}$) and also in the third simulation ($R_0 = 44 \mu\text{m}$) for the 5th mode. Detailed information on the simulation parameters and settings can be found in Appendix Table 5.1 column #2. These results demonstrate that ALPACA is capable of reproducing the measurements effectively, indicating its ability to accurately simulate non-spherical bubbles.

2.3 Cross validation with ROM

Both ALPACA and the Reduced Order Model (ROM) have been validated using measurements. The ROM, which consists of a coupled system of ordinary differential equations, is computationally efficient and can simulate a single case in less than a minute. However, it is primarily applicable for small surface perturbations. On the other hand, ALPACA simulations are more computationally intensive and take hours to complete because they involve the full hydrodynamics solution. Nevertheless, ALPACA can handle larger surface oscillations and even simulate bubble breakups. The concept of cross-validation involves comparing the results obtained from both the ROM and ALPACA. By creating a small initial perturbation in both methods, several observations can be made:

1. If the bubble is spherically stable, the initial perturbation gradually damps down, this behavior allows us to observe the spherical stability limit.
2. Surface mode oscillations that remain stable can occur beyond the spherical stability limit. These cases can be categorized based on their dominant modes.
3. Surface oscillations can become unstable, this leads to a bubble breakup. By monitoring this behavior, we can also determine the limit at which breakup occurs.

2.3.1 Initial shape in ALPACA

The bubble must be initiated from a perturbed state with a small perturbation. The most challenging aspect is configuring the level-set function. Let the initial level-set function be,

$$\phi_0(x, y) = -\rho \cdot R_0 + \sqrt{x^2 + \beta \cdot x \cdot (y - y_0) + \alpha \cdot (y - y_0)^2}, \quad (2.22)$$

where α , β are parameters to control the even and odd mode amplitudes, while ρ must be determined to ensure that the initial volume V_0 matches that of a sphere with a radius R_0 ($V_0 = 4R_0^3\pi/3$). Based on the initial level-set the surface mode amplitudes can be calculated for $t = t_0$, and α , β can be tuned to achieve the desired perturbation. The level-set defines the initial interface $\phi_0 = 0$ as

$$\rho^2 R_0^2 = x^2 + \beta x \cdot (y - y_0) + \alpha (y - y_0)^2. \quad (2.23)$$

A coordinate transform to the polar coordinates centered in y_0 is the following,

$$x = r \cdot \sin(\theta) \quad \text{and} \quad y = y_0 - r \cdot \cos(\theta). \quad (2.24)$$

Applying the transformation to Equation (2.23), the $r(\theta)$ function can be found,

$$r(\theta) = \frac{\rho R_0}{\sqrt{\sin^2(\theta) + \alpha \cos^2(\theta) - \beta \sin(\theta) \cos(\theta)}}. \quad (2.25)$$

A valid set of parameters to describe small initial deformations is,

$$\alpha = 0.92, \quad \beta = 0.3 \quad \text{and} \quad \rho = 0.9781. \quad (2.26)$$

The bubble surface $r(\theta)$ is determined as shown in Equation (2.25). Using this information, the mode amplitudes can be calculated, and the formula for deriving these mode amplitudes can be found in the Appendix in Equation (5.8). Table 2.2 lists the dimensionless mode amplitudes for the above-mentioned parameters. This initial perturbation results in a non-sphericity of the initial shape, with $\hat{a}_{\text{avg}} = 0.062$ and $\hat{a}_{\text{dev}} = 0.034$, therefore, the perturbation can be considered small.

Table 2.2: Dimensionless modes amplitudes, $\hat{a}_i = a_i/R$

\hat{a}_0	\hat{a}_2	\hat{a}_3	\hat{a}_4	\hat{a}_5	\hat{a}_6	\hat{a}_7	\hat{a}_8
0.99651	0.03142	-0.04999	-0.00768	-0.01618	-0.00054	-0.00673	0.00003

2.3.2 Simulation settings

Three parameter studies were conducted, and the common parameters for each can be found in column #3 of Table 5.1. In each parameter study, the frequency was held constant while the bubble radius and pressure amplitude were adjusted in the ranges specified in Table 2.3. The output data from the ROM simulation was provided by Peter Kalmar, the data was further process by myself. For each combination of parameters the dominant mode had to be identified. The dominant mode is the one with the largest amplitude. If the dominant mode amplitude does not reach $\hat{a}_i = 0.001$, then the bubble is considered spherically stable.

Table 2.3: Parameters used in the studies

Frequency f	Equivalent radius R_E	Pressure amplitude p_A
30 kHz/120 kHz/480 kHz	0 μm . . . 80 μm	0 kPa . . . 150 kPa

The dominant modes are plotted in the (R, p_A) plane for the $f = 30$ kHz case in Figure 2.7. The various colors correspond to the different modes, as indicated in the legend. The gray line shows the limit of spherical stability, below which the bubble is considered spherical according to the ROM. Above the spherical stability line, where there is no color in the plot the bubble undergoes breakup.

2.3.3 Results

Using the ROM results as a reference, several ALPACA simulations are conducted and compared. The radius–time and mode amplitude–time curves for several pressure amplitude and $R_0 = 47.5 \mu\text{m}$ are presented in Figure 2.8. From these simulations the following observations can be made:

1. For a low pressure amplitude ($p_A = 10$ kPa) the initial perturbation in the modes damp down as illustrated in Figure 2.8b. The bubble is considered spherically stable in that case, and a gray point is marked in Figure 2.7 at the coordinates ($R = 47.5$ μm , $p_A = 10$ kPa). This point falls below the spherical stability limit, aligning with the ROM results.
2. For pressure amplitudes $p_A = 32$ kPa and $p_A = 36$ kPa, there is an initial large mode 3 oscillation observed during the first few acoustic cycles. However, this dampens down and a stable mode 2 oscillation remains. The ROM predicts a dominant mode 2 for $p_A = 32$ kPa and a dominant mode 4 for $p_A = 36$ kPa, which differs from ALPACA results in the second case.
3. For a high pressure amplitude ($p_A = 42$ kPa), the initial perturbation grows, leading to bubble breakup at $t_{\text{split}} = 0.072$ ms. This breakup event is indicated by a vertical dashed line in Figure 2.8h. For this particular parameter combination the ROM also predicts a breakup.

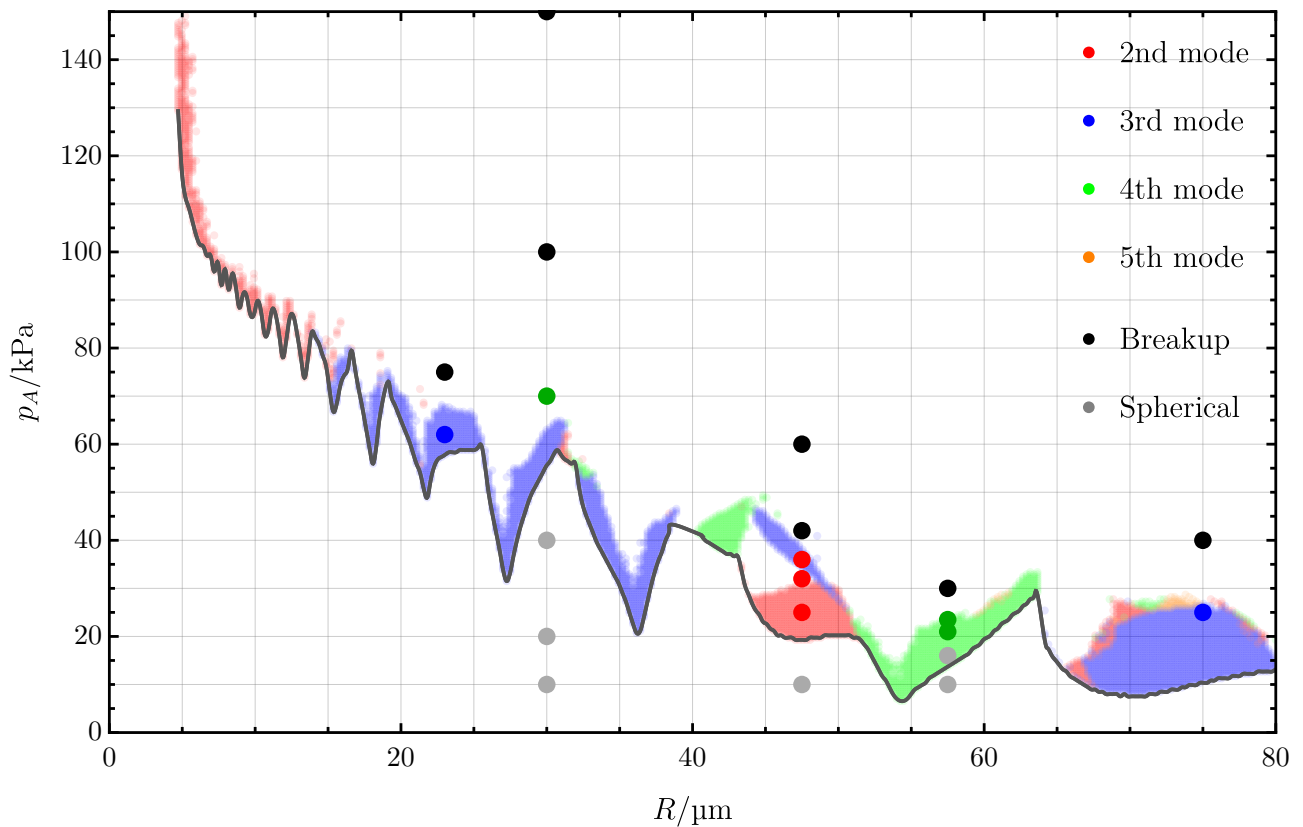


Figure 2.7: Parameter study results at $f = 30$ kHz, the background is colored based on the ROM results and the dots show the ALPACA results.

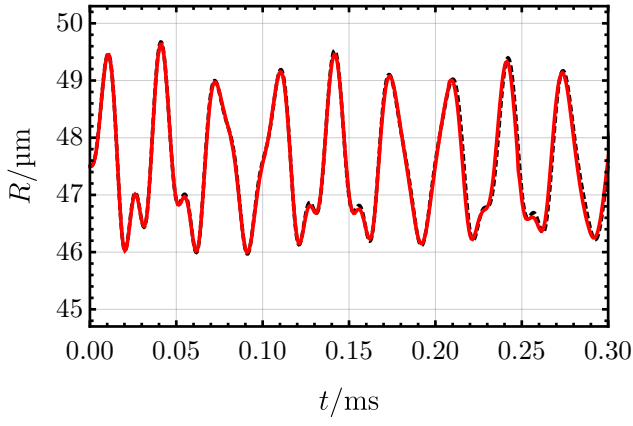
In Figure 2.8 the radial dynamics is also depicted, and a remarkable agreement can be found between the ALPACA (red line) and the ROM (black dashed line). The same classification process was applied to all ALPACA simulations. In total, 62 ALPACA simulations were conducted, with each simulation running for 24 hours on the SUPERMUC-NG supercomputer, utilizing 1 compute node with 36 cores. In most cases, this computing time was sufficient to run the simulations for at least 10 acoustic cycles, as shown in Figure 2.8, enabling the analysis of long-term behavior. For lower frequencies, simulating the same number of acoustic cycles

requires more time, as the period time is longer, and more time steps are necessary. Simulating smaller bubbles necessitates a reduction in cell size, and in accordance with the CFL condition, the time step size is also reduced. To account for these factors, the simulations were extended for an additional 24 hours in the case of low frequencies and small bubbles.

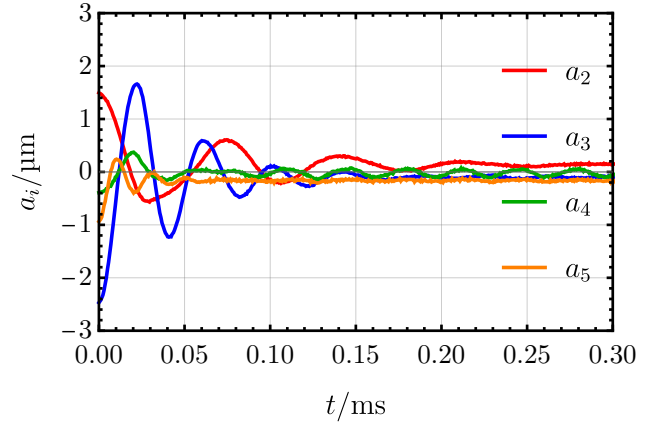
The results of the simulations are presented in Figure 2.7, 2.9 and 2.10 overlaid on the ROM results. Below the spherical stability limit, as determined by the ROM (gray line), the bubbles in the ALPACA simulation also exhibit spherical stability. Slightly above the stability limit, the surface mode oscillations remain small and cannot be seen in the ALPACA simulations in some cases. For example in Figure 2.7, at ($R = 57.5 \mu\text{m}$, $p_A = 15 \text{kPa}$), the modes amplitudes are so small that they cannot be resolved by ALPACA with the given settings.

The stable surface mode oscillations generally show good agreement between the ROM and the ALPACA simulations. However, there are some cases where discrepancies occur, particularly for higher surface modes, as exemplified in Figure 2.9 at ($R = 42.5 \mu\text{m}$, $p_A = 25 \text{kPa}$) and Figure 2.10 at ($R = 18.6 \mu\text{m}$, $p_A = 120 \text{kPa}$). Additionally, cases with high surface mode amplitudes above the validity limit can also exhibit differences, such as $\hat{a}_2 > 0.3$ in Figure 2.9 at ($R = 17.5 \mu\text{m}$, $p_A = 60 \text{kPa}$). It is important to note that bubble breakup consistently occurs above the region of stable surface oscillations. However, there are instances where the bubble does not break up, although predicted by the ROM (e.g. Figure 2.10, $R = 10.5 \mu\text{m}$, $p_A = 80 \text{kPa}$). This can be attributed to the validity limit, as it assumes small perturbations in the surface and may not accurately capture the behavior in cases with significant surface perturbations.

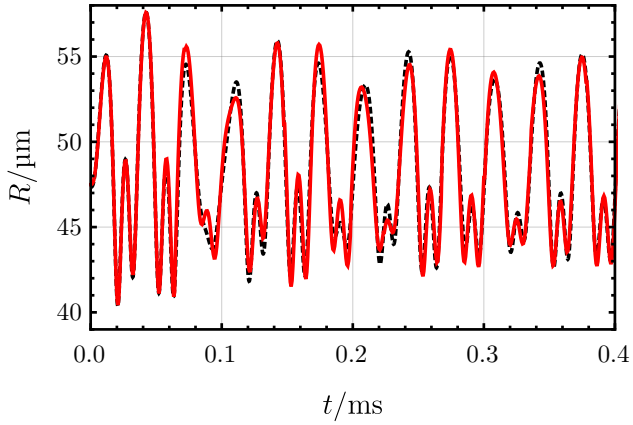
Out of the 62 ALPACA simulations, 54 of them, or 87%, align with the ROM predictions. The simulation results are summarized in Table 5.2 in the Appendix. Based on these observations, it can be concluded that the spherical stability limit and the stable surface mode oscillations are accurately predicted by the reduced order model, as long as the validity limit of the ROM is not exceeded. Currently, the reduced order model is known to provide good agreement with measurements up to $\hat{a}_i \approx 0.2$, meaning that the mode amplitudes should be at most 20% of the bubble radius [16]. In summary, these results mean that ALPACA can indeed be used for non-spherical bubble oscillations, as the spherical stability limit and stable surface mode oscillations are predicted well in most cases.



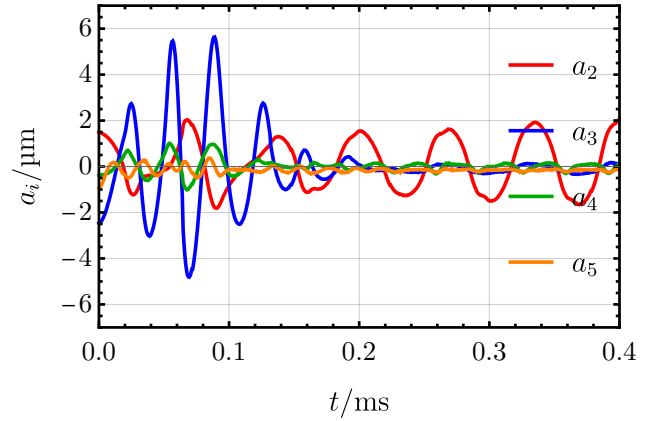
(a) $p_A = 10$ kPa, radius



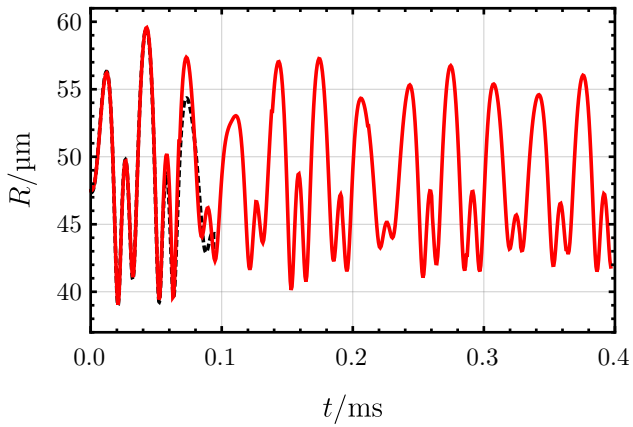
(b) $p_A = 10$ kPa, modes



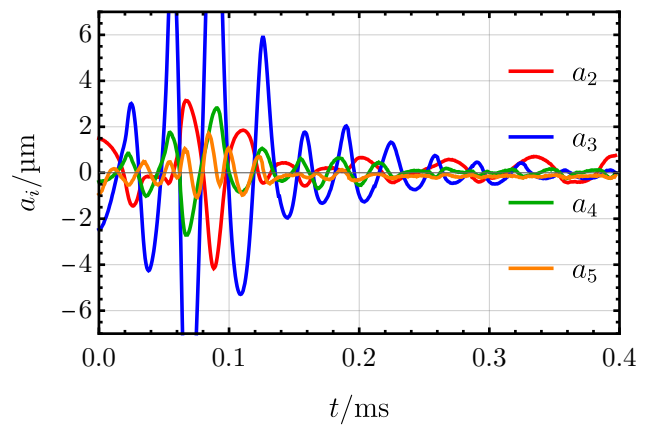
(c) $p_A = 32$ kPa, radius



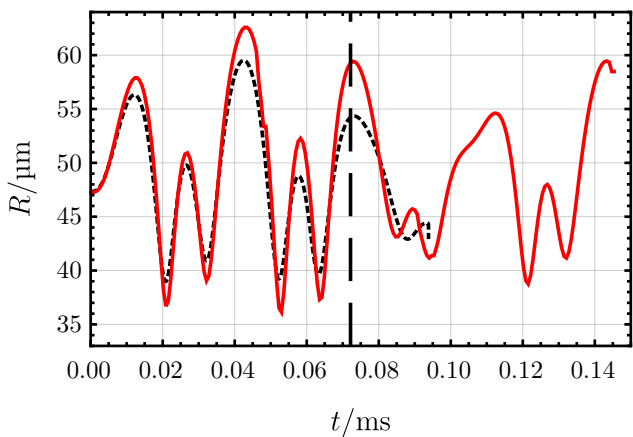
(d) $p_A = 32$ kPa, modes



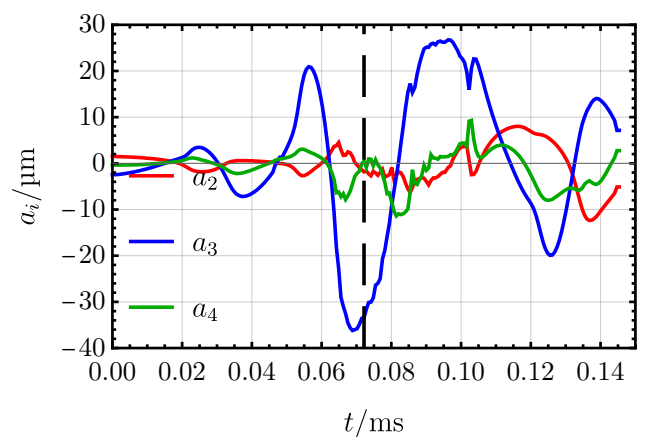
(e) $p_A = 36$ kPa, radius



(f) $p_A = 36$ kPa, modes



(g) $p_A = 42$ kPa, radius



(h) $p_A = 42$ kPa, modes

Figure 2.8: Radius and mode amplitudes for $R_0 = 47.5$ μm in ALPACA (Black dashed: ROM)

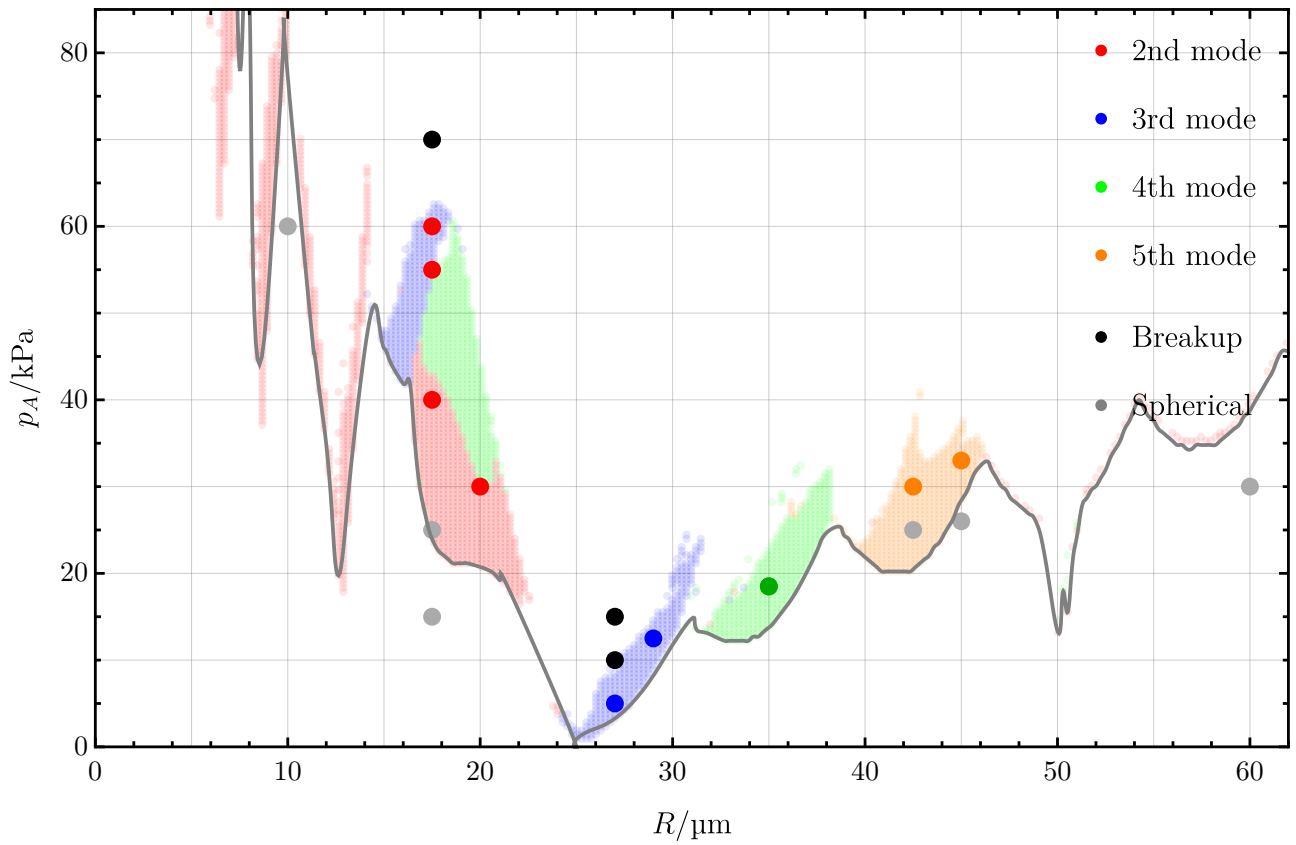


Figure 2.9: Parameter study results at $f = 130$ kHz

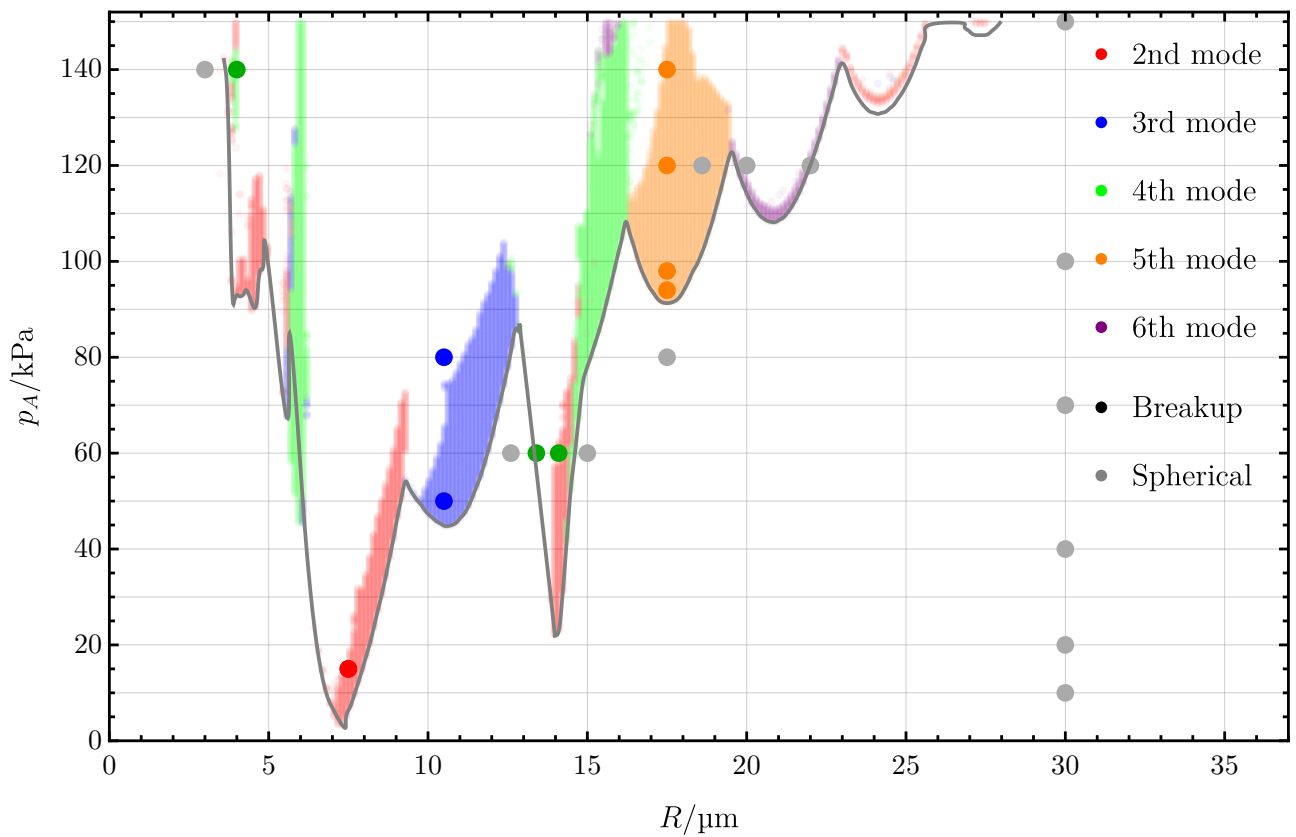


Figure 2.10: Parameter study results at $f = 480$ kHz

3 Multi-bubble systems

In the previous section, it became evident that ALPACA is well-suited for accurately simulating individual bubbles. However, single bubble simulations in ALPACA, in most instances, do not yield new insights, as simpler models like the Keller-Miksis equation or the ROM can effectively describe the behavior of individual bubbles. Conversely, systems composed of multiple bubbles are considerably more challenging to model using these simpler approaches, and ALPACA can be a powerful tool for analyzing such complex scenarios. The objective of this section is to determine the point at which bubbles have minimal influence on each other, as this threshold holds practical significance for approximating the maximum number of bubbles in a reactor. By establishing this maximum number, it becomes possible to predict the chemical output of a reactor, as the output of a single-bubble is already known [38].

3.1 Setup

The axisymmetric model is kept to mitigate computational costs, but this choice limits the study to a row of bubbles. While using standing waves for validation made sense in single bubble simulations, as many experiments also employ standing waves [23], for future applications, the need for a standing wave might not be imperative. The most significant bubble collapse typically occurs within the first few acoustic cycles, and chemical equilibrium is usually reached after a few significant collapses [38]. At this point, no further useful output product is generated. It may suffice to employ a traveling acoustic wave with only a few cycles for future applications. In the upcoming multi-bubble simulations, only a single acoustic cycle is used.

Figure 3.1a illustrates the simulation setup, featuring two bubbles of the same size situated within a domain of length $l = 2\lambda$ and width b . The initial equilibrium bubble radius R_0 is the same for both bubbles, while the distance between the centers of the bubbles is referred to as D , and the gap between the bubble surfaces is labeled as $d = D - 2R_0$. The center of the southern bubble is precisely located at $y = \lambda + R_0$. Based on the previously defined quantities a dimensionless bubble distance D^* can be derived as

$$D^* = \frac{D}{R_0}. \quad (3.1)$$

Initially, the bubbles are in a state of equilibrium, and the fields are set up as described in Equation (2.6)-(2.9). Boundary conditions are applied as follows: a symmetry boundary condition on the west, and zero-gradient type boundary conditions on all other sides. The initial conditions in the liquid phase are defined piecewise. In the north side (domain one), the liquid is at rest,

$$p_{l,1}(x, y) = p_0, \quad (3.2)$$

$$u_{l,1}(x, y) = 0, \quad (3.3)$$

$$v_{l,1}(x, y) = 0 \text{ and} \quad (3.4)$$

$$\rho_{l,1}(x, y) = \rho_0. \quad (3.5)$$

where $p_{l,1}$, $u_{l,1}$, $v_{l,1}$ and $\rho_{l,1}$ denote the pressure, x , y -directional velocity and the density in the first domain, respectively. In second domain, an acoustic wave is defined to travel to the north. The equations for traveling waves are derived from the continuity and the Navier-Stokes equation in 1D in the Appendix (see Section 5.2). The wave is set according to Figure 3.1a. First, the negative pressure reaches the bubble, causing it to expand. Then, during the positive

pressure part, the bubble collapses swiftly. By setting $t = 0$ in Equation (5.32)-(5.34), the initial conditions are as follows,

$$p_{l,2}(x, y) = p_0 + p_A \sin(ky), \quad (3.6)$$

$$u_{l,2}(x, y) = 0, \quad (3.7)$$

$$v_{l,2}(x, y) = \frac{p_A}{c\rho_0} \sin(ky) \text{ and} \quad (3.8)$$

$$\rho_{l,2}(x, y) = \rho_0 + \frac{p_A}{c^2} \sin(ky), \quad (3.9)$$

where c is the speed of sound, p_A is the pressure amplitude and $k = 2\pi/\lambda$. The initial pressure in the simulation is illustrated in Figure 3.1b for $p_A = 1.5$ bar. It is also evident that the simulation domain is significantly larger than the bubble size in each direction. The parameters for the simulations can be found in Table 5.1 in column #4 in the Appendix.

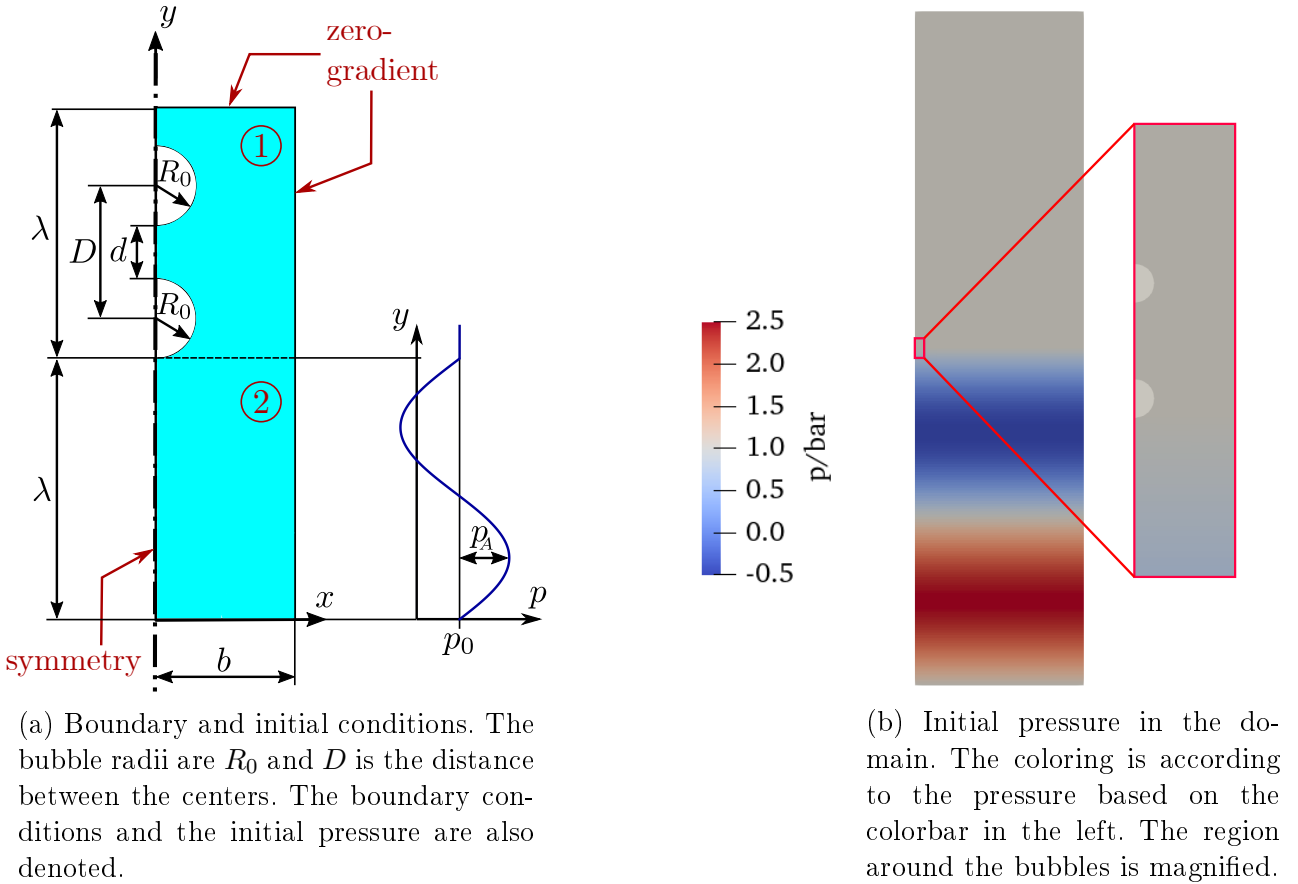


Figure 3.1: Boundary and initial conditions in the multi-bubble simulations

Typical results of multi-bubble simulations are depicted in Figure 3.2. The top row shows the acoustic wave traveling north, while the bottom row illustrate the bubbles. It can be observed that the bubbles expand during the negative pressure phase of the excitation. For example, the bubbles have a much larger radius at $t = 11.62 \mu\text{s}$ than initially. During the positive pressure phase, the bubbles collapse, as seen at $t = 16.83 \mu\text{s}$. The bottom bubble is already collapsed, as the acoustic wave reaches it first. During the collapse, a pressure wave is emitted from the bubbles, and these waves can be observed at $t = 22.33 \mu\text{s}$. The strength of the collapse, the amplitude of the emitted pressure wave, and the shape of the bubble after collapse all depend on the distance between the bubbles.

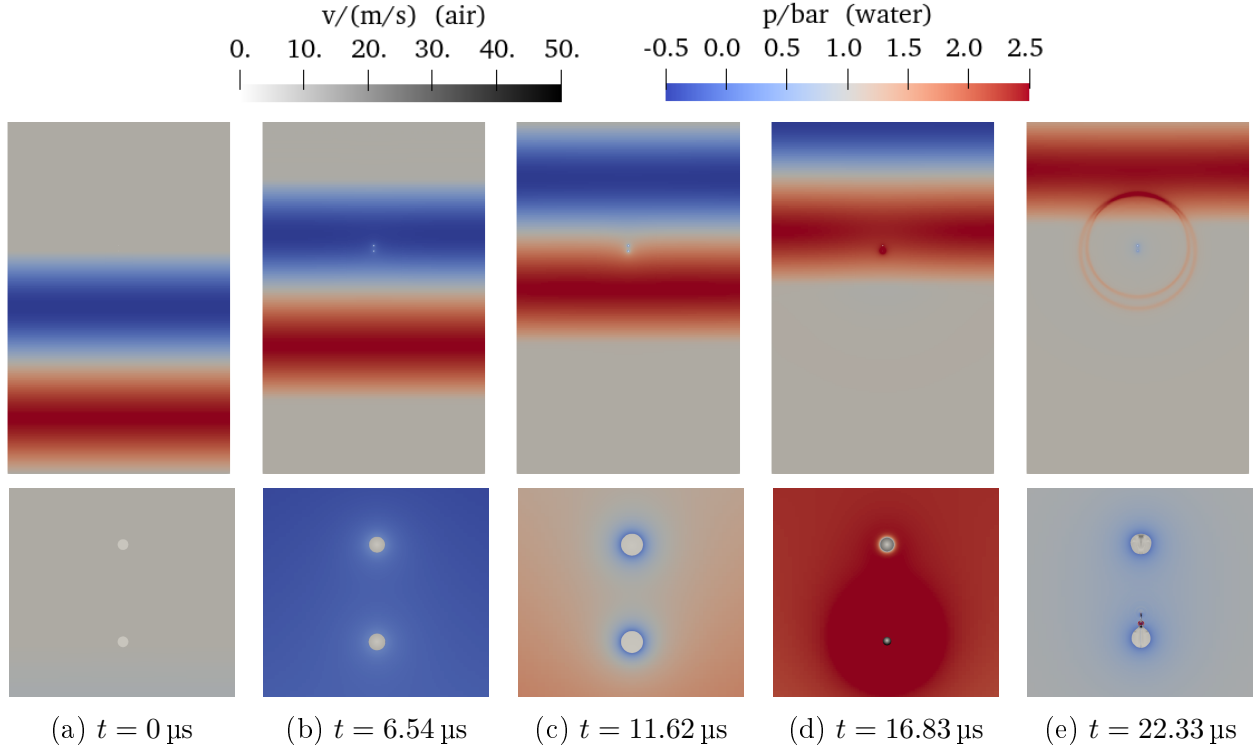


Figure 3.2: Typical result of multi-bubble simulations at $f = 50$ kHz

3.2 Convergence

It is known that single-bubble simulations converge as the resolution is increased. A similar study was conducted for a multi-bubble system, starting with a coarse mesh characterized by $D_{\text{cell}} = 88$ and a maximum multiresolution level of $l_{\text{max}} = 8$. Two $R_0 = 40 \mu\text{m}$ bubbles were placed $D = 180 \mu\text{m}$ away from each other, resulting in $D^* = 4.5$, the rest of the settings were already described in the previous section. The maximum resolution level was then increased to $l_{\text{max}} = 9$, which resulted in the halving of the cell size at the bubble interface. Finally, l_{max} was increased to 10. This mesh refinement approach focuses exclusively on enhancing the resolution near the bubble interface, while maintaining the same resolution in regions farther away. Table 3.1 provides an overview of the mesh statistics for all three cases. As the number of levels is increased, the bubble resolution doubles, and the cell size at the interface is halved with the introduction of each additional level. However, it is worth noting that the total cell count does not even double. Figure 3.3 illustrates the meshes in proximity to the bubble. In the case of the coarse mesh, the entire bubble is uniformly resolved with the same cell size. As we transition to higher resolutions, only the bubble's interface is resolved with the minimum cell size, and there are noticeable resolution jumps within the interior of the bubble.

Table 3.1: Mesh statistics for different resolutions

Resolution	l_{max}	D_{cell}	#Cells	#Cells in bubbles
Coarse	8	88	51 712	6 036
Medium	9	175	90 112	20 278
Fine	10	350	159 232	51 134

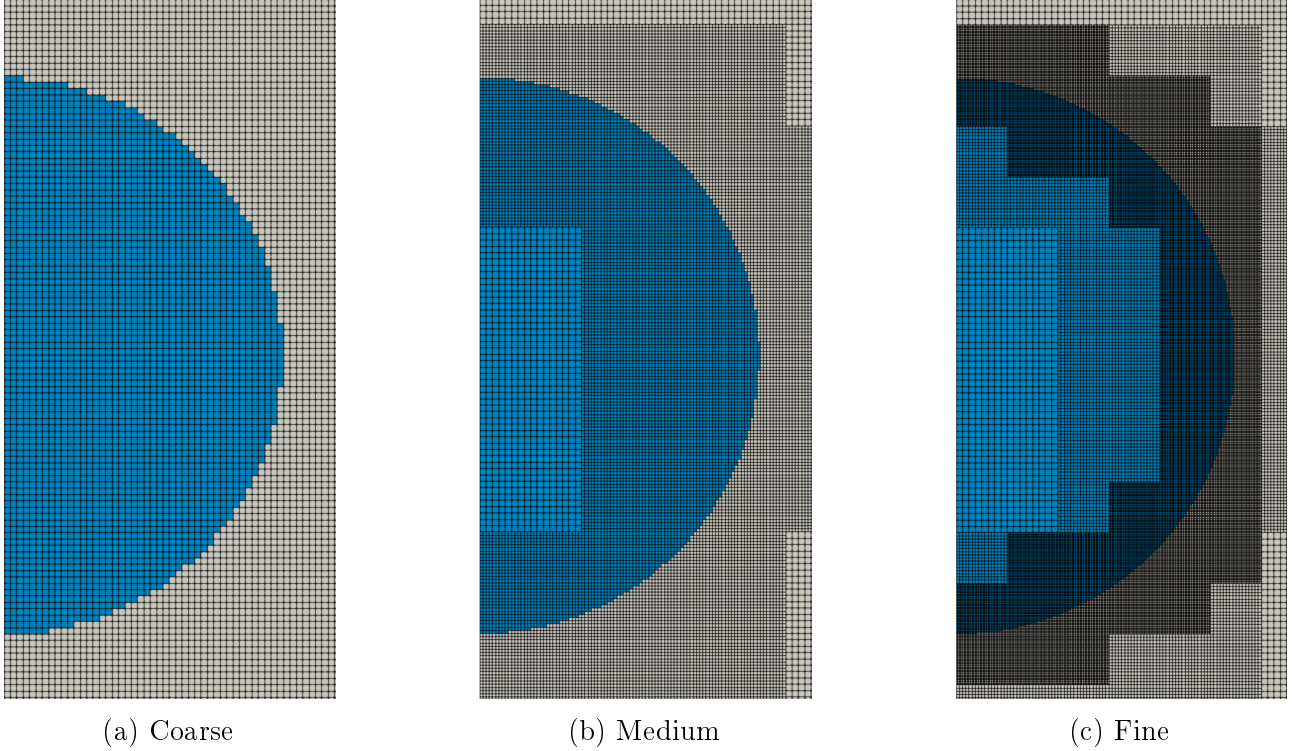


Figure 3.3: Different mesh resolutions near the bubble

The snapshots from the simulations are presented in Figure 3.4. Up to the moment of the first bubble collapse, the results appear visually identical, with no notable difference. At approximately $t \approx 12 \mu\text{s}$, the bubble undergoes a collapse, and a liquid jet penetrates both bubbles. In the case of coarse resolution, the liquid jet cannot be resolved adequately and fails to penetrate the bubble. For medium and fine resolutions, similar bubble shapes are observed after the jetting. However, the fine resolution offers more intricate details, such as some gas being carried by the jet, and the formation of a bubble tail.

Figure 3.5 presents the surface modes, equivalent bubble radius, and bubble mass. The top bubble is represented by a continuous line, while the bottom bubble is represented by a dashed line, with different colors denoting different resolutions, as indicated in the legend. The first mode corresponds to the translational motion of the bubble, the top bubble initially moves slightly upwards as shown by the continuous curves in Subfigure (a). Negative a_1 values indicate an upward motion based on the polar coordinate transformation defined earlier in Figure 1.2d. During the collapse, the top bubble starts moving downward towards the other bubble, and this motion remains consistent across different resolutions. In contrast, the bottom bubble – as indicated by the dashed curves in Subfigure (a) – moves downward and then upward. Here, the coarse resolution (red line) deviates more, but overall, a clear trend of convergence is observed. For modes 2 to 4 (Subfigure (b) to (d)), increasing the resolution leads to convergence. In each case, there is a significant difference between the coarse and medium results compared to the medium and fine results. This behavior strongly indicates the convergence of the surface modes. For higher surface modes, the coarse resolution performs much worse, as in these cases, the mode amplitudes are comparable to the cell size, with $a_{\min}^{(\text{coarse})} = 0.91 \mu\text{m}$.

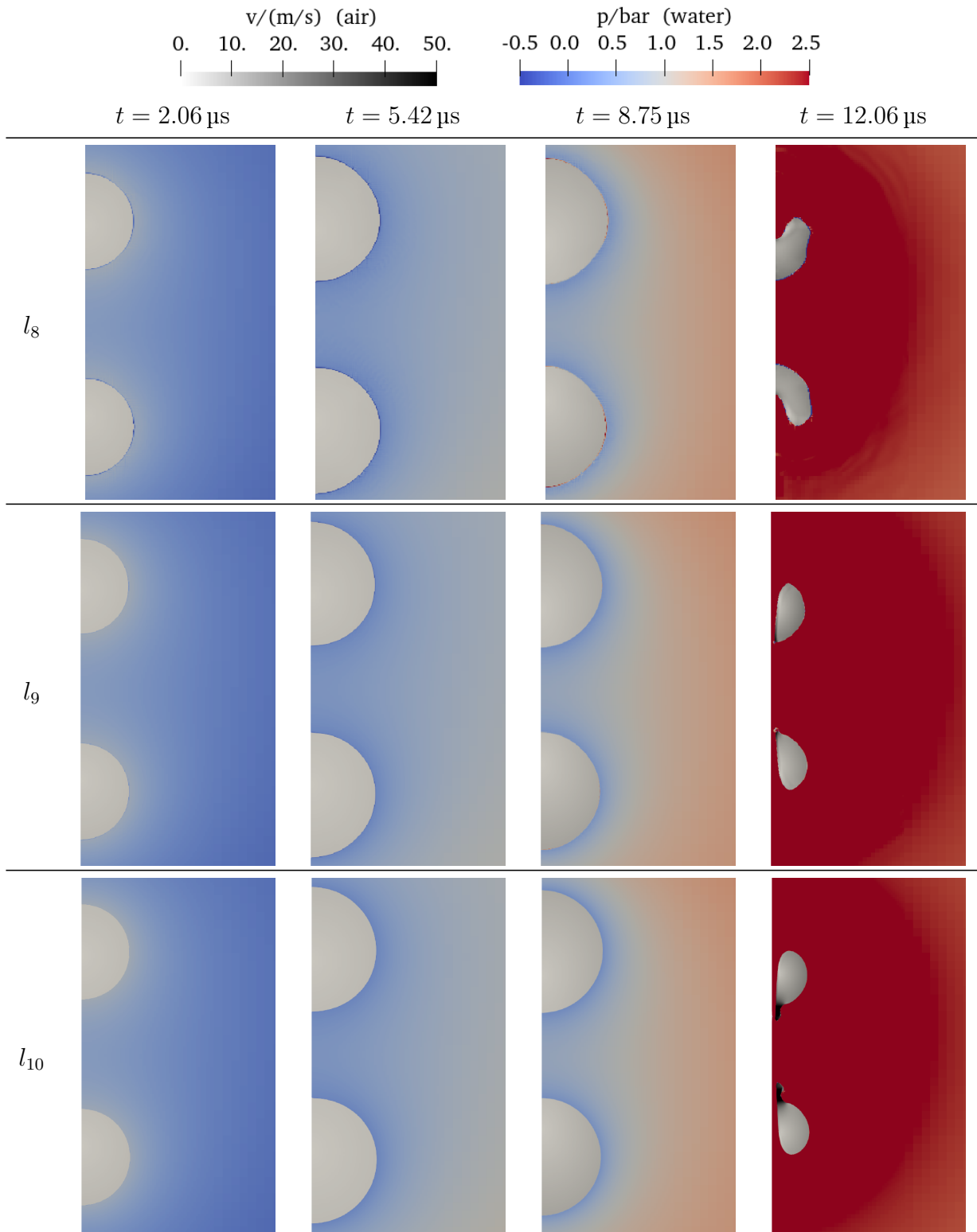


Figure 3.4: Simulation results at different resolutions

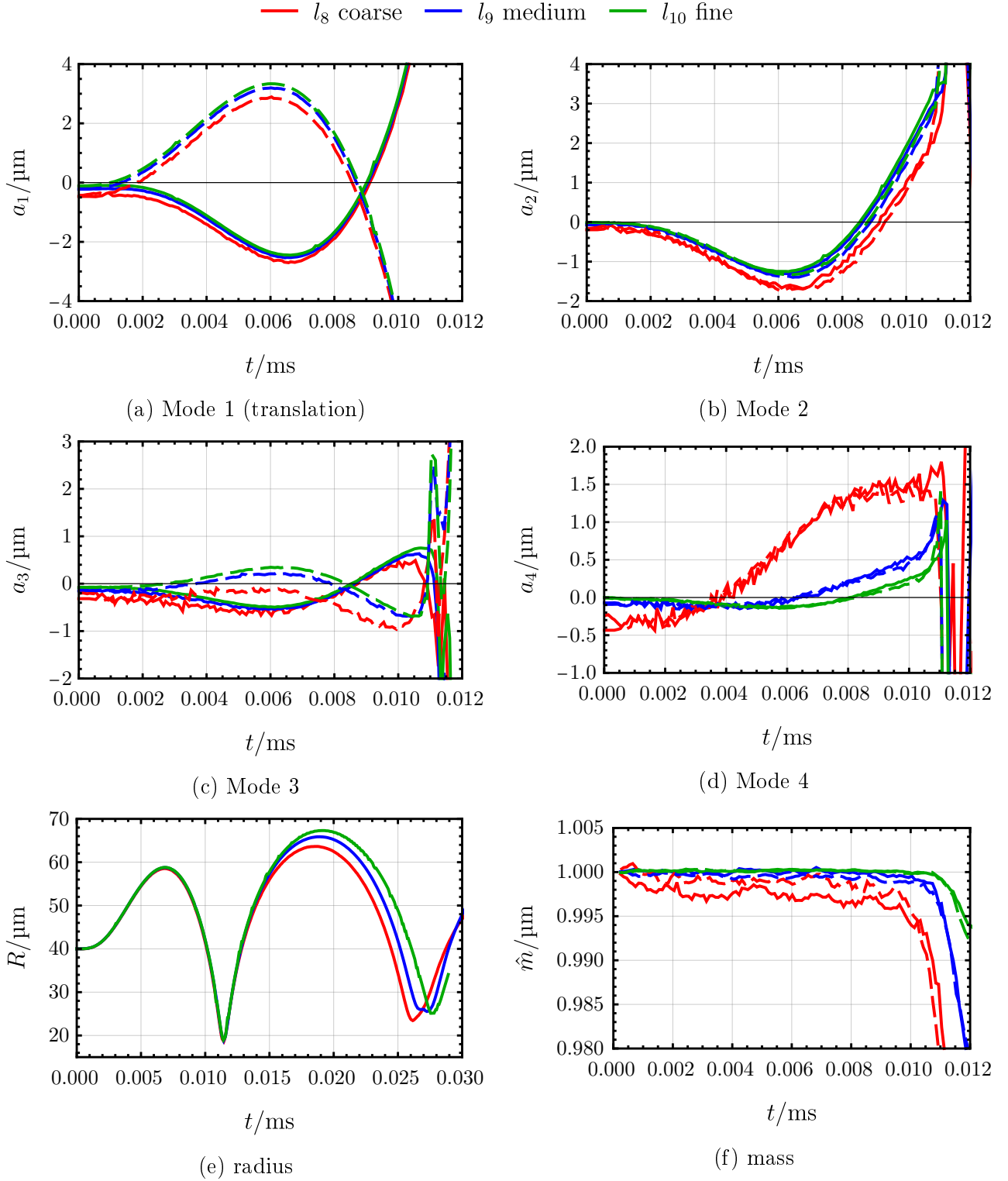


Figure 3.5: Surface mode amplitudes, bubble radius and mass of the top and bottom bubble using different resolutions (continuous line: top bubble, dashed line: bottom bubble).

The equivalent bubble radius remains consistent across all resolutions until the bubble collapse occurs around $t \approx 0.012$ ms. Subfigure (e) reveals that during the second cycle, the results start to deviate. Subfigure (f) illustrates that the bubble mass remains nearly constant until the moment of collapse, indicating dissipation levels of less than 0.5%. However, during

the collapse phase between $t \approx 0.010$ ms and $t \approx 0.012$ ms, the bubble mass decreases. Notably, higher resolutions exhibit a slower decrease in mass. It's important to clarify that this mass dissipation is not a physical phenomenon but rather an artifact caused by the insufficient resolution of the bubble's surface. Based on the convergence study, the following observations can be made:

- The coarse resolution is sufficient if the primary goal is to calculate integral quantities like the bubble radius. However, this resolution does not capture the surface details accurately, resulting in differences in surface modes, and it fails to simulate the formation of a bubble jet.
- The medium resolution, on the other hand, provides reasonably similar mode amplitudes to the fine resolution until bubble collapse. It also successfully captures the formation of a bubble jet at the same time instance. In the long term, some deviation occurs due to mass loss and lower surface resolution.

In the following simulations, a medium resolution is considered adequate since the long-term behavior is not the primary focus. The main objective is to determine the bubbles' effect on each other for a relevant sonochemistry case. As previously mentioned, achieving the peak chemical output requires only a few expansion-collapse cycles. While toroidal bubbles forming following a jet align with theoretical and experimental findings, it's important to note that these cases inherently involve three-dimensional phenomena, like the circulation ring around the bubble [39], which cannot be captured by the axisymmetric assumption. Consequently, the fine details of bubble jet formation are not of primary interest, and medium resolution suffices to determine whether jetting occurs. Medium resolution simulations also run quickly, meaning the simulation of a single acoustic cycle take approximately 2 hours on 4 CPU cores.

3.3 Effect of distance

The distance between the bubbles for a bubble radius of $R_0 = 40$ μm was varied from $D^* = 2$ to 80 (for the definition of D^* refer to Equation (3.1)). In the simulations, a traveling wave passed through the bubbles, after which the simulation continued for at least one more expansion-collapse cycle. The following quantities were monitored:

- The maximum pressure inside the bubble at the first bubble collapse, denoted as $p_{B,\text{max}}$. This represents the average bubble pressure in the collapsed state. Generally, the pressure distribution inside the bubble remains fairly homogeneous, even for highly deformed bubbles, and the maximum deviation stays below 1%.
- The rate of bubble collapse, defined as the size difference between the maximally expanded and collapsed state during the first cycle,

$$\Delta R_{\text{max}} = R_{\text{expanded}} - R_{\text{collapsed}}, \quad (3.10)$$

where R refers to the equivalent bubble radius. The equivalent bubble radius is derived from the bubble volume, as mentioned before.

- Time of jetting: When bubbles are in proximity they collapse in an aspherical way, similar to a bubble near a wall, and a bubble jet forms along the symmetry axis. The jet cuts through the bubble, leaving behind a toroidal shape. The time when the jet reaches the other side, and a toroidal shape is formed, is denoted as t_{jet} .

- The non-sphericity until the start of collapse is assessed using the \hat{a}_{avg} metric. This dimensionless measure has a local maxima in the expanded state. It's worth noting that \hat{a}_{dev} can also be employed to quantify non-sphericity, and the results are consistent in both cases. The \hat{a}_{avg} metric is selected for its simplicity.

Radius-time curves for various D^* values are presented for the bottom bubble in Figure 3.6a. The Keller-Miksis solution for a single bubble is also indicated by a dashed black line. In each case, the bubble reaches its maximum size around $t \approx 0.007$ ms and collapses around $t \approx 0.0011$ ms. It is evident that when the bubbles are in close proximity (D^* is small), the collapse is delayed. The farther apart the bubbles are, the better the Keller-Miksis equation approximates the radius-time curve. When the bubbles are infinitely far away, representing a single bubble, the Keller-Miksis equation aligns with the ALPACA simulation until the first collapse.

In Figure 3.6b, the non-sphericity \hat{a}_{avg} is illustrated. The non-sphericity exhibits a local maximum in the expanded state at around $t \approx 0.007$ ms, and during the collapse, non-sphericity spikes. For $D^* < 6$, a bubble jet occurs at the time of the collapse. The local maxima in non-sphericity are also more pronounced when the bubbles are closer together. Even in the case of a single bubble ($D^* = \infty$), there is a spike in the non-sphericity with $\hat{a}_{\text{avg}} > 0.2$, because the traveling wave results in slightly asymmetric pressures between the top and bottom of the bubble. Based on the validation in Section 2.1.3, it is expected that for such significant spikes, the Keller-Miksis equation loses validity. Consequently, the radius already deviates in the next expansion cycle.

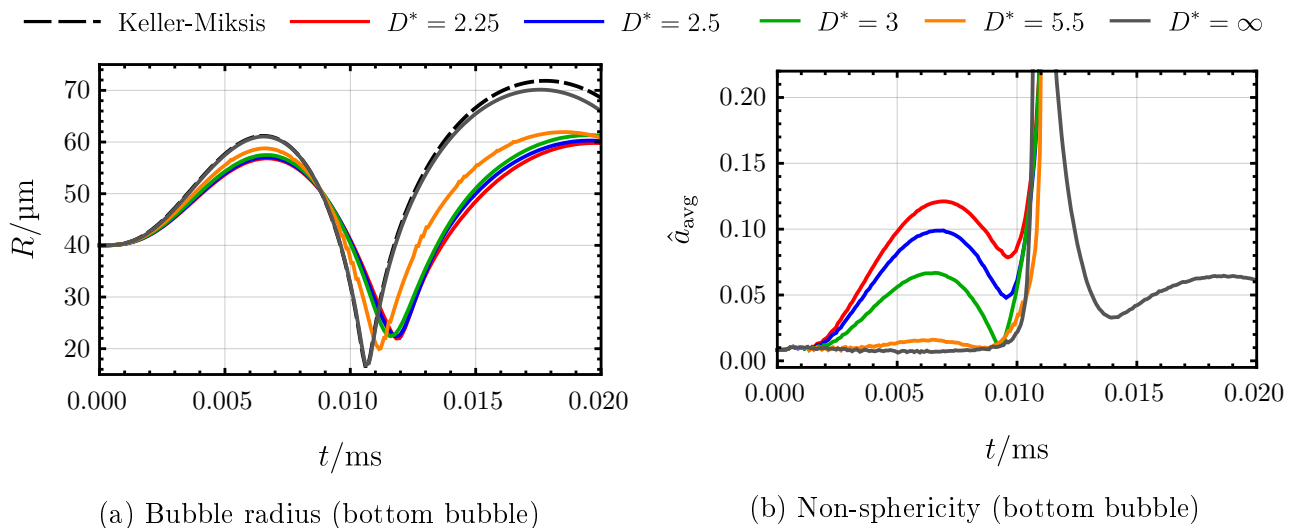
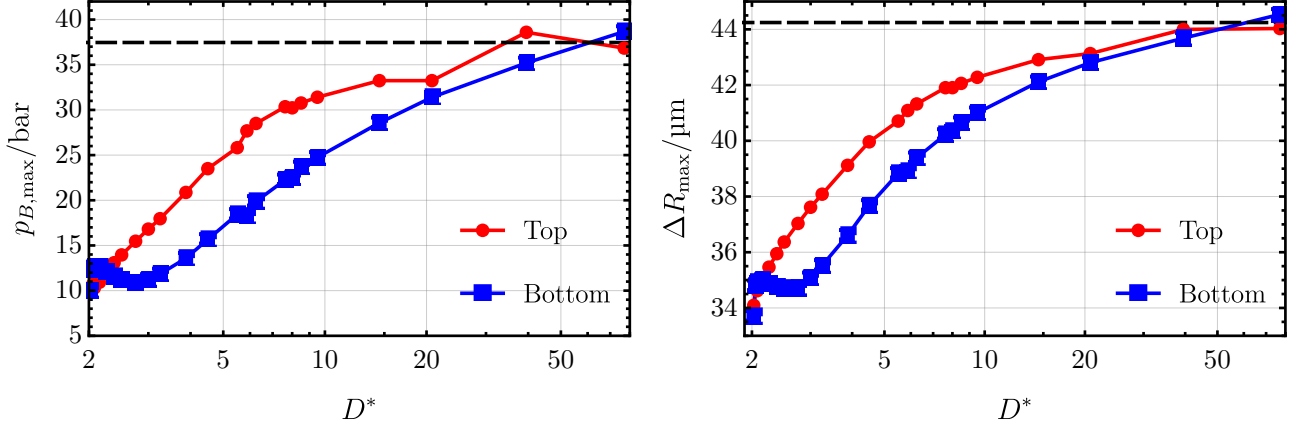


Figure 3.6: Radius and non-sphericity of the bottom bubble in the first 2 acoustic cycles for selected D^* values, colored according to the legend.

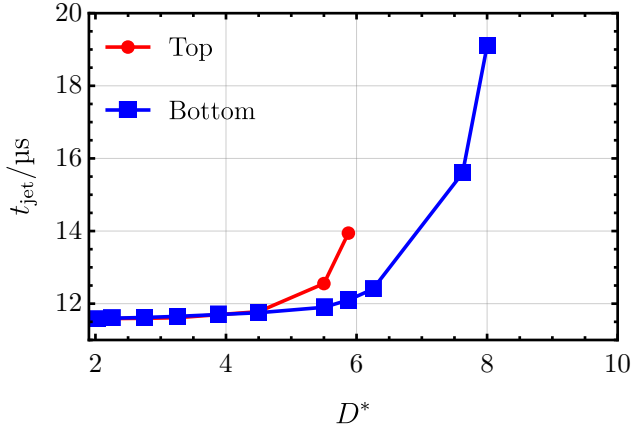
A large-scale study was conducted involving 24 ALPACA simulations, the parameters and observations are summarized in Table 5.3 in the Appendix. The results are summarized in Figure 3.7. Subfigure (a) illustrates the maximum bubble pressure in both bubbles as a function of the dimensionless distance D^* . The dashed black line represents the maximum pressure for the $D^* = \infty$ case, where the pressure inside the bubble reached $p_B = 37.5$ bar. Subfigure (b) shows the maximum collapse, ΔR_{max} . It is noticeable that the bottom bubble experiences less compression compared to the top one. For closely spaced bubbles ($D^* \leq 4$), the bubble pressure does not even reach half of the single-bubble case, indicating that the bubbles have a strong

negative influence on each other. This negative effect persists until $D^* = 40$. However, for $D^* \geq 20$, the pressure decrease is less than 15%.

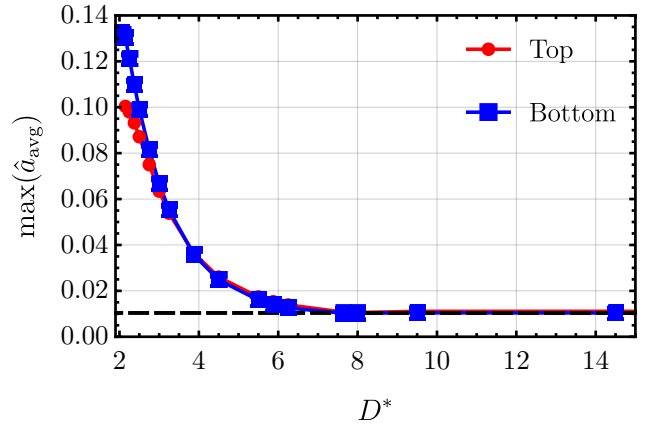


(a) Maximum bubble pressure as a function of D^* in the top and bottom bubble

(b) Maximum bubble collapse ($R_{\max} - R_{\min}$) as a function of D^*



(c) Bubble jetting time as a function of D^*



(d) Non-sphericity as a function of D^*

Figure 3.7: Effect of dimensionless distance D^* between bubbles on the bubble pressure, maximum collapse, jetting time and non-sphericity. The values for both the top and bottom bubble are presented according to the legend.

For closely spaced bubbles, the loss of compression can be attributed to bubble jetting. As shown in Subfigure (c), a bubble jet cuts through the top bubble until $D^* = 6$ and the bottom one until $D^* = 8$. The jet of the top bubble is consistently slightly delayed because the acoustic wave reaches it later. This time difference is already accounted for in the figure by subtracting $\Delta t_{\text{jet}} = D/c$ from the measured jetting time, ensuring a perfect overlap in the jetting time of the top and bottom bubbles until $D^* = 4$. For $D^* = 4 \dots 6$, the top bubble jets exponentially later as the distance increases, because the bubble jet's velocity gets lower as the bubble expansion is more spherical. In the range $D^* = 6 \dots 8$, the bottom bubble also jets later while the top bubble does not jet anymore. At $D^* = 8$, the non-sphericity of the bubble is already minimal, as depicted in Subfigure (d). The maximal non-sphericity during the first cycle decreases as the bubbles move farther apart, as observed already in Figure 3.6b. Altogether, six different phenomena can be classified as shown in Figure 3.8:

1. **Coalescence** $D^* \leq 2.025$: During the expansion phase the bubbles merge together, and then during collapse a bubble jet forms.

2. **Symmetric jets** $2 < D^* < 4$: Following a highly non-spherical expansion, the top and bottom bubbles jet at the same time, with the time delay accounted for by the propagation of sound.
3. **Delayed top jet** $4 < D^* < 6$: The non-sphericity of the expansion is small, and the top bubble jets exponentially later. However, this delay is not caused by the speed of sound.
4. **Only bottom jet** $6 < D^* < 8$: The top bubble does not jet in the first cycle anymore, but the bottom one still does.
5. **No jet, but large effect** $8 < D^* < 20$: The bubbles have a significant effect on each other, and the compression is still not optimal. However, bubble jetting and a significant loss of sphericity do not occur anymore. The loss of compression is mainly the result of the damping of the acoustic wave.
6. **Diminishing effect** $20 < D^*$: The bubbles' effect on each other is small, and the bubble pressure is near the single-bubble case. At $D^* \approx 40$, the bottom bubble even has a seemingly positive effect on the top one, as the top bubble experiences a larger compression than the single-bubble case, similar situation can be observed around $D^* \approx 80$ (see Figure 3.7a). It should be noted, that the temporal resolution is not high enough to capture the maximum pressure exactly as it persists only for a fraction of a microsecond during an extreme collapse.

These phenomena will be investigated in detail in the following section.

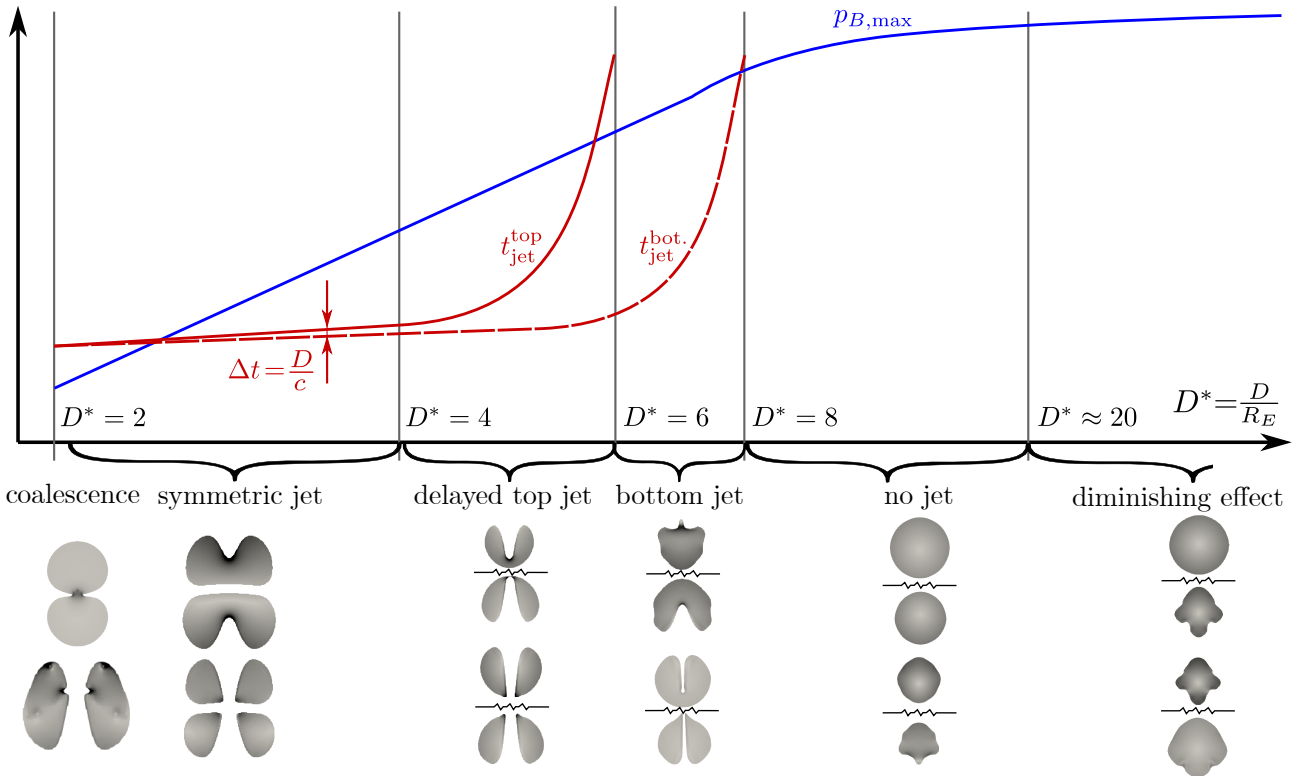


Figure 3.8: Qualitative effect of bubbles on each other as function of the bubble distance D^* . The snapshots below the graph depict the before and after collapse states of the bubbles.

3.4 Interaction phenomena

3.4.1 Coalescence in the expansion phase

Coalescence in the expansion phase occurs when the bubble interfaces are in close proximity. Merger during the first acoustic cycle was observed only at $D^* = 2.025$, meaning that the initial distance between the bubble interfaces was $d = 1 \mu\text{m}$. According to the theory, as adjacent bubbles expand, a pressure film forms between them. Further expansion causes the drainage of this film until a critical film thickness of around $0.1 \mu\text{m}$ is reached, leading to the coalescence of the bubbles due to attractive Van der Waals forces [27].

The process of bubble coalescence is illustrated in Figure 3.9. The expansion is highly non-spherical, and a liquid film remains between the bubbles, as observed at $t = 5.0 \mu\text{s}$. As the bubble continues to expand, this liquid film drains, causing a significant drop in pressure ($p \ll p_B \ll p_0$). By $t = 7.5 \mu\text{s}$, the bubbles have already coalesced. It is important to note that the critical film thickness is smaller than the minimum cell size, and Van der Waals forces are not simulated. However, coalescence still occurs. In the simulation, the pressure before merger drops to almost 0 bar in the liquid, compared to the bubble pressure of 0.3 bar. This low pressure essentially pulls the bubble interfaces together and leads to their merger.

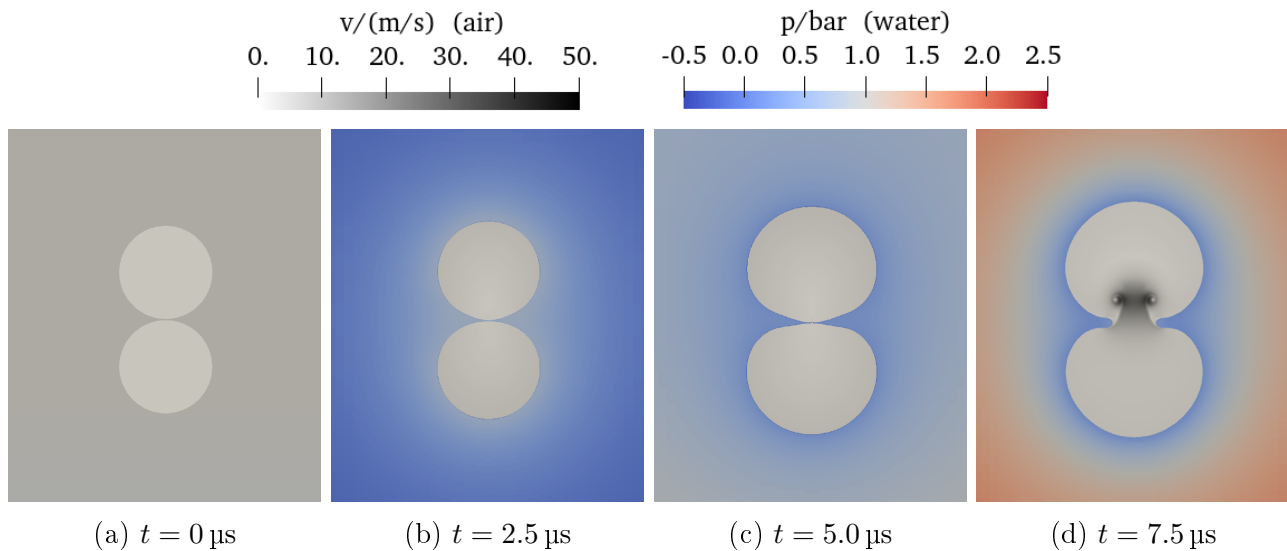


Figure 3.9: Bubble coalescence in the $D^* = 2.025$ case

3.4.2 Non-spherical expansion

If the initial distance between the bubble interfaces is greater than $d = 1 \mu\text{m}$, the bubbles do not coalesce during the first expansion. However, the bubbles remain highly non-spherical, and the surfaces facing each other become flattened. This flattening is a well-known phenomenon that is observed when bubbles collide and can also be extended to expanding bubbles [27]. According to theory, flattening occurs when the liquid inertia is greater than the capillary pressure caused by surface tension. Flattening takes place when the Weber number exceeds a threshold of 0.5. The Weber number for expanding bubbles is [27]

$$\text{We} = \frac{\rho v^2}{\frac{\sigma}{R_m}}, \quad (3.11)$$

where ρ is the density of liquid, σ is the surface tension and R_m is the mean radius defined as

$$\frac{2}{R_m} = \frac{1}{R_1} + \frac{1}{R_2}. \quad (3.12)$$

The velocity, denoted as v , is determined by the sum of the bubble expansion velocities, which can be expressed as $v = \dot{R}_1 + \dot{R}_2$. As shown in Figure 3.10, the bubbles, which start with the same initial radius, have approximately the same radius at later times. Therefore, the mean radius can be considered as $R_m = R$. Assuming a constant expansion from the initial radius of $R = 40 \mu\text{m}$ to the maximum size of $R = 57 \mu\text{m}$ at $t = 7 \mu\text{s}$, the velocity can be approximated as follows,

$$\dot{R} = \frac{57 \mu\text{m} - 40 \mu\text{m}}{7 \mu\text{s}} \approx 2.5 \text{ m/s}, \quad (3.13)$$

meaning $v \approx 5 \text{ m/s}$. This results in a Weber number ranging from 13 to 20 throughout the expansion, indicating that the bubble interfaces should flatten out. This flattening phenomenon can be observed in the ALPACA simulation, as illustrated in Figure 3.10. The Weber number criteria for expanding bubbles does not include the distance between the bubbles in any way. However, based on the ALPACA simulations, it is known that flattening persists until $D^* \approx 4$, although with diminishing effects.

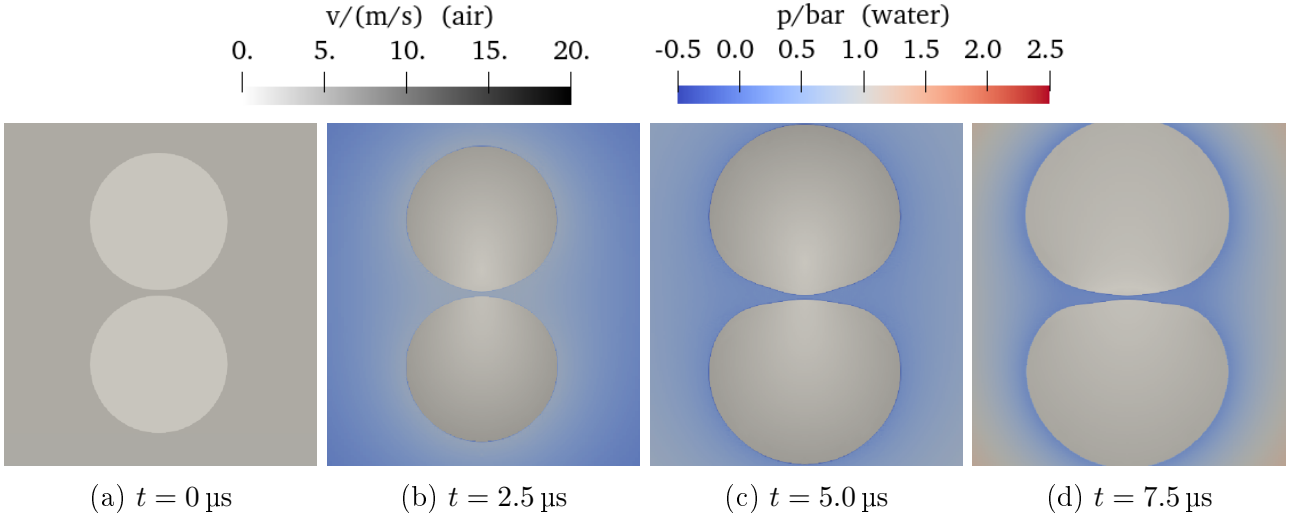


Figure 3.10: Flattening in the $D^* = 2.075$ case

3.4.3 Symmetric jets

As already known, proximate bubbles expand non-spherically due to flattening. According to theory, a non-spherical bubble during collapse produces a high-velocity jet if a pressure gradient is present during the collapse [25]. Figure 3.11 illustrates the rapid collapse and the bubble jet for the $D^* = 2.25$ simulation. Due to the flattening in the expanded state, non-sphericity is already present. The pressure gradient is the result of film drainage between the bubbles and pressure inhomogeneities caused by surface tension due to the non-spherical shape. At the start of jetting at $t = 11.2 \mu\text{s}$, the pressure gradient between the north and south sides of the bubbles reaches almost 3 bar. The velocity of the liquid jet reaches around 120 m/s according to the simulation. The jets then collide in the middle, causing a radial (x -directional) flow directed outwards that widens the conical hole in the toroidal bubbles, as seen at $t = 11.8 \mu\text{s}$.

The jets are roughly symmetric, meaning that they have similar velocities and cut through the bubble at the same time instance, except for the $\Delta t_{\text{jet}} = D/c$ time delay caused by the propagation of sound. For instance in the $D^* = 3.875$ case, the jetting times are as follows,

$$t_{\text{jet}}^{\text{bot.}} = 11.7 \mu\text{s} \quad \text{and} \quad t_{\text{jet}}^{\text{top}} = 11.8 \mu\text{s}. \quad (3.14)$$

The time delay in this case is

$$\Delta t_{\text{jet}} = \frac{D}{c} = \frac{155 \mu\text{m}}{1496 \text{ m/s}} \approx 0.1 \mu\text{s}, \quad (3.15)$$

meaning that the delayed jetting comes from the fact that information reaches the top bubble with the speed of sound. The jets are symmetric until $D^* \approx 4$, which coincides with the limit for flattening as well.

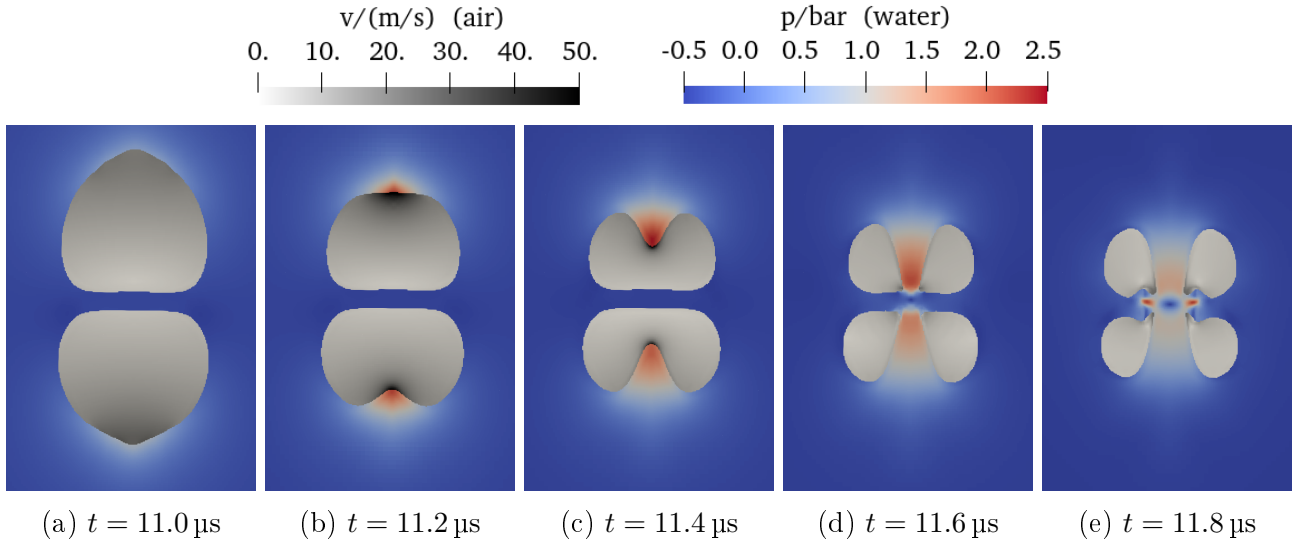


Figure 3.11: Symmetric jets penetrating the bubble along the axis in the $D^* = 2.25$ simulation

3.4.4 Delayed jets

As D^* is increased from 4 to 6, the initiation of jetting in the top bubble occurs later. This delay is a consequence of reduced pressure gradients and, consequently, diminished jet velocities. The simulation for $D^* = 5.5$ is depicted in Figure 3.12. It can be observed that at the onset of jetting at $t = 11.0 \mu\text{s}$, the bubbles exhibit less distortion compared to previous instances (refer to Figure 3.11 for comparison). Additionally, flattening no longer occurs, leading to lower pressure gradients. The pressure gradient across the bubbles is not visible in the figure, as the pressure surrounding the bubbles exceeds 12 bar due to the intense collapse. The pressure gradient across the bubble can be measured using Paraview, and at the start of the jetting,

$$\Delta p_{\text{bot.}} = 1.41 \text{ bar} \quad \text{and} \quad \Delta p_{\text{top}} = 1.16 \text{ bar}, \quad (3.16)$$

indicating that the top bubble experiences a smaller gradient, resulting in a slower jet. The jet's velocity is not sufficient to completely penetrate the top bubble in its collapsed state, and the bubble begins to expand during the jetting phase, as evidenced at $t = 12 \mu\text{s}$. Despite the jet's deceleration due to the expanding bubble, it ultimately manages to cut the bubble by $t = 13 \mu\text{s}$. The precise jetting times and the time delay caused by the speed of sound are as follows,

$$t_{\text{jet}}^{\text{bot.}} = 11.9 \mu\text{s}, \quad t_{\text{jet}}^{\text{top}} = 12.7 \mu\text{s} \quad \text{and} \quad \Delta t_{\text{jet}} = \frac{D}{c} \approx 0.15 \mu\text{s}, \quad (3.17)$$

implying that the delay in jetting cannot be attributed to the limited speed of sound. These scenarios are categorized as asymmetric jets because the jetting velocities differ between the top and bottom bubbles, and the shape of the bubbles during jetting also differs. As the distance increases, non-sphericity diminishes in the expanded state (refer to Figure 3.7d from earlier), resulting in progressively smaller pressure gradients and jetting velocities. Consequently, more time is required for the jet to penetrate the bubble. As the jet proceeds more slowly in the top bubble, significant shape deformations appear at a later stage, allowing for a greater degree of compression. At $t = 11.5 \mu\text{s}$, the top bubble exhibits a smaller volume, and consequently, a smaller equivalent radius. The equivalent radii in the collapsed state are as follows,

$$R_{\text{bot.}}(11.5 \mu\text{s}) = 22.1 \mu\text{m} \quad \text{and} \quad R_{\text{top.}}(11.5 \mu\text{s}) = 18.4 \mu\text{m}, \quad (3.18)$$

indicating a more substantial compression of the top bubble. With this, it becomes clear why the top bubble attains a higher maximum pressure upon collapse as observed previously in Figure 3.7a. Simply put, the smaller initial pressure gradient across the bubble results in a more spherical collapse.

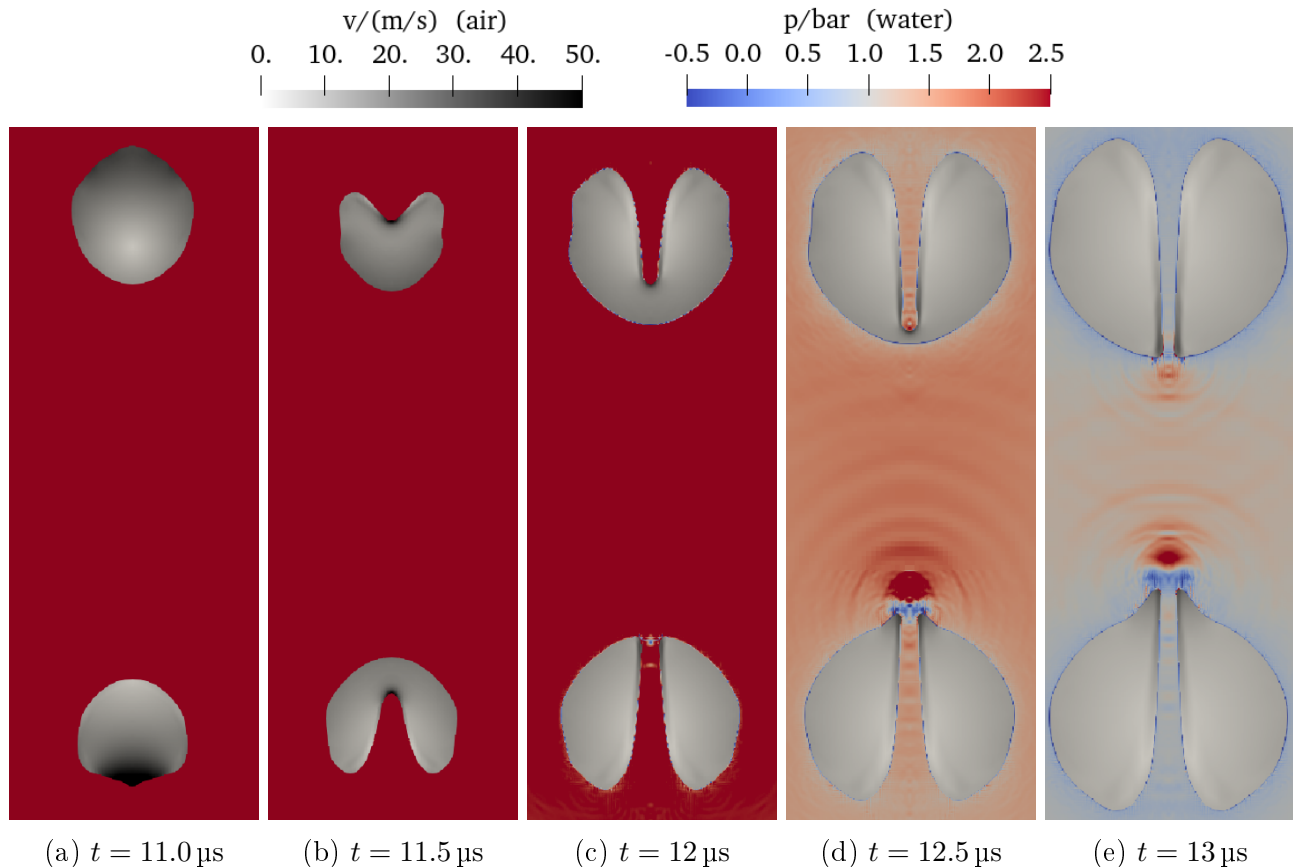


Figure 3.12: Asymmetric jets penetrating the bubble along the axis in the $D^* = 5.5$ simulation

3.4.5 Halting jets

As the separation distance between bubbles increases, the jet velocity decreases. Additionally, jets gradually lose speed as they traverse through the bubble and may even come to a halt at certain points. Figure 3.13 illustrates the top bubble in the simulation with $D^* = 6.25$. At $t = 12 \mu\text{s}$, the jet's velocity only reaches 25 m/s, significantly lower than the 120 m/s jetting velocity observed for symmetric jets at $D^* = 2.25$. As the bubble expands, the jet decelerates even

further, and by $t = 15 \mu\text{s}$, the jet has already stopped, creating an opening in the bubble from the top. The critical distance at which the top bubble is not penetrated by the jet completely is approximately $D_{\text{crit}}^* \approx 6$, while the critical distance for the bottom bubble is approximately $D_{\text{crit}}^* \approx 8$. Beyond $D^* > 8$, the bubbles still significantly affect each other in an adverse manner, although jets do not occur anymore.

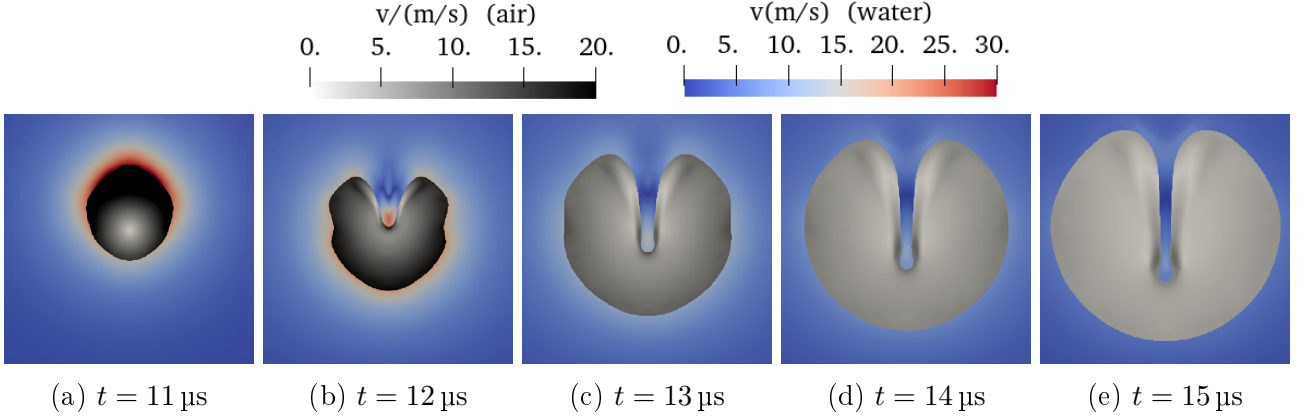


Figure 3.13: Bubble jet halting during the expansion in the $D^* = 6.25$ simulation

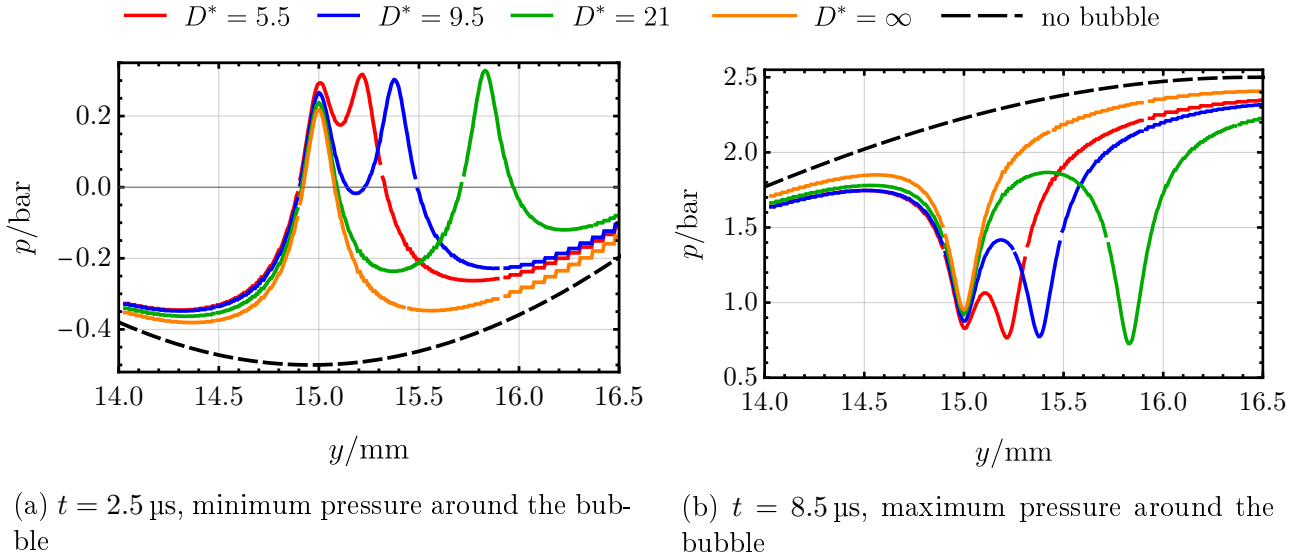


Figure 3.14: The effect of bubbles on the surrounding pressure. The bottom bubble is placed at $y_0 = 15 \text{ mm}$ while the top bubble is at $y_0 + D^* \cdot R_0$. The different colors represent different D^* values according to the legend.

3.4.6 Effects through the pressure field

For larger distances, specifically $D^* > 8$, jetting and non-sphericity caused by flattening does not occur. Nevertheless, the bubbles still influence each other from a distance through the damping of the acoustic field. In the simulations, the bottom bubble is positioned at $y_0 = 15 \text{ mm}$, and the minimum pressure of the traveling wave reaches the bottom bubble at $t = 2.5 \mu\text{s}$. The pressure along the y axis is presented in Figure 3.14a. If no bubble is present in the domain, the pressure at $y_0 = 15 \text{ mm}$ should be $p_0 - p_A = -0.5 \text{ bar}$, as indicated by the dashed black

line. When a single-bubble is introduced into the domain, i.e., $D^* = \infty$, the pressure around the bubble is higher, approximately around 0.2 bar, as depicted by the orange curve. The closer another bubble is placed in the domain, the higher the pressure becomes around the bubble; for $D^* = 5.5$, it is nearly 0.3 bar (see the red curve). Elevated pressures during the expansion phase are disadvantageous because they lead to reduced expansion.

Similarly, the pressure around the bubble is depicted after the peak of the wave has reached the bubble at $t = 8.5 \mu\text{s}$. In this case, the pressure around the bubble decreases as the bubbles are closer. For instance, the pressure experienced by the bottom bubble at $D^* = 5.5$ is approximately 0.1 bar lower than in the $D^* = \infty$ scenario. Lower pressures around the bubble in this phase are also undesirable because they result in a smaller collapse. Close bubbles effectively experience a reduced pressure amplitude throughout the expansion-collapse cycle, but this effect diminishes with increasing distance.

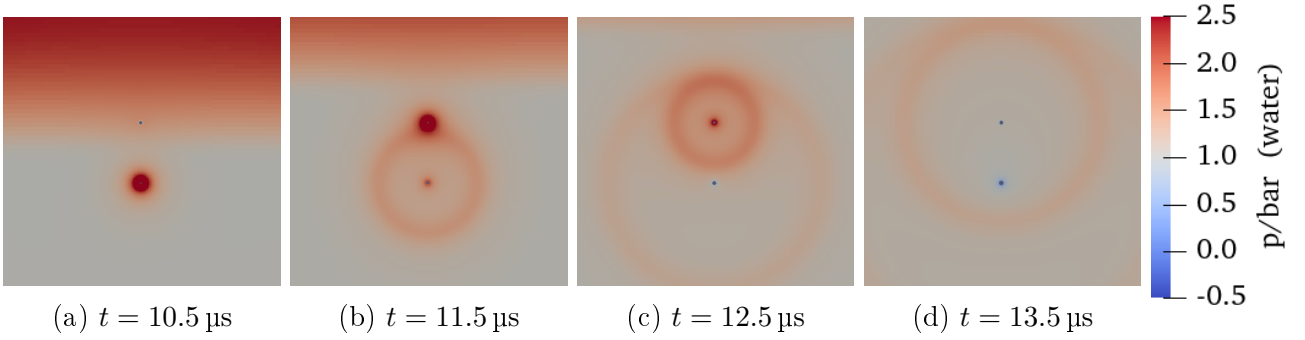
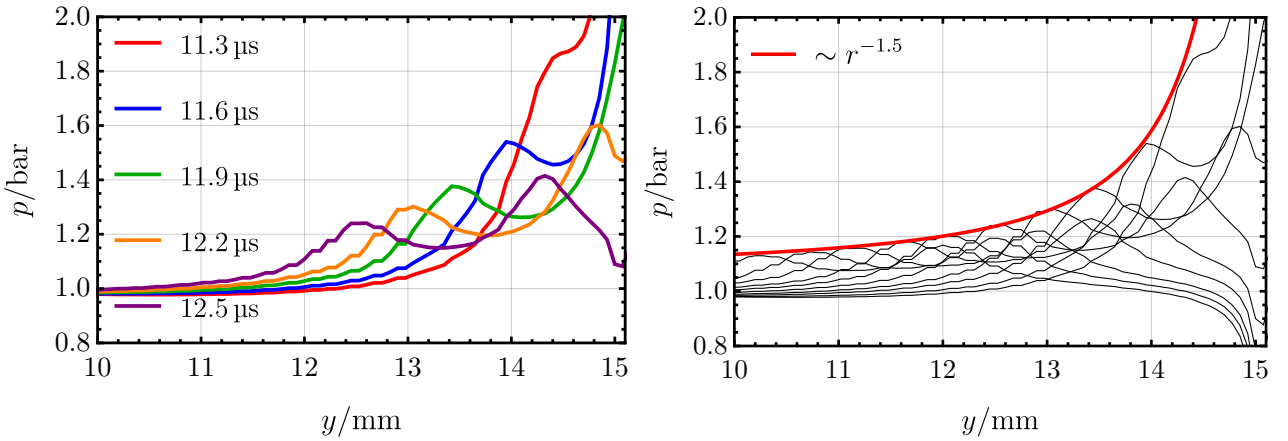


Figure 3.15: Shockwave from the bubble collapse in the $D^* = 39.5$ simulation



(a) Pressure profile along the y axis at specified time instances. Time instances and coloring are according to the legend.

(b) Decay of the shockwave. The thin black lines depict the pressure in several time instances and red is the enveloping curve.

Figure 3.16: Propagation and decay of the shockwave

3.4.7 Pressure wave emission

It is a well-established fact that cavitating bubbles emit shockwaves [40]. In Figure 3.15 the $D^* = 39.5$ simulation results are depicted, showing the emission of a shockwave from the bottom bubble at approximately $t = 10.5 \mu\text{s}$. This shockwave then propagates radially outward and interacts with the top bubble during its collapse. However, its impact is relatively limited, given

that the amplitude of the shock is around 1 bar, while the pressure of the bubble reaches 37 bar. Figure 3.16a displays pressure data along the y -axis, illustrating the shockwave's progression in the negative y direction, along with its gradual decay. According to theoretical expectations, the pressure front should decay with a rate of $r^{-1.5}$, where r represents the distance from the bubble. In Figure 3.16b, pressure values are plotted at 10 different time instances, and they conform to an enveloping curve resembling $1.06 \text{ bar} + 0.80 \cdot r^{-1.5}$.

The top bubble emits a pressure wave around $t = 11.5 \mu\text{s}$, and similarly, it decays with a rate of $r^{-1.5}$. This decay is also evident in Figure 3.15. In this particular case, the shockwave's effect on the bubble is relatively minor due to the small amplitudes, but more substantial collapses can generate even larger shockwaves.

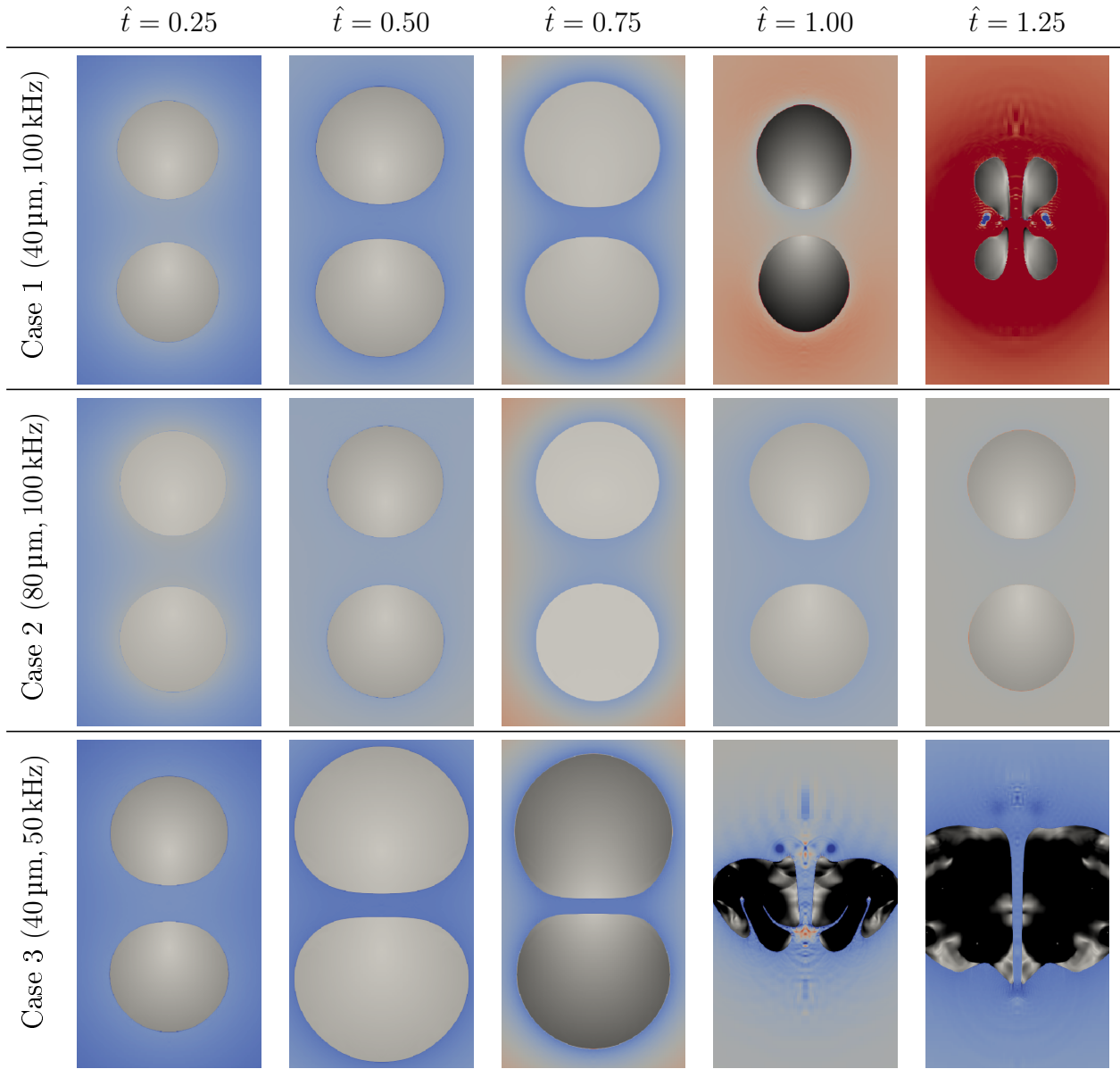


Figure 3.17: $D^* = 3$ simulation snapshots with various parameters in given time instances.

3.5 Influence of parameters

It was found $D^* \approx 20$ is the threshold beyond which the influence of bubbles on each other becomes negligible. However, adjusting other parameters may alter this threshold. With the

current setup using two bubbles of the same size, there are three parameters to control:

1. Bubble size R_0 : In smaller bubbles, the effect of surface tension is more pronounced.
2. Frequency f : Lowering the frequency results in longer acoustic cycles, allowing more time for the expansion of the bubble and a more vigorous collapse.
3. Pressure amplitude p_A : Higher pressure amplitudes also lead to more powerful collapses.

The impact of distance is explored with larger bubbles and lower frequencies. In the first case, the original configuration investigated thus far, with $R_0 = 40 \mu\text{m}$ and $f = 100 \text{ kHz}$ is considered and used as a reference. In the second case, the bubble size was increased to $R_0 = 80 \mu\text{m}$, while keeping all other parameters the same. In the third case, the frequency was reduced to $f = 50 \text{ kHz}$. To compare the cases a dimensionless time is introduced as

$$\hat{t} = t \cdot f. \quad (3.19)$$

According to the initial conditions, the minimum pressure point of the traveling acoustic wave reaches the bottom bubble at $\hat{t} = 0.25$, the maximum pressure point at $\hat{t} = 0.75$ and the excitation ends at $\hat{t} = 1$. In Figure 3.17, the qualitative effects of the parameters for a distance of $D^* = 3$ can be observed. In the second case, where the bubble size was increased, jetting does not occur during the collapse. Furthermore, the larger bubble compresses much less compared to the smaller bubble, and the pressure in the larger bubble only reaches 2.8 bar during the collapse, in contrast to the 16 bar pressure reached in the smaller bubble. In the third case, the lower frequency results in a more substantial bubble collapse with jetting, where the pressure reaches 12 bar. Notably, the bubbles even coalesce during jetting. Based on the figure, it is evident that changing parameters such as the radii and frequency has a significant impact on the behavior of the bubbles. The same jetting limits cannot be identified for modified parameters because the behavior is inherently different. In the second case, not even adjacent bubbles exhibit jetting, whereas in the third case, jetting occurs even when a single bubble is placed in the domain.

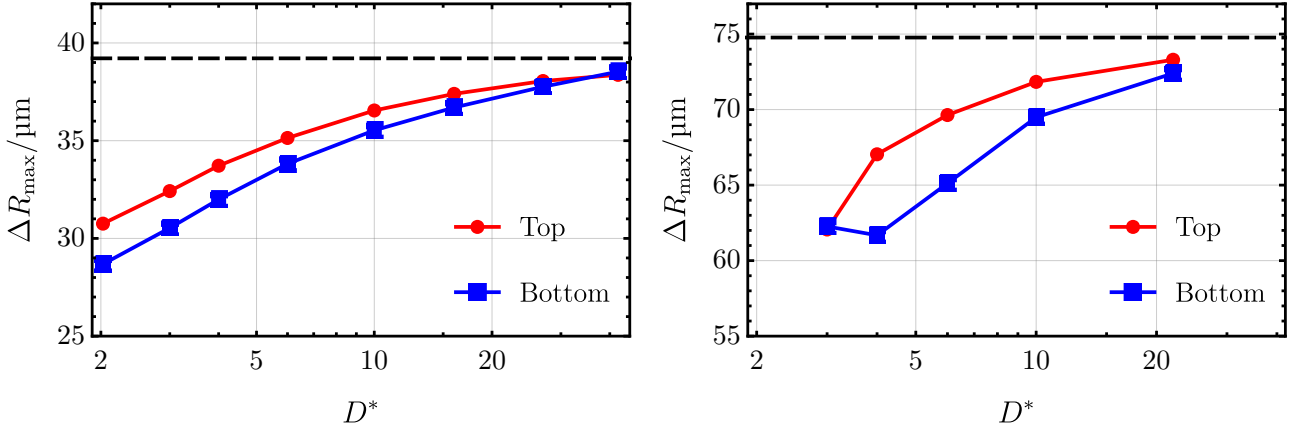
The maximum difference in radius throughout the first cycle (i.e. maximum collapse), denoted as ΔR_{max} and defined in Equation (3.10), is employed to compare each case. This value represents the variation in the equivalent radius at maximum expansion and at collapse. The equivalent radius is determined based on volume, thus ΔR_{max} effectively characterizes the volume change. Alternatively, the maximum pressure change could be used as a metric. However, during the collapsed state, pressure changes extremely rapidly. For instance, consider the following parameters:

$$f = 50 \text{ kHz}, \quad R_0 = 40 \mu\text{m} \quad \text{and} \quad D^* = 34.$$

These parameters result in a pressure change inside the bubble of 183 bar during a time step of $\Delta t = 0.125 \mu\text{s}$ at the end of the collapse. The pressure change in the subsequent time step is already -148 bar . The temporal gradient is so high that a much higher sampling rate is required to accurately capture the maximum pressure. However, the ALPACA simulation saves data only at each macro time step. The multiresolution algorithm in ALPACA employs different time steps on each resolution level. This means a minimum micro time step size of $0.125 \mu\text{s}/2^{l_{\text{max}}}$. Given that, in the collapsed state, the entire bubble is resolved using the highest level, which is $l_{\text{max}} = 10$, the step size within the bubble is actually 0.122 ns. Consequently, the simulation results are expected to remain accurate, and too large step sizes do not pose a significant issue. However, it's important to note that, without modifying the source code of ALPACA, it is not feasible to write out the micro time steps. Currently, higher sampling rates are only achievable by reducing the Courant number, which leads to much slower simulations. Therefore, the use

of the equivalent radius as a metric is preferred, as its gradient is considerably smaller, and sampling introduces a smaller error.

The maximum collapse, denoted as ΔR_{\max} , is presented in Figure 3.18a as a function of the dimensionless distance D^* in the second case. The maximum collapse of a single bubble with the same parameters is represented by a horizontal dashed line. As the distance between the bubbles increases, the effect becomes smaller, and the results approach those of the maximum collapse in the single-bubble case. Similar to initial case (as shown in Figure 3.7b), the top bubble experiences a significant collapse, and this difference diminishes at around $D^* \approx 30$. Figure 3.18b depicts the maximum collapse in third case. The maximal collapse similarly approaches the single-bubble case as the distance is increased.



(a) Case 2: Maximum collapse in case of $R_0 = 80 \mu\text{m}$, $f = 100 \text{ kHz}$

(b) Case 3: Maximum collapse in case of $R_0 = 40 \mu\text{m}$, $f = 50 \text{ kHz}$

Figure 3.18: Maximum collapse in second and third case. The dashed black line denotes the maximum collapse of a single-bubble ($D^* = \infty$) with the same parameters.

The trends of maximal collapse as a function of D^* are notably similar in each case. To facilitate comparisons among the cases, the dimensionless deviation from the single-bubble case is introduced, denoted as \hat{R}_{dev} , which is:

$$\hat{R}_{\text{dev}} = \frac{\Delta R_{\infty} - \Delta R_{\max}}{\Delta R_{\infty}}, \quad (3.20)$$

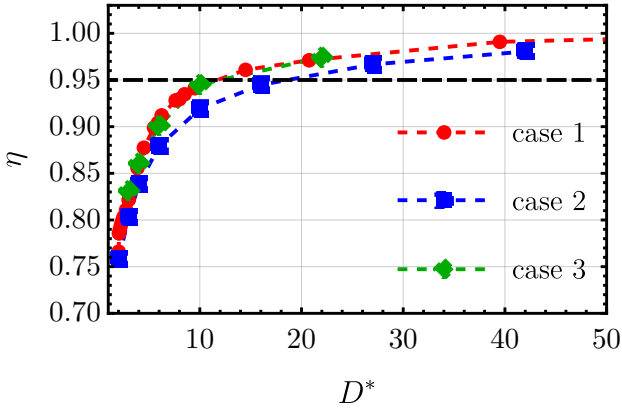
where ΔR_{∞} is the maximum collapse of a single bubble using the same parameters. This deviation can be computed for both the top and the bottom bubble ($\hat{R}_{\text{dev}}^{(\text{top})}$ and $\hat{R}_{\text{dev}}^{(\text{bot.})}$). Utilizing this deviation from the optimal single-bubble case, we can define the collapse efficiency as:

$$\eta = 1 - \frac{\hat{R}_{\text{dev}}^{(\text{top})} + \hat{R}_{\text{dev}}^{(\text{bot.})}}{2}. \quad (3.21)$$

This efficiency metric offers a measure of how effectively the bubbles collapse, taking into account both the top and bottom bubbles in the comparison.

The compression efficiency is depicted as a function of distance in Figure 3.19. Interestingly, the efficiency's dependence on D^* is quite consistent for bubbles of the same size. This can be attributed to the fact that D^* accurately captures the mutual influence of the bubbles but does not consider the variation in the effect of surface tension, which also changes with size. In each case, the efficiency experiences a rapid increase when $D^* < 10$. In this region, the

effect of bubbles on each other is notably significant. As $10 < D^* < 20$, there is a transitional phase where the collapse efficiency surpasses 95%. Beyond $D^* > 20$, the effect diminishes and gradually approaches the behavior observed in the single-bubble case ($\eta = 1$).



Case	Radius $R_0/\mu\text{m}$	Frequency f/kHz
1	40	100
2	80	100
3	40	50

Figure 3.19: The effect of the bubbles on each other in different scenarios

3.6 Adding more bubbles

Some simulations were conducted based on the first case ($R_0 = 40 \mu\text{m}$, $f = 100 \text{ kHz}$), but with an additional bubble placed above the two previous bubbles at the same distance. In the first simulation, a value of $D^* = 2.25$ was selected. According to the findings from the two-bubble scenario, one would expect to observe the flattening and jetting of the bubbles. Figure 3.20 provides a visualization of the flattening and collapse of all three bubbles. The middle bubble undergoes flattening on both sides, as observed at $t = 11 \mu\text{s}$, and jetting initiates in the top and bottom bubbles at $t = 12 \mu\text{s}$. The middle bubble does not experience a significant pressure gradient since the conditions on its south and north sides are similar, which explains the absence of jets during its collapse. However, high-velocity jets, with speeds of approximately $v \approx 70 \text{ m/s}$, originated from the bottom and top bubble reach and penetrate the middle bubble. In the end, three toroidal bubbles are formed at $t = 14 \mu\text{s}$. At a distance of $D^* = 4.5$, a similar scenario unfolds, with the top and bottom bubble jetting during the collapse, and consequently effecting the middle bubble.

As the distance between the bubbles increases, the influence of the bubbles on each other diminishes. Figure 3.21a displays the maximum collapse of each bubble in the three-bubble simulation. With increasing distance, the maximum collapse also approaches the optimal collapse of a single-bubble. This three-bubble scenario is directly compared to the two-bubble case in Figure 3.21b, where the average efficiency η is presented as a function of the dimensionless distance D^* . In each case, the efficiency is slightly reduced in comparison to the two-bubble case. However, the overall trend remains similar, and the threshold of 95% efficiency is attained at around $D^* \approx 20$. This suggests that the threshold of $D^* \approx 20$ remains applicable even in scenarios involving more bubbles. However, it's worth noting that when dealing with a significantly larger number of bubbles, additional factors such as the damping of the acoustic wave may also become significant.

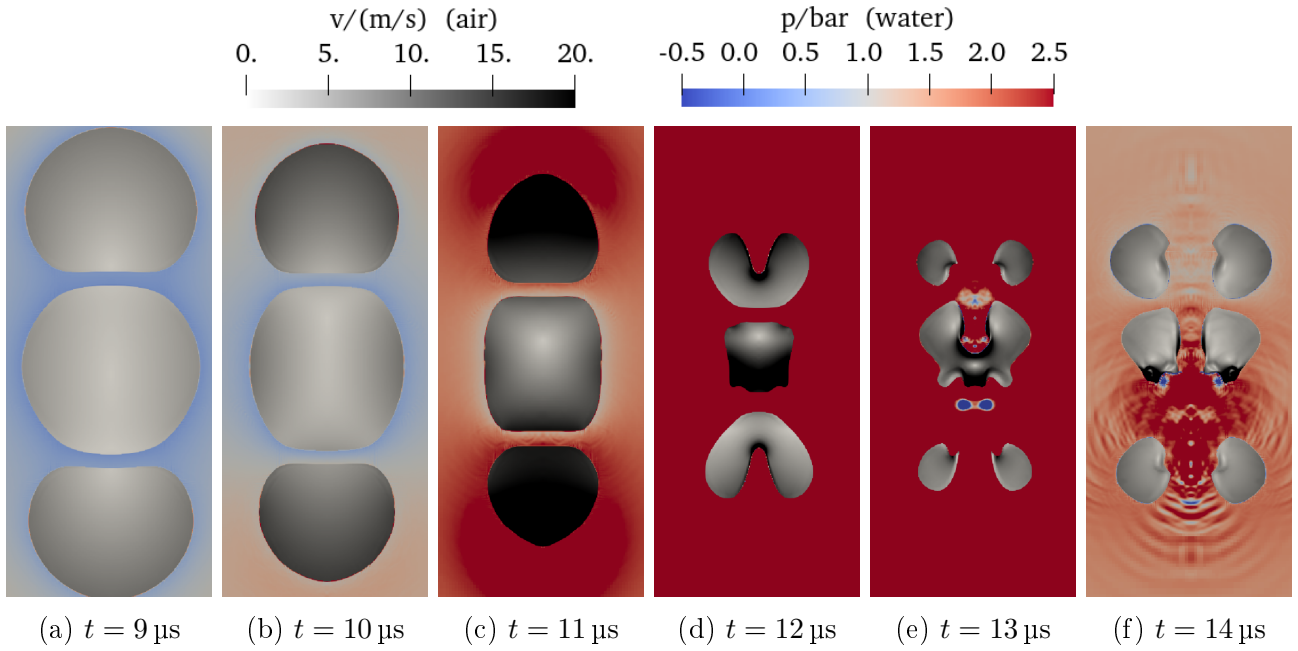
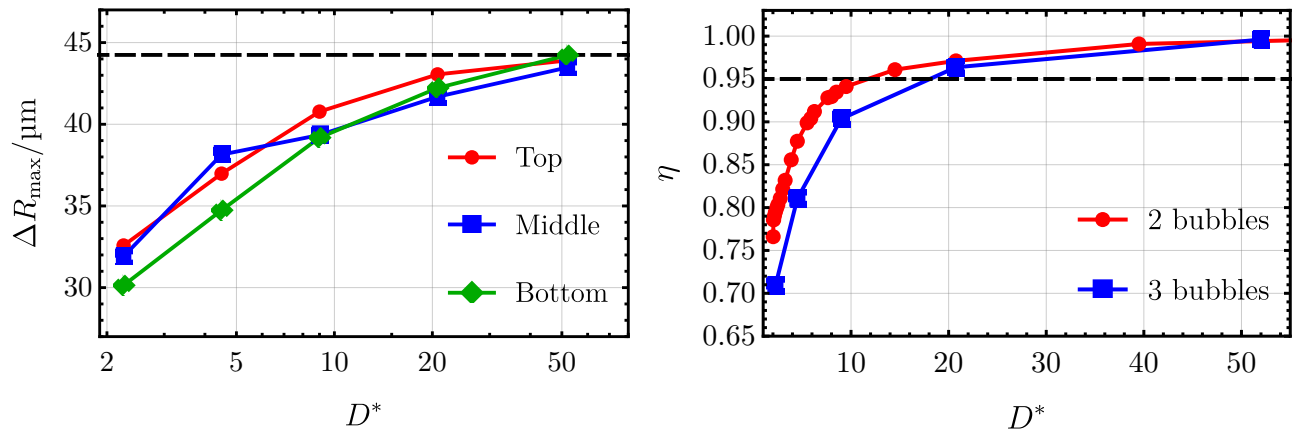


Figure 3.20: Flattening and jetting in the $D^* = 2.25$ case with 3 bubbles.



(a) Maximum collapse (ΔR_{\max}) in the 3 bubble case. The different colors belong to the top, middle and bottom bubble according to the legend.

(b) Efficiency η of the 2 and 3 bubble case. The coloring corresponds to the legend. The dashed horizontal line marks the 95% efficiency.

Figure 3.21: Summary of results in the 3 bubble simulation as a function of the dimensionless bubble distance D^*

4 Conclusion

4.1 Validation

The first objective was to validate the ALPACA software for sonochemical simulations. Numerous simulations were conducted, encompassing both spherical and non-spherical scenarios, and they exhibited remarkable agreement with other models and experimental measurements. Some of these findings were previously reported, however this study presented several new discoveries, while established results were utilized, including the requirement for a bubble resolution exceeding $D_{\text{cell}} > 100$ and the necessity of a sufficiently large simulation domain, particularly for high-frequency cases to prevent acoustic wave dampening.

The primary new discovery was the validity limit of the Keller-Miksis equation for non-spherical bubble oscillations, based on the amplitudes of surface modes. The Keller-Miksis equation is formulated for spherical bubbles; however, it was observed that the radial dynamics of bubbles do not significantly deviate even when their spherical shape is lost. Two metrics were introduced to characterize the non-sphericity of the bubbles: one is the sum of the squares of dimensionless mode amplitudes, denoted as \hat{a}_{avg} , and the other measures the sectional area deviation from a spherical shape, denoted as \hat{a}_{dev} . Additionally, a metric E to quantify the error caused by non-sphericity was introduced. The crucial finding was that, **as long as a bubble's non-sphericity remains below a specific threshold in the collapsed state, the radial dynamics in the subsequent expansion-collapse cycle can be accurately described by the Keller-Miksis equation.** If the non-sphericity exceeds the threshold, accuracy is not guaranteed, and the error can surpass 10% during the following cycle. The specific threshold values are defined as:

$$\hat{a}_{\text{avg}} = 0.2 \quad \text{and} \quad \hat{a}_{\text{dev}} = 0.1. \quad (4.1)$$

This validity limit was found to hold even in the case of multi-bubble simulations, as illustrated in Figure 3.6b.

4.2 Reduced Order Model (ROM)

An extensive comparison was conducted between the reduced order model and ALPACA. The ROM simulations were executed by Peter Kalmar, while the classification of dominant modes was performed by myself. Furthermore, the 62 conducted ALPACA simulations and the subsequent comparison are my individual work. Previously, both ALPACA and the ROM were validated using only a limited number of measurements, as not many are available in the literature. This is due to the challenging nature of obtaining precise measurements of surface modes. The comparison between ALPACA and ROM reveals that, in most cases, both models can accurately predict surface oscillations and bubble breakup, resulting in an impressive 87% agreement. To achieve these results in ALPACA, a bubble resolution of $D_{\text{cell}} \approx 300$ was applied in each case. Instances where the models exhibited deviations were primarily associated with

- the amplitude of surface mode oscillations falling within the sub-grid resolution of ALPACA, or
- the dimensionless amplitudes exceeding the validity limit of the ROM ($\hat{a}_i > 0.2$).

The most important conclusion drawn from this study is that **both ALPACA and ROM are effective tools for simulating surface mode oscillations. Additionally, both models accurately predict the spherical stability limit.** However, it is essential to note that bubble

breakup in ROM does not always translate to breakup in ALPACA. For bubble breakup to occur, it necessitates large mode amplitudes that exceed the validity limit of ROM. Even in cases where this limit is exceeded, ROM continues to accurately predict bubble breakup in most scenarios. Based on these findings, we can confidently employ both ROM and ALPACA for the investigation of non-spherical bubbles, taking into consideration their respective validity limits.

4.3 Multi-bubble systems

This study showcased a setup involving multi-bubble systems that were acoustically excited with a traveling wave. The bubbles were placed along the symmetry axis. To ensure the accuracy of results, a convergence study was conducted using three numerical meshing settings to determine the necessary resolution. The study revealed that, even with a coarse mesh, integral quantities could be accurately described during the initial expansion-collapse cycle. However, to accurately capture surface modes, a resolution of approximately $D_{\text{cell}} \approx 175$ was employed. This resolution level made possible the simulation of bubble jets while maintaining a reasonable runtime, allowing for the execution of a substantial number of simulations.

A comprehensive study was conducted, consisting of an initial set of 24 simulations to investigate the impact of the distance between bubbles in an acoustic field. Subsequently, an additional set of 22 simulations was introduced, incorporating various parameters to explore the dependency of the initial findings on these parameters. The parameters of the simulations are summarized in Table 5.3 in the Appendix. In this study, several interactions between bubbles in an acoustic field were identified using ALPACA:

- **Coalescence during expansion:** This phenomenon occurs when the bubble interfaces are in close proximity. During the expansion of neighboring bubbles, a liquid film forms between them. As expansion continues, the pressure in the film drops, leading to a merger of the interfaces. This was observed in the initial simulation and was found to hold for other parameters, but only in situations where the bubbles were extremely close, with $D^* \leq 2.025$.
- **Non-spherical expansion:** Non-spherical expansion is triggered by the flattening of the facing surfaces of bubbles. It is explained by a high Weber number during expansion, signifying that liquid inertia between the bubbles surpasses the surface tension's capillary pressure, causing the surfaces to flatten. A visible flattening effect persists until $D^* \approx 4$ in the initial simulation, and this limit was found to be applicable to other parameter combinations as well.
- **Symmetric jets at collapse:** Non-spherical shapes before collapse lead to substantial pressure gradients, resulting in the formation of bubble jets. These jets penetrate the bubble along the symmetry axis, resulting in the creation of toroidal bubbles. They are called "symmetric" because both the top and bottom bubbles exhibit a similar shape, and the jet velocities are identical. Symmetric jetting in the first case occurred until $D^* \approx 4$, but this threshold may not be directly applied to other parameter combinations. Nevertheless, similar symmetric jetting is observed for three bubbles with the same threshold of $D^* \approx 4$, where the middle bubble does not produce a jet, but two jets impact its surface.
- **Delayed jets:** In the initial set of simulations, as the bubbles experience reduced pressure gradients, the jet velocities are smaller, resulting in the delayed penetration of the bubble. This delay initially occurs at the top bubble for $D^* > 4$ and similarly at the bottom bubble for $D^* > 6$. At some point, the velocities become so small that the jet halts inside the

bubble. This behavior is specific for the initial set of parameters (see the first case in Section 3.5).

- **Effects through the pressure field:** Bubbles significantly influence the pressure of the surrounding acoustic wave. Nearby bubbles have a mutual impact on each other, leading to elevated surrounding pressure during the expansion phase and reduced pressure during the collapse phase. As a result, bubbles effectively experience a reduced pressure amplitude.
- **Pressure wave emission:** Cavitating bubbles emit a shockwave, and the amplitude of this shockwave decreases with the distance (-1.5 power). Although the pressure wave can affect other bubbles, the specific setup used in this study did not produce amplitudes significant enough to result in a considerable effect on other bubbles.

While certain phenomena, like jetting, are indeed specific to particular parameters, it was discovered that the interactions between bubbles can be effectively characterized by D^* . The qualitative graph of the maximal collapse is found to be largely independent of various parameters. **The efficiency of collapse provides a parameter-independent description of the effect of bubble distance.** This metric is based on the difference between the maximal expanded bubble radius and the collapsed bubble radius, compared to the single-bubble case. Based on the value of D^* scenarios can be categorized into three groups

1. $D^* < 10$: In this range, the bubbles exert a significant influence on each other through non-spherical expansion and highly damped pressure amplitudes. The efficiency of collapse remains below 95% in each case.
2. $10 < D^* < 20$: This represents a transitional phase with a notably larger collapse of the top bubble in each case. Direct effects like non-spherical expansion are less prominent, but the damping of pressure amplitudes is still significant.
3. $D^* > 20$: Here, the mutual effect diminishes and eventually becomes negligible. The efficiency of collapse reaches 95% in each case and slowly converges to 100%.

In conclusion, it can be deduced that the efficiency loss attributed to other bubbles does not exceed 5% as long as $D^* = D/R_0 > 20$, where D represents the distance between the center of the bubbles, and R_0 is the initial equilibrium bubble radius. This threshold is independent of various parameters, such as frequency and bubble size, and it is also found to be unrelated to the number of bubbles involved, as long as the number of bubbles is small.

4.4 Improvement points

There are several potential areas for improving the current work. Most notably, the establishment of the $D^* = 20$ threshold was based on only three sets of parameters. To ensure a reliable threshold, further testing with a variety of parameter sets and arrangements is essential. However, this endeavor demands increased computational resources. For instance, under the current settings, with $f = 100$ kHz and $R_0 = 40$ μm , a full length simulation would require approximately 4 hours to run on a typical data center CPU. For each set of parameters, roughly 10 simulations should be conducted. The challenge lies in the fact that halving the frequency (f) doubles the simulation time, and similarly, halving the bubble size (R_0) also doubles the simulation time. For instance, running a simulation at $f = 20$ kHz and $R_0 = 20$ μm would take approximately 40 hours. The plan moving forward is to draft a new proposal for supercomputing resources based on the results of this study. This will provide access to the additional computational resources needed for the expanded and comprehensive parameter exploration.

There are additional points that require attention. As previously mentioned, significant collapses can result in rapid pressure changes within the bubbles. However, the current version of ALPACA lacks the capability to employ a sufficiently high sampling rate to resolve these collapses in time, without the need for reducing the Courant number. Given that ALPACA is an open-source software, the code can be modified to record the bubble pressure during micro time steps. By implementing source code modifications, it is also possible to address mass dissipation through the artificial increase in bubble mass at each step. This adjustment would enable the execution of long-term simulations, extending beyond the limitations of just 10 acoustic cycles. A similar solution has already been successfully employed by researchers in OpenFOAM [17].

Acknowledgment

Thanks to *Dr. Ferenc Hegedűs* for his ideas, suggestions and theoretical help. I also thank *Péter Kalmar* for the explanation of the Reduced Order Model and the data provided. Thanks to the *Nanoshock* research group for providing pre-release access to the new version of ALPACA. The author gratefully acknowledge the Gauss Centre for Supercomputing e.V. (www.gauss-centre.eu) for funding this project by providing computing time on the GCS Supercomputer SuperMUC-NG at Leibniz Supercomputing Centre (www.lrz.de). Supported by the **ÚNKP-23-2-III-BME-50** New National Excellence Program of the Ministry for Culture and Innovation from the source of the National Research, Development and Innovation Fund.



KULTURÁLIS ÉS INNOVÁCIÓS MINISZTERIUM



NATIONAL RESEARCH, DEVELOPMENT
AND INNOVATION OFFICE

HUNGARY



References

- [1] Timothy J Mason. “Sonochemistry and the environment—Providing a “green” link between chemistry, physics and engineering”. In: *Ultrasonics sonochemistry* 14.4 (2007), pp. 476–483.
- [2] Sangyeon Cho and Seok Hyun Yun. “Structure and optical properties of perovskite-embedded dual-phase microcrystals synthesized by sonochemistry”. In: *Communications Chemistry* 3.1 (2020), pp. 1–7.
- [3] JL Silva Junior et al. “Copper molybdate synthesized by sonochemistry route at room temperature as an efficient solid catalyst for esterification of oleic acid”. In: *Ultrasonics sonochemistry* 73 (2021), p. 105541.
- [4] Amir Hassanjani-Roshan et al. “Synthesis of iron oxide nanoparticles via sonochemical method and their characterization”. In: *Particuology* 9.1 (2011), pp. 95–99.
- [5] Mohammed Ali Dheyab et al. “Mechanisms of effective gold shell on Fe₃O₄ core nanoparticles formation using sonochemistry method”. In: *Ultrasonics sonochemistry* 64 (2020), p. 104865.
- [6] Sonja Lauterborn and Wilhelm Urban. “Ultrasonic cleaning of submerged membranes for drinking water applications”. In: *Journal of the Acoustical Society of America* 123.5 (2008), pp. 3291–3291.
- [7] TJ Mason, AP Newman, and SS Phull. “Sonochemistry in water treatment”. In: *Division of Chemistry, Coventry University, Coventry CVI 5FB* (1994), pp. 3927–3933.
- [8] Werner Lauterborn and Thomas Kurz. “Physics of bubble oscillations”. In: *Reports on progress in physics* 73.10 (2010), p. 106501.
- [9] Ruo Feng et al. “Enhancement of ultrasonic cavitation yield by multi-frequency sonication”. In: *Ultrasonics sonochemistry* 9.5 (2002), pp. 231–236.
- [10] Ryuzi Kato et al. “Sonochemical production of a carbon nanotube”. In: *Ultrasonics Sonochemistry* 6.4 (1999), pp. 185–187.
- [11] Alfred Vogel, S Busch, and U Parlitz. “Shock wave emission and cavitation bubble generation by picosecond and nanosecond optical breakdown in water”. In: *The Journal of the Acoustical Society of America* 100.1 (1996), pp. 148–165.
- [12] Forrest R Gilmore. “The growth or collapse of a spherical bubble in a viscous compressible liquid”. In: (1952).
- [13] Joseph B Keller and Michael Miksis. “Bubble oscillations of large amplitude”. In: *The Journal of the Acoustical Society of America* 68.2 (1980), pp. 628–633.
- [14] Stephen J Shaw. “Translation and oscillation of a bubble under axisymmetric deformation”. In: *Physics of Fluids* 18.7 (2006), p. 072104.
- [15] Stephen J Shaw. “The stability of a bubble in a weakly viscous liquid subject to an acoustic traveling wave”. In: *Physics of Fluids* 21.2 (2009), p. 022104.
- [16] Péter Kalmár et al. “Memory-friendly fixed-point iteration method for nonlinear surface mode oscillations of acoustically driven bubbles: from the perspective of high-performance GPU programming”. In: *Ultrasonics Sonochemistry* 99 (2023), p. 106546.
- [17] Max Koch et al. “Numerical modeling of laser generated cavitation bubbles with the finite volume and volume of fluid method, using OpenFOAM”. In: *Computers & Fluids* 126 (2016), pp. 71–90.

- [18] Jinsen Hu et al. “Numerical and experimental investigations on the jet and shock wave dynamics during the cavitation bubble collapsing near spherical particles based on Open-FOAM”. In: *Ultrasonics Sonochemistry* 99 (2023), p. 106576.
- [19] Benedikt Biller et al. “Jetting mechanisms in bubble-pair interactions”. In: *Physics of Fluids* 34.7 (2022).
- [20] Takuya Yamamoto, Shin-ichi Hatanaka, and Sergey V. Komarov. “Fragmentation of cavitation bubble in ultrasound field under small pressure amplitude”. In: *Ultrasonics Sonochemistry* 58 (2019), p. 104684.
- [21] Nils Hoppe et al. “ALPACA - a level-set based sharp-interface multiresolution solver for conservation laws”. In: *Computer Physics Communications* 272 (2022), p. 108246.
- [22] Vinay R Gopala and Berend Gm Van Wachem. “Volume of fluid methods for immiscible-fluid and free-surface flows”. In: *Chemical Engineering Journal* 141.1-3 (2008), pp. 204–221.
- [23] Sarah Cleve et al. “Microstreaming induced by acoustically trapped, non-spherically oscillating microbubbles”. In: *Journal of Fluid Mechanics* 875 (2019), pp. 597–621.
- [24] Matthieu Guédra and Claude Inserra. “Bubble shape oscillations of finite amplitude”. In: *Journal of Fluid Mechanics* 857 (2018), pp. 681–703.
- [25] Juan Manuel Rosselló et al. “Acoustically induced bubble jets”. In: *Physics of Fluids* 30.12 (2018).
- [26] Alexander A Doinikov. “Translational motion of two interacting bubbles in a strong acoustic field”. In: *Physical review E* 64.2 (2001), p. 026301.
- [27] Michiel Postema et al. “Ultrasound-induced encapsulated microbubble phenomena”. In: *Ultrasound in medicine & biology* 30.6 (2004), pp. 827–840.
- [28] Yang Shen et al. “The role of the bubble–bubble interaction on radial pulsations of bubbles”. In: *Ultrasonics Sonochemistry* 73 (2021), p. 105535.
- [29] Lin Fu, Xiangyu Y Hu, and Nikolaus A Adams. “A family of high-order targeted ENO schemes for compressible-fluid simulations”. In: *Journal of Computational Physics* 305 (2016), pp. 333–359.
- [30] Nils Hoppe, Stefan Adami, and Nikolaus A. Adams. “A parallel modular computing environment for three-dimensional multiresolution simulations of compressible flows”. In: *Computer Methods in Applied Mechanics and Engineering* 391 (), p. 114486.
- [31] Robert R Nourgaliev and Theo G Theofanous. “High-fidelity interface tracking in compressible flows: unlimited anchored adaptive level set”. In: *Journal of Computational Physics* 224.2 (2007), pp. 836–866.
- [32] Dániel Nagy. “Az ALPACA szoftvercsomag validációja nem gömbszimmetrikus buborékok szimulációjára”. In: *BME-GPK TDK Konferencia* (2022).
- [33] Francis H Harlow and Anthony A Amsden. *Fluid Dynamics. A LASL Monograph*. Tech. rep. Los Alamos National Lab.(LANL), Los Alamos, NM (United States), 1971.
- [34] JWJ Kaiser, S Adami, and NA Adams. “Three-dimensional direct numerical simulation of shock-induced bubble collapse near gelatin”. In: *11th International Symposium on Turbulence and Shear Flow Phenomena, TSFP 2019*. 2019.
- [35] Dániel Nagy. “Akusztikusan gerjesztett buborékok többfázisú numerikus szimulációja korszerű véges térfogat módszerrel”. In: *BME-GPK TDK Konferencia* (2021).

- [36] Dániel Nagy and Ferenc Hegedűs. “Az ALPACA szoftver validációja akusztikusan gerjesztett gázbuborékok szimulációjára: Validation of ALPACA for the simulation of acoustically excited gas bubbles”. In: *Nemzetközi Gépészeti Konferencia–OGÉT* (2023), pp. 360–365.
- [37] Michel Versluis et al. “Microbubble shape oscillations excited through ultrasonic parametric driving”. In: *Physical review E* 82.2 (2010), p. 026321.
- [38] Csanád Kalmár, Kálmán Klapcsik, and Ferenc Hegedűs. “Relationship between the radial dynamics and the chemical production of a harmonically driven spherical bubble”. In: *Ultrasonics sonochemistry* 64 (2020), p. 104989.
- [39] YL Zhang et al. “3D jet impact and toroidal bubbles”. In: *Journal of Computational Physics* 166.2 (2001), pp. 336–360.
- [40] Emil-Alexandru Brujan, T Ikeda, and Yoichiro Matsumoto. “On the pressure of cavitation bubbles”. In: *Experimental Thermal and Fluid Science* 32.5 (2008), pp. 1188–1191.
- [41] Matthieu Guédra et al. “Experimental evidence of nonlinear mode coupling between spherical and nonspherical oscillations of microbubbles”. In: *Physical Review E* 94.5 (2016), p. 053115.

5 Appendix

5.1 Legendre polynomials and surface modes

The n th Legendre polynomial is $P_n(x)$, the first few are

$$P_0(x) = 1, \quad (5.1)$$

$$P_1(x) = x, \quad (5.2)$$

$$P_2(x) = \frac{1}{2}(3x^2 - 1), \quad (5.3)$$

and

The Legendre polynomials also form a basis on the $[-1, 1]$ interval, meaning they are orthogonal to each other. The orthogonality of integrable functions can be defined based on a generalized scalar product

$$\langle f, g \rangle = \int_{-1}^1 f(x)g(x)w(x)dx, \quad (5.4)$$

where $w(x)$ is a weighting function. For Legendre polynomials $w(x) = 1$ and

$$\langle P_n, P_m \rangle = \int_{-1}^1 P_n(x)P_m(x)dx = \begin{cases} \frac{2}{2n+1} & \text{if } n = m \\ 0 & \text{if } n \neq m \end{cases}, \quad (5.5)$$

thus, they form a basis. To describe the modes shapes let $x = \cos \theta$, then $dx = -\sin \theta d\theta$ and after substitution,

$$\langle P_n(\cos \theta), P_m(\cos \theta) \rangle = \int_0^\pi P_n(\cos \theta)P_m(\cos \theta) \sin(\theta)d\theta = \begin{cases} \frac{2}{2n+1} & \text{if } n = m \\ 0 & \text{if } n \neq m \end{cases} \quad (5.6)$$

Equation (5.6) shows that the mode shapes also form an orthogonal basis, using the weight $w(\theta) = \sin \theta$. The bubble surface $r(\theta)$ can be described as a generalized Fourier series in the

$P_n(\cos \theta)$ basis

$$r(\theta) = \sum_{n=0}^{\infty} a_n P_n(\cos \theta), \quad (5.7)$$

where $a_0 = R$. The a_n Fourier coefficients can be calculated as

$$a_n = \frac{\langle P_n(\cos \theta), r(\theta) \rangle}{\langle P_n(\cos \theta), P_n(\cos \theta) \rangle} = \frac{2n+1}{2} \int_0^\pi P_n(\cos \theta) \cdot r(\theta) \cdot \sin(\theta) d\theta, \quad (5.8)$$

which formula can be found in many papers about non-spherical bubbles [14, 23, 24, 41], however none of them considers the bubble shape expansion as a generalized Fourier-series. This consideration opens up a new way to classify the sphericity of the bubble using Parseval's theorem,

$$\sum_{n=0}^{\infty} \frac{2|a_n|^2}{2n+1} = \int_0^\pi r(\theta)^2 \sin(\theta) d\theta. \quad (5.9)$$

Let us calculate the square of the deviation from the spherical shape,

$$\int_0^\pi \left(R - r(\theta)\right)^2 \sin(\theta) d\theta = \int_0^\pi \left(R^2 + r(\theta)^2 - 2Rr(\theta)\right) \sin(\theta) d\theta. \quad (5.10)$$

From Equation (5.8) it can be seen that, by setting $n = 0$

$$2a_0 = 2R = \int_0^\pi r(\theta) \sin(\theta) d\theta, \quad (5.11)$$

then Equation (5.10) is

$$\int_0^\pi \left(R - r(\theta)\right)^2 \sin(\theta) d\theta = 2R^2 + \sum_{n=0}^{\infty} \frac{2|a_n|^2}{2n+1} - 4R^2 = -2R^2 + 2R^2 + \sum_{n=2}^{\infty} \frac{2|a_n|^2}{2n+1}. \quad (5.12)$$

Finally, we can see that

$$\sum_{n=2}^{\infty} \frac{2|a_n|^2}{2n+1} = \int_0^\pi \left(R - r(\theta)\right)^2 \sin(\theta) d\theta, \quad (5.13)$$

and this gives integral of the deviation squared from the spherical shape, which is a possibility to characterize the non-sphericity of the bubble. Using the dimensionless mode coefficients

$$\sum_{n=2}^{\infty} \frac{2|\hat{a}_n|^2}{2n+1} = \int_0^\pi \left(1 - \frac{r(\theta)}{R}\right)^2 \sin(\theta) d\theta. \quad (5.14)$$

5.2 Derivation of standing and traveling waves

In a standing wave the pressure is

$$p(t, y) = p_0 + p_A \sin(\omega t) \cos(ky) \quad (5.15)$$

and in a traveling wave

$$p(t, y) = p_0 + p_A \sin(ky - \omega t), \quad (5.16)$$

where p_A is the pressure amplitude, $\omega = 2\pi f$ is the angular frequency and $k = 2\pi/\lambda$ is the spatial frequency. To derive the density and velocity in acoustic waves from a prescribed pressure first

the compressible continuity and Navier-Stokes equations have to be simplified. The governing equations of compressible flow in 1D are,

$$\text{continuity: } \frac{\partial \rho}{\partial t} + \frac{\partial(\rho v)}{\partial y} = 0 \quad \text{and} \quad (5.17)$$

$$\text{Navier-Stokes: } \frac{\partial(\rho v)}{\partial t} + \frac{\partial(\rho v^2)}{\partial y} = -\frac{\partial p}{\partial y} + \nu \frac{\partial^2 v}{\partial y^2}, \quad (5.18)$$

where v is the velocity in y direction, ρ is the density, p is the pressure and ν is the kinematic viscosity. In the equations v, p, ρ are all scalar fields depending on t and y . In the derivation the following assumptions are used:

1. The viscosity can be neglected.
2. The velocity v is much smaller than the speed of sound c , i.e. $v \ll c$.
3. The change of density is small, thus $\rho \approx \rho_0$ and even the change of density can be neglected when compared to the change of velocity.

Let us start the derivation by using the product rule in Equation (5.17),

$$\frac{\partial \rho}{\partial t} + v \frac{\partial \rho}{\partial y} + \rho \frac{\partial v}{\partial y} = 0, \quad (5.19)$$

and notice that from the 3rd assumption

$$v \frac{\partial \rho}{\partial y} \ll \rho \frac{\partial v}{\partial y}. \quad (5.20)$$

Then we get the following connection between the density and the velocity,

$$\frac{\partial \rho}{\partial t} + \rho_0 \frac{\partial v}{\partial y} = 0. \quad (5.21)$$

In the Navier-Stokes equation the viscosity is neglected, and the product rule is used on the left-hand side,

$$v \frac{\partial \rho}{\partial t} + \rho \frac{\partial v}{\partial t} + 2\rho v \frac{\partial v}{\partial y} + v^2 \frac{\partial \rho}{\partial y} = -\frac{\partial p}{\partial y}, \quad (5.22)$$

again the derivative of ρ can be neglected as they are compared to the much large derivatives of v . Then using $\rho \approx \rho_0$,

$$\rho_0 \frac{\partial v}{\partial t} + 2\rho_0 v \frac{\partial v}{\partial y} = -\frac{\partial p}{\partial y}. \quad (5.23)$$

Let us compare the magnitude of terms on the left-hand side, it can be assumed that a sinusoidal change in pressure results in a sinusoidal change in the velocity, that is the angular and spatial frequency is the same and $v(t, y) = v_A \sin(ky - \omega t + \phi)$ with the amplitude v_A and phase shift ϕ . Then

$$\left| \frac{\partial v}{\partial t} \right| \gg? \left| 2v \frac{\partial v}{\partial y} \right| \quad (5.24)$$

$$v_A \omega \gg? 2v v_A k \quad (5.25)$$

$$2\pi f \gg? 2v \frac{2\pi f}{c} \quad (5.26)$$

$$c \gg 2v, \quad (5.27)$$

which is true based on the second assumption, meaning that the change with respect to y can be neglected. The resulting equation is

$$\rho_0 \frac{\partial v}{\partial t} = - \frac{\partial p}{\partial y}. \quad (5.28)$$

The determination of the v and ρ fields are easy from here. First Equation (5.28) is used, and the velocity can be calculated by derivation with respect to y and then integration with respect to t . Finally, Equation (5.21) is used, and the density can be determined. The standing wave solution is

$$p(t, y) = p_0 + p_A \sin(\omega t) \cos(ky), \quad (5.29)$$

$$v(t, y) = - \frac{p_A}{c\rho_0} \cos(\omega t) \sin(ky) \text{ and} \quad (5.30)$$

$$\rho(t, y) = \rho_0 + \frac{p_A}{c^2} \sin(\omega t) \cos(ky). \quad (5.31)$$

The traveling wave solution is

$$p(t, y) = p_0 + p_A \sin(ky - \omega t), \quad (5.32)$$

$$v(t, y) = \frac{p_A}{c\rho_0} \sin(ky - \omega t) \text{ and} \quad (5.33)$$

$$\rho(t, y) = \rho_0 + \frac{p_A}{c^2} \sin(ky - \omega t). \quad (5.34)$$

These equations are used to set up the initial conditions in ALPACA.

5.3 Simulation settings

Table 5.1: The simulation setting

Simulation		#1	#2	#3	#4
Initial radius	$R_0 = R_E$	30 μm	<i>varying</i>	<i>varying</i>	40 μm
Frequency	f	120 kHz	130 kHz	<i>varying</i>	100 kHz
Pressure amplitude	p_A	<i>varying</i>	1.2 bar	<i>varying</i>	1.5 bar
Ambient pressure	p_0	1 bar	1 bar	1 bar	1 bar
Density of liquid	ρ_0	1000 kg/m ³	1000 kg/m ³	1000 kg/m ³	1000 kg/m ³
Dyn. viscosity (liquid)	μ_l	0.001 Pa · s			
Surface tension	σ	0.0728 N/m	0.067 N/m	0.0728 N/m	0.0728 N/m
EoS parameter (liquid)	γ_l	4.4	4.4	4.4	4.4
EoS parameter (liquid)	$p_{\infty,l}$	$6 \cdot 10^8$ Pa	$6 \cdot 10^8$ Pa	$6 \cdot 10^8$ Pa	$5.0854 \cdot 10^8$ Pa
Speed of sound	c_l	1624.8 m/s	1624.8 m/s	1624.8 m/s	1496 m/s
EoS parameter (gas)	γ_g	1.4	1.4	1.4	1.4
EoS parameter (gas)	$p_{\infty,g}$	0	0	0	0
Domain length	l	3λ	λ	3λ	2λ
Domain width	b	3λ	$\lambda/5$	1.5λ	$\lambda/2$
l_0 mesh	$b \times l$	144×144	16×80	<i>varying</i>	32×128
Refinement levels	l_{\max}	10	9	<i>varying</i>	9
Refinement tol.	ε	0.01	0.01	0.01	0.01
Bubble resolution	D_{cell}	218	≈ 236	≈ 300	175
Courant number		0.85	0.85	0.85	0.85

Table 5.2: Comparison of ALPACA simulation results to ROM

Simulation	f/kHz	$R/\mu\text{m}$	p_A/kPa	Dominant (ALPACA)	Dominant (ROM)
1/01	30	47.5	10	none	none
1/02	30	47.5	25	2	2
1/03	30	47.5	32	2	2
1/04	30	47.5	36	2	3
1/05	30	47.5	42	breakup	breakup
1/06	30	47.5	60	breakup	breakup
1/07	30	75	25	3	3
1/08	30	75	25	breakup	breakup
1/09	30	57.5	10	none	none
1/10	30	57.5	16	4	4
1/11	30	57.5	21	4	4
1/12	30	57.5	23.5	4	4
1/13	30	57.5	30	breakup	breakup
1/14	30	23	62	3	3
1/15	30	23	75	breakup	breakup
1/16	30	30	10	none	none
1/17	30	30	10	none	none
1/18	30	30	10	none	none
1/19	30	30	10	4	breakup
1/20	30	30	10	breakup	breakup
1/21	30	30	10	breakup	breakup
2/01	130	17.5	15	none	none
2/02	130	17.5	25	none	none
2/03	130	17.5	40	2	2
2/04	130	17.5	55	2	3
2/05	130	17.5	60	2	3
2/06	130	17.5	70	breakup	breakup
2/07	130	27	5	3	3
2/08	130	27	10	breakup	breakup
2/09	130	27	15	breakup	breakup
2/10	130	45	26	none	none
2/11	130	20	30	2	2
2/12	130	29	12.5	3	3
2/13	130	35	18.5	4	4
2/14	130	42.5	25	none	5
2/15	130	42.5	30	5	5
2/16	130	45	33	5	5
2/17	130	10	60	none	none
2/18	130	60	30	none	none
3/01	480	17.5	80	none	none
3/02	480	17.5	94	5	5
3/03	480	17.5	98	5	5
3/04	480	17.5	120	5	5
3/05	480	17.5	140	5	5
3/06	480	18.6	120	none	5
3/07	480	20	120	none	none
3/08	480	22	120	none	none
3/09	480	10.5	50	3	3
3/10	480	10.5	80	3	break
3/11	480	7.5	15	2	2
3/12	480	12.6	60	none	none
3/13	480	13.4	60	4	break
3/14	480	14.1	60	4	2
3/15	480	15	60	none	none
3/16	480	3	140	none	none
3/17	480	3	140	4	4
3/18	480	30	10	none	none
3/19	480	30	20	none	none
3/20	480	30	40	none	none
3/21	480	30	70	none	none
3/22	480	30	100	none	none
3/23	480	30	150	none	none

Table 5.3: Multi-bubble simulation settings and results

#	D^*	$\Delta R_{\max}^{(\text{top})}/\mu\text{m}$	$\Delta R_{\max}^{(\text{bot.})}/\mu\text{m}$	Observed phenomena (in order)
Case 1, $f = 100$ kHz, $p_A = 1.5$ bar, $R_0 = 40$ μm				
1/01	2.025	34.09	33.69	Flattening, Coalescence, Jet
1/02	2.05	34.75	34.79	Flattening, Symmetric jetting
1/03	2.075	34.62	34.92	Flattening, Symmetric jetting
1/04	2.15	34.92	35.02	Flattening, Symmetric jetting
1/05	2.25	35.46	34.86	Flattening, Symmetric jetting
1/06	2.375	35.95	34.77	Flattening, Symmetric jetting
1/07	2.5	36.37	34.71	Flattening, Symmetric jetting
1/08	2.75	37.03	34.71	Flattening, Symmetric jetting
1/09	3.	37.61	35.08	Flattening, Symmetric jetting
1/10	3.25	38.08	35.52	Flattening, Symmetric jetting
1/11	3.875	39.12	36.61	Flattening, Symmetric jetting
1/12	4.5	39.96	37.68	Bottom jet, Top jet
1/13	5.5	40.71	38.83	Bottom jet, Top jet
1/14	5.875	41.09	38.90	Bottom jet, Top jet
1/15	6.25	41.32	39.39	Bottom jet, Top jet halts
1/16	7.625	41.91	40.23	Delayed bottom jet
1/17	8.	41.91	40.34	Delayed bottom jet
1/18	8.5	42.06	40.65	Bottom jet halts
1/19	9.5	42.28	41.01	–
1/20	14.5	42.91	42.11	–
1/21	20.75	43.13	42.80	–
1/22	39.5	44.00	43.68	–
1/23	77.	44.03	44.54	–
1/24	∞	–	44.24	–
Case 2, $f = 100$ kHz, $p_A = 1.5$ bar, $R_0 = 80$ μm				
2/01	2.025	30.76	28.68	Flattening, Coalescence
2/02	3.	32.42	30.53	Flattening
2/03	4.	33.72	31.99	–
2/04	6.	35.14	33.82	–
2/05	10.	36.55	35.53	–
2/06	16.	37.40	36.70	–
2/07	27.	38.05	37.76	–
2/08	42.	38.37	38.53	–
2/09	∞	–	39.21	–
Case 3, $f = 50$ kHz, $p_A = 1.5$ bar, $R_0 = 40$ μm				
3/01	2.025.	62.32	61.92	Coalescence, Flattening, Jet
3/02	3.	62.06	62.26	Flattening, Symmetric jet
3/03	4.	67.04	61.68	Flattening, Symmetric jet
3/04	6.	69.64	65.12	Bottom jet, Top jet
3/05	10.	71.83	69.49	Bottom jet, Top jet
3/06	18.	71.17	68.68	Bottom jet, Top jet <i>Too low temporal resolution</i>
3/07	22	73.30	72.40	Bottom jet, Top jet <i>Fixed, Courant=0.2</i>
3/08	34.	69.23	70.61	Bottom jet, Top jet <i>Too low temporal resolution</i>
3/09	∞	–	74.77	Jet <i>Fixed, Courant=0.2</i>
Case 4, $f = 100$ kHz, $p_A = 1.5$ bar, $R_0 = 40$ μm , 3 bubbles				
4/01	2.25	32.58	30.14	Symmetric jet, Impact on middle bubble
4/02	4.5	36.98	34.74	Symmetric jet, Impact on middle bubble
4/03	9	40.77	39.18	–
4/04	20.75	43.05	42.22	–
4/05	52.	43.91	44.23	–